

The Pennsylvania State University
The Graduate School
College of Earth and Mineral Science

**SPECTROSCOPIC ELLIPSOMETRY STUDY OF TRANSPARENT CONDUCTING
METAL, STRONTIUM NIOBATE**

A Thesis in
Materials Science and Engineering
by
Yoonsang Park

© 2018 Yoonsang Park

Submitted in Partial Fulfillment
of the Requirements
for the Degree of
Master of Science

August 2018

The thesis of Yoonsang Park was reviewed and approved* by the following:

Venkatraman Gopalan

Professor of Materials Science and Engineering

Thesis Advisor

Roman Engel-Herbert

Associate Professor of Materials Science and Engineering

Thesis Co-advisor

Zhiwen Liu

Professor of Electrical Engineering

Suzanne Mohney

Professor of Materials Science and Engineering

Chair, Intercollege Graduate Program

in Materials Science and Engineering

*Signatures are on file in the Graduate School

ABSTRACT

Transparent conductors exhibit both optical transparency and high electrical conductivity. Because of these properties, they are utilized in a variety of technological applications, such as solid-state lighting, display panel, smart windows, and photovoltaics. Recently, correlated metals, which show different behavior compared to conventional metals due to interactions between electrons, are proved to be good candidates for transparent conductors. The electron correlations tune the optical and electrical properties so that correlated metals can exhibit high electrical conductivity and optical transparency in the visible range at the same time.

Spectroscopic ellipsometry is a powerful characterization tool to probe optical properties of materials. Spectroscopic ellipsometry measures the change in polarization state of light between incident light and reflected light. With proper analysis of ellipsometry data, one can obtain optical dielectric function and corresponding refractive index and extinction coefficients of materials. With refractive index and extinction coefficient, one can determine transmission, reflection, and absorption of the materials.

In this thesis, characterization of optical properties of correlated metal SrNbO_3 by spectroscopic ellipsometry will be discussed. In Chapter 1, the basics of spectroscopic ellipsometry, which includes basic concepts, general oscillators for modeling, and modeling method will be discussed. In Chapter 2, topics regarding correlated metal SrNbO_3 , including some background of correlated metals and transparent conductors, and spectroscopic ellipsometry results, will be discussed. Finally, in Chapter 3, Spectroscopic ellipsometry results for other correlated metals will be discussed.

TABLE OF CONTENTS

LIST OF FIGURES	vi
LIST OF TABLES	xii
Acknowledgements	xiii
Chapter 1 Spectroscopic Ellipsometry	1
1.1 Light at Interfaces and Fresnel's Equation	2
1.2 Basics of Spectroscopic Ellipsometry	6
1.2.1 Ellipsometric Parameter ρ	6
1.2.2 Pseudo-Dielectric Function	7
1.2.3 Jones Matrix	8
1.3 Optical Constants Models	11
1.3.1 Lorentz Model	11
1.3.2 Drude Model	17
1.3.3 Tauc-Lorentz Model	19
1.3.4 Sellmeier Model	21
1.3.5 Drude-Lorentz Model	22
1.3.6 Interband Absorption: Band Structure and Density of States	22
1.3.7 Effective Medium Theories	25
1.4 Ellipsometry Measurement Method	29
1.4.1 Sample Preparation	30
1.5 Data Analysis	30
Chapter 2 Transparent Conducting Correlated Metal SrNbO_3	33
2.1 Correlated Electron System	33
2.2 Transparent Conductors	34
2.2.1 Ultrathin Metallic Film	36
2.2.2 Metallic Nanowires	37
2.2.3 Transparent Conducting Oxides (TCOs)	38
2.2.4 Figure of Merit (Φ_{TC})	39
2.2.5 Key Descriptors for Transparent Conductors	41
2.3 Correlated Metals for Transparent Conductor Applications	42
2.3.1 Cost-Effectiveness of Transparent Correlated Metals	43
2.3.2 Performance of Transparent Correlated Metals	44
2.3.3 SrVO_3	45
2.4 Strong Interband Absorption in SrVO_3 and SrNbO_3 as Transparent Conductor	47

2.5 Theoretical and Experimental Results.....	50
2.5.1 Sample Growth and X-ray Diffraction	50
2.5.2 Spectroscopic Ellipsometry for SrNbO ₃ on KTaO ₃	51
2.5.3 Spectroscopic Ellipsometry for SrNbO ₃ on LSAT	56
2.5.4 DFT and DMFT Calculation	58
2.5.5 Hall Coefficient Measurement.....	60
2.5.6 Figure of Merit for SrNbO ₃	62
2.6 SrNbO ₃ as a Deep Ultraviolet Transparent Conductor	64
Chapter 3 Spectroscopic Ellipsometry Results on Other Correlated Metals	65
3.1 Co Doped BaFe ₂ As ₂	65
3.2 1-T TiS ₂	66
3.3 2-H NbSe ₂	67
Chapter 4 Conclusion and Future Work	69
References.....	70
Appendices.....	74
Appendix A Sample Calibration	74
Appendix B Data Acquisition	75
Appendix C Single Crystal.....	79
Appendix D Thin Film	81
Appendix E Surface Roughness Characterization	82

LIST OF FIGURES

Chapter 1

- Figure 1.1** Schematic diagram of spectroscopic ellipsometry measurement¹. The electric field components of incidence s- and p- wave are denoted with subscript, i_s and i_p , respectively, and those of reflected s- and p- wave are denoted with the subscript, r_s and r_p , respectively. The amplitude ratio Ψ and phase difference Δ are also represented in the figure. 1
- Figure 1.2** Light wave interacting with two different interfaces¹. The refractive indices of two different media are denoted as n_i and n_t , and important displacement points are also denoted. The angles for incident, transmitted and reflected light are also represented. 3
- Figure 1.3** s- and p- wave with plane of incidence³. The surface normal, the line drawn perpendicular to the incident surface, is represented as a dotted line. 4
- Figure 1.4 (a)** electric field and magnetic field component of p – polarized wave and **(b)** electric and magnetic field components of s- polarized wave¹. 6
- Figure 1.5** Lorentzian Single electron spring model. Electron particle moves opposite to the direction of applied electric field. In this scheme, vertical direction is z and horizontal direction is x, so that the scheme plane lies in x-z plane⁵. 12
- Figure 1.6** Dielectric function spectra of real ($K_{e,R}$) and imaginary ($K_{e,i}$) of single Lorentz model in terms of angular frequency in 10^{14} Hz⁶. Note the resonant frequency is located at 1 eV. 16
- Figure 1.7.** Optical spectra of Drude model⁷. Plasma frequency ω_p , is denoted as where real part of dielectric function ϵ_1 hits zero. 18

- Figure 1.8.** Reflectance (%) vs. wavelength of common metals⁸. Plasma frequency is the turning point of high and low reflection, where the slope of function gets infinite.....19
- Figure 1.9.** Tauc-Lorentz dielectric function spectra of amorphous silicon (a-Si)¹. Note that ϵ_2 peak is not symmetric anymore.21
- Figure 1.10 (a)** Band structure and **(b)** Density of States (DOS) of 1-T phase TiS₂¹². The dotted line denotes 0 eV, which is Fermi level. In Figure 1.10 (b), the numbers denote specific DOS peak to explain interband transition in the text.....23
- Figure 1.11** Imaginary optical dielectric constant (ϵ_2) of 1-T TiS₂ as a function of energy (eV), determined from spectroscopic ellipsometry.25
- Figure 1.12 (a)** spherical dielectric surrounded by a capacitor. The polarization arises due to external electric field generated by capacitor and surface polarization charge and **(b)** Spherical geometry of dielectric. L is the radius of the sphere, which is denoted by r in Equation (1.38)¹.26
- Figure 1.13 (a)** Schematics of Maxwell-Garnett model and **(b)** Schematics of Bruggeman Effective Medium Approximation¹³29
- Figure 1.14** Light propagation in multilayer sample when (a) light is reflected from both the surface and back side of the substrate and (b) the light is scattered by rough surface of back side of the substrate⁴.30

Chapter 2

- Figure 2.1** Electrical conductivity (σ) as function of renormalization factor Z_k of several metallic system²⁸. Note that conventional conductors have $Z_k = 1$, whereas

correlated electron systems have $Z_k < 1$	34
Figure 2.2 (a) Abundance of elements in Earth crust in function of atomic number Z and (b) indexed demanding of indium as function of year.	36
Figure 2.3 Comparative chart for candidates of transparent conductors: transparent conducting oxides (TCOs), ultrathin metallic film, graphene, metallic mesh and nanowires.	38
Figure 2.4 Key descriptors for figure of merit of transparent conductors. Red characters denote the ratio of carrier concentration (n) and effective mass of electrons (m^*).	42
Figure 2.5 Electrical conductivity (σ) of several transparent conductors as a function of plasma frequency (ω_p) ²⁸ . Note that both quantities depend on carrier concentration (N_f) and electron effective mass (m^*).	46
Figure 2.6 (a) thickness dependence of conductivity of several transparent conducting materials and (b) real and imaginary part of dielectric function spectra of SrVO ₃ determined from density functional theory (red lines) and spectroscopic ellipsometry (purple dots) ²⁸	46
Figure 2.7 Unit cells of SrNbO ₃ . SrNbO ₃ has Perovskite unit cell with A site occupancy of Sr cation, B site occupancy with Nb cation, which is surrounded by oxygen octahedra.	49
Figure 2.8 X-ray diffraction peaks for six SrNbO ₃ thin films. The 5-digit numbers correspond to the thickness of 10.6 nm (18001), 23.2 nm (18003), 29.2 nm (18002), 37 nm (14149), 40 nm (14122) and 60 nm (14123).	50

- Figure 2.9** Spectroscopic ellipsometry data (Ψ and Δ) for KTaO_3 and fitting result. The data was fitted with two Lorentz oscillators.....52
- Figure 2.10** Ellipsometry fitting result after properly setting up oscillators and layer optical model for substrate and thin film.....53
- Figure 2.11** Ellipsometry fitting results after the refinement. The refinement includes adjustment of the fitting parameters, and consideration of surface roughness...54
- Figure 2.12** Dielectric function spectra of five SrNbO_3 samples with different thicknesses determined from spectroscopic ellipsometry, along with DFT calculation. The spectral range is from 0.1 eV to 5.1 eV. Rainbow in the background denotes the visible range.....56
- Figure 2.13** Optical dielectric function of four sputtered SrNbO_3 thin films determined from spectroscopic ellipsometry, along with DFT calculation. The spectral range is from 0.7 eV to 5.1 eV.....57
- Figure 2.14** Band structure of (a) SrVO_3 and (b) SrNbO_3 determined from DFT with DMFT correction. Fermi level is denoted as white line (DMFT) at 0 eV. For DFT band structure, Nb-eg bands, Nb-t2g bands, and oxygen 2p bands are presented. In Courtesy of Dr. Turan Birol.....59
- Figure 2.15** (a) Sheet resistance, (b) mobility, and (c) carrier concentration as function of film thickness at the room temperature. The line fit in Figure 2.8 (a) shows Fuch and Sondheimer (FS) and Mayadas and Shatzkes (MS) model. The experimental error bars are smaller than the legends.62
- Figure 2.16** Figure of Merit as function of film thickness for conventional transparent conductors at (a) visible range (400- 800 nm), (b) UV A range (315 – 400 nm), (c)

UV B range (280 – 315 nm), and (d) Germicidal UV range (250 – 280 nm). Experimental data points were extracted for silver^{32,62} (grey circles), ITO^{42,63} (blue circles), SrVO₃²⁸ (yellow green circles) and SrNbO₃ from this work. Line fits are from Φ_{TC} calculation, discussed in **Chapter 2.2.4**.63

Chapter 3

Figure 3.1 (a) Refractive index (n) and **(b)** extinction coefficients (k) of 10% Co doped BaFe₂As₂ determined from spectroscopic ellipsometry, with incident angle of 50°, 60° and 70°.66

Figure 3.2 Refractive index (n , red) and extinction coefficients (k , green) of 1-T TiS₂ determined from spectroscopic ellipsometry. The Bruggeman EMA fitting gives the roughness thickness of about 5 nm.67

Figure 3.3 (a) real (ϵ_1) and **(b)** imaginary (ϵ_2) part of dielectric function spectra of NbSe₂, as a function of energy (eV). The line in the plot of ϵ_1 is parallel to 0 value in order to denote plasma frequency.68

Appendices

Figure A.1 CompleteEase software that shows the result of calibration. The MSE value and measured film thickness are listed in the upper left side of the figure. The plots of raw data and model are shown in the bottom part of the figure, as a function of wavelength in nm.75

Figure B.1 Data acquisition procedure for CompleteEase software. The window in the middle is “Acquisition Parameters Setup”, which can control the measurement method.76

- Figure B.2** Beam alignment window that shows **(a)** before the alignment and **(b)** after the alignment. For properly aligned reflected beam, the red cross should coincide with the black cross.77
- Figure B.3** CompleteEase software after ellipsoemetry measurement is done. The plot shows three sets of psi (Ψ) and delta (Δ) vs. wavelength in nm with incident angle of 55° , 65° and 75°78
- Figure C.1** Parameterize Layer window in CompleteEase software. The gray box mentioned in the text is on the upper left corner of the figure.80
- Figure E.1** Analysis panel of CompleteEase containing EMA layer (green box). The layer has several options for surface roughness characterization.82

LIST OF TABLES

Table 1.1 Jones vectors with corresponding polarization states of light ¹ . The x and y axis shown here are two directions perpendicular to the direction of propagation of light.....	9
Table 1.2 Example of Jones matrices with corresponding optical elements. δ is phase difference caused by a compensator (retarder) and α is angle of coordinate rotation ¹	10
Table 2.1 Resistivity and growth conditions of four different SrNbO ₃ thin films grown by sputtering technique. Numbering (_#) denotes two different thin films with the same film thickness. In courtesy of Joseph Roth.....	58

Acknowledgements

I would like to thank Dr. Venkatraman Gopalan, my thesis advisor, for mentoring me with great wisdom. His guidance throughout the period of Master's degree has been extremely helpful, in terms of both understanding complex concepts of optics and conducting optics experiments. I indeed have learnt a lot from his teaching. I would also like to thank Dr. Roman Engel-Herbert for helpful discussion related to electron correlation and scattering mechanism of electrons in conducting thin films. I am also grateful to Dr. Zhiwen Liu and Dr. Ismaila Dabo for brief discussions regarding optics and solid-state physics. I would also like to say thanks to Dr. Alexej Pogrebnjakov for discussions regarding spectroscopic ellipsometry. The discussions have been indeed very helpful for this work. Finally, I want to acknowledge Dr. Turan Birol at University of Minnesota for invaluable an-hour-lasting discussion regarding electron correlation, DFT and DMFT calculations.

It has been a pleasure to work with my group members. I enjoyed working and discussing matters with Yakun Yuan, Haricharan Padmanabhan, Disha Talreja, and Hugo Wang. It also has been a pleasure to collaborate with Joseph Roth from Dr. Engel-Herbert's group in transparent conductor project.

Finally, I would like to thank my family. They have always respected my decision and been supportive throughout my life. I would especially like to thank my father, Suman, for counseling and mentoring me whenever I face hardship.

This thesis is based upon work supported by the National Science Foundation (NSF) under NSF-DMREF: DMR #1629477. Any opinions, findings, and conclusions or recommendations expressed in this thesis are those of the author and do not necessarily reflect the views of the National Science Foundation.

Chapter 1 Spectroscopic Ellipsometry

Spectroscopic ellipsometry characterizes optical properties by probing reflection or transmission of the light from media. **Figure 1.1** shows schematic diagram of reflective spectroscopic ellipsometry. The light source shoots the incidence light with known polarization state and the detector measures the change in the polarization state of light. The name “ellipsometry” is originated from the fact that reflected or transmitted light often becomes elliptically polarized. The change in the polarization state of the light measured by ellipsometry can be represented as Ψ , the amplitude ratio, and Δ , the phase difference between s- and p-polarized light. The spectroscopic ellipsometry measures spectra of Ψ and Δ in ultraviolet (UV) and visible region, but often the measurements can be done in infrared region.

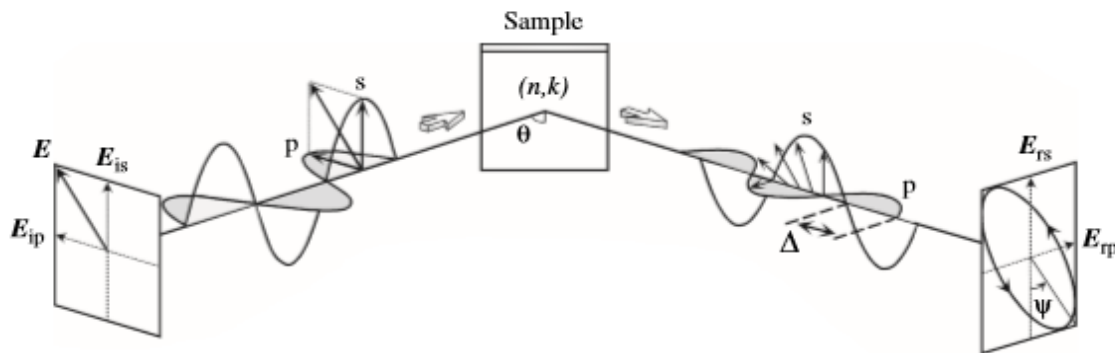


Figure 1.1 Schematic diagram of spectroscopic ellipsometry measurement¹. The electric field components of incidence s- and p- wave are denoted with subscript, is and ip, respectively, and those of reflected s- and p- wave are denoted with the subscript, rs and rp, respectively. The amplitude ratio Ψ and phase difference Δ are also represented in the figure.

Once the spectroscopic ellipsometry measures spectra of Ψ and Δ , one can determine complex optical dielectric function spectra ($\epsilon_1 + i \epsilon_2$), and corresponding refractive index (n) and extinction coefficient (k) by proper analysis. Or, if the spectra of optical constants of specific material is already known, one can determine the thickness of the sample. The pros of ellipsometry is that it is indeed very useful tool to determine optical constants of materials and thickness of film with very high sensitivity ($\sim 0.1 \text{ \AA}$) in a non-destructive way. However, there

are usually two restrictions for ellipsometry measurement¹. One is the surface roughness. If surface roughness is too large and the light depolarization rate exceeds ~5 %, the measurement error starts to increase enormously, since rough surface decreases the intensity of reflected light by light scattering. The other is that the measurements should be done at oblique angle, since ellipsometry measures the change in polarization state in s- and p- polarized light. If the measurements are done in normal incidence, s- and p- polarization of light do not exist, hence cannot properly measure Ψ and Δ . However, there is an exception. Normal incidence measurements can be done on the sample that has in-plane anisotropy. This topic will not be discussed in this thesis.

1.1 Light at Interfaces and Fresnel's Equation

Spectroscopic ellipsometry is indeed a tough subject to discuss. In this section, I will briefly go over how light interacts with the interfaces of media. The concepts that will be discussed here are very crucial to understand mechanism of ellipsometry. For more information, please read Fujiwara Hiroyuki's *Spectroscopic Ellipsometry: Principles and Applications*¹ or *Gopalan Note Ch. 5 Light at Interfaces*².

For simplicity, let us consider the light propagating through interfaces consist of two different media, represented in **Figure 1.2**. When the incident light travels from point B to D during a time t , the transmitted light travels from point A to E, and reflected light goes to point C. Let θ_i , θ_r and θ_t be the angles of incidence, reflection and transmission, respectively. By considering the facts explain above, we can derive the following equation:

$$\frac{\sin \theta_i}{BD} = \frac{\sin \theta_t}{AE} = \frac{\sin \theta_r}{AC} = \frac{1}{AC} \quad (1.1)$$

and, we know that the speed of the light in a medium is given by $v = c/n$, where v is speed of the light in the medium, c is the speed of light in air/vacuum, and n is refractive index of the

medium. By considering this fact, we can also obtain the following equation:

$$\overline{BD} = \frac{ct}{n_i}, \overline{AE} = \frac{ct}{n_t}, \overline{AC} = \frac{ct}{n_r} \quad (1.2)$$

Where n_i , n_t and n_r refers to the refractive indices of incident, transmitted and reflected light wave. It is obvious from the **Figure 1.2** that $\overline{BD} = \overline{AC}$. Since $n_i = n_r$, we obtain $\theta_i = \theta_r$, which is the law of reflection.

If we combine **Equation (1.1) and (1.2)**, we can derive simple Snell's Law:

$$n_i \sin \theta_i = n_t \sin \theta_t \quad (1.3)$$

For Snell's Law shown above, we can also substitute refractive index to complex refractive index notation, which can be represent as $N = n + i k$, where n is refractive index and k is extinction coefficient.

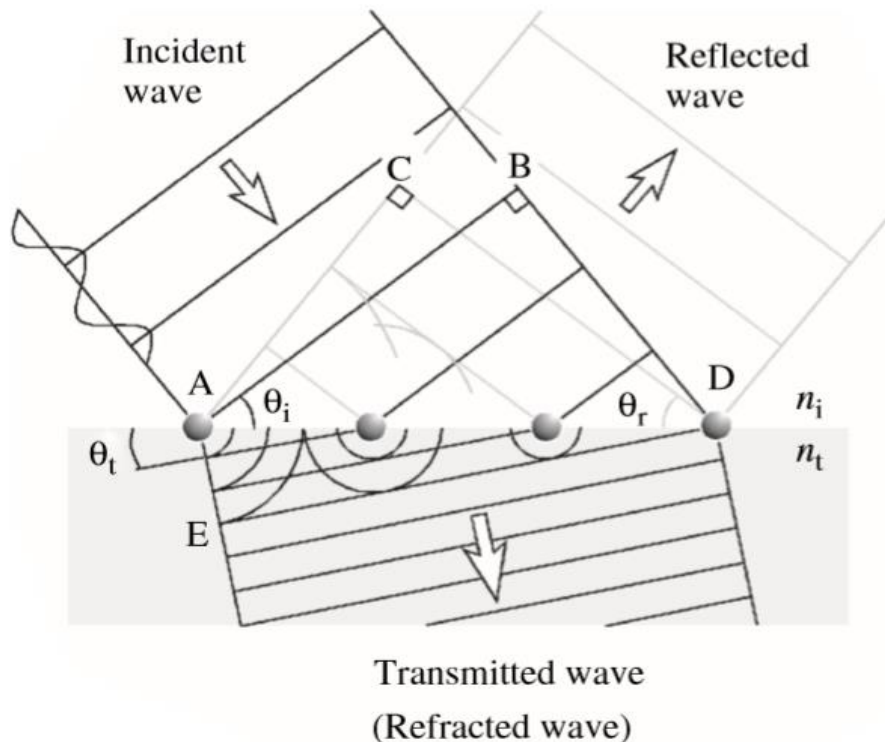


Figure 1.2 Light wave interacting with two different interfaces¹. The refractive indices of two different media are denoted as n_i and n_t , and important displacement points are also denoted. The angles for incident, transmitted and reflected light are also represented.

Now, let's deal with more complicated situation. Since most of the ellipsometry measurements are done with oblique angle, it is important to understand how light wave, either after transmitted or reflected back from the media, can be modified or changed. For oblique incidence, there are two types of light polarization, simply called s and p. **Figure 1.3** shows s- and p- polarized waves, along with the plane of incidence. The plane of incidence is defined as the plane that contains incident light, surface normal, reflected light, and transmitted light wavevectors. The p- wave, or p- component of light is defined as electric field component oscillates parallel to the plane of incidence, whereas s- wave, or s- component of light is defined as electric field oscillation perpendicular to the plane of incidence.

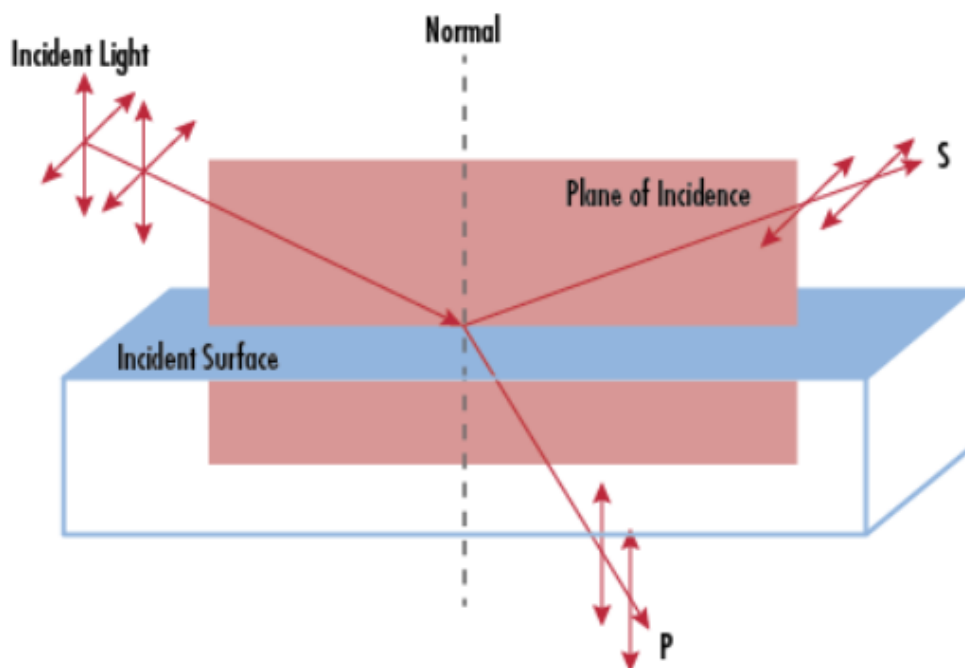


Figure 1.3 s- and p- wave with plane of incidence³. The surface normal, the line drawn perpendicular to the incident surface, is represented as a dotted line.

Figure 1.4 shows electric field and magnetic field components of s- and p- polarized wave. With the basic knowledge of light, light is an electromagnetic wave, which is composed of both oscillating electric field and magnetic field perpendicular to each other. Let's first look at the case of p-polarized wave, shown in **Figure 1.4 (a)**. For p-polarized light wave, parallel

component of p – wave on the incident side must be continuous at the interface. Considering boundary condition at the interface, the parallel component of p-polarized incident light should be equal to the parallel component of transmitted light. In terms of mathematical equation involving both electric and magnetic field, we have:

$$E_{ip}\cos\theta_i - E_{rp}\cos\theta_r = E_{tp}\cos\theta_t, \quad B_{ip} + B_{rp} = B_{tp} \quad (1.4)$$

Since we know that, in the medium with refractive index of n , $E = vB$, where $v = c/n$, the second part of **Equation (1.4)** becomes:

$$n_i(E_{ip} + E_{rp}) = n_t E_{tp} \quad (1.5)$$

Combining **Equation (1.4)** and **Equation (1.5)** by plugging in **Equation (1.5)** to the right-hand side of the first part of **Equation (1.4)** we can obtain the reflection coefficient for p-polarized wave:

$$r_p \equiv E_{rp}/E_{ip} = \frac{n_t \cos\theta_i - n_i \cos\theta_t}{n_t \cos\theta_i + n_i \cos\theta_t} \quad (1.6)$$

Similarly, we can also obtain the transmission coefficient for p-polarized wave:

$$t_p \equiv E_{tp}/E_{ip} = \frac{2n_i \cos\theta_i}{n_t \cos\theta_i + n_i \cos\theta_t} \quad (1.7)$$

For s- polarized wave shown in **Figure 1.4 (b)**, we have the following boundary conditions:

$$-B_{is}\cos\theta_i + B_{rs}\cos\theta_r = -B_{ts}\cos\theta_t, \quad E_{is} + E_{rs} = E_{ts} \quad (1.8)$$

Where the subscript is, rs and ts refers to incident, reflected and transmitted s- wave. With the same method for deriving reflection and transmission coefficient of p -polarized wave, we can also simply derive the expression for reflection and transmission coefficient for s- polarized wave:

$$r_s \equiv E_{rs}/E_{is} = \frac{n_i \cos\theta_i - n_t \cos\theta_t}{n_i \cos\theta_i + n_t \cos\theta_t}, \quad t_s \equiv E_{ts}/E_{is} = \frac{2n_i \cos\theta_i}{n_i \cos\theta_i + n_t \cos\theta_t} \quad (1.9)$$

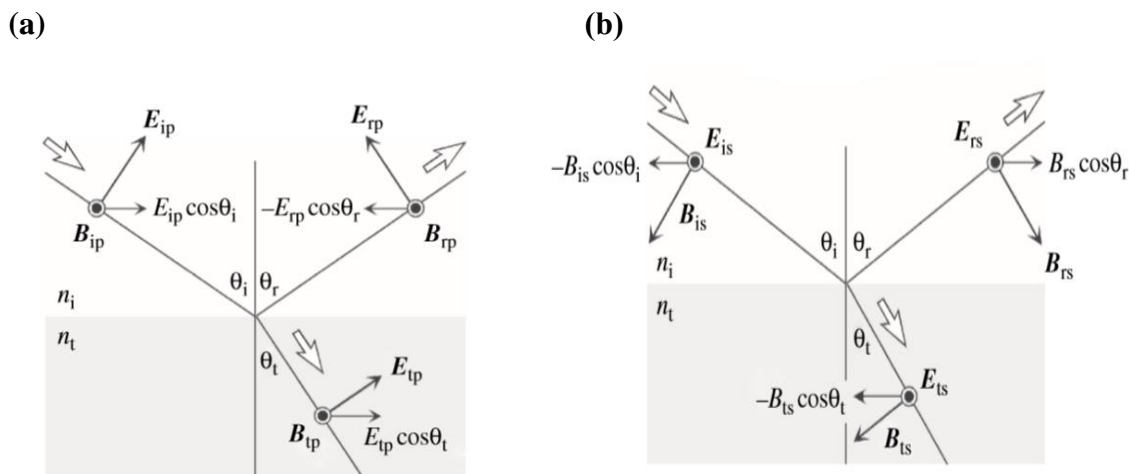


Figure 1.4 (a) electric field and magnetic field component of p – polarized wave and (b) electric and magnetic field components of s- polarized wave¹.

The **Equations (1.6), (1.7) and (1.9)** are called Fresnel's equation. Fresnel's equation determines the relationship between s- and p- polarized light in terms of refractive indices and incidence angle. The reflection and transmission coefficient for each wave determines the amplitude ratio. These relationships will become much more important, as we will go through the basics of spectroscopic ellipsometry in the later chapters.

1.2 Basics of Spectroscopic Ellipsometry

1.2.1 Ellipsometric Parameter ρ

As mentioned earlier, spectroscopic ellipsometry measures the amplitude ratio Ψ and phase difference Δ between s- and p- waves. So, how are they related to the optical constants of the media? First, let's define ellipsometric parameter ρ in terms of Ψ and Δ ^{1,4}:

$$\rho \equiv \tan \Psi \exp(-i\Delta) \quad (1.10)$$

The ellipsometric parameter ρ represents both amplitude ratio and phase difference of s- and p- polarized light in one simple equation. Now, let us consider reflective spectroscopic ellipsometry. In terms of Fresnel's coefficients, ρ can be represented as:

$$\rho \equiv r_p/r_s \quad (1.11)$$

We already know that, from **Chapter 1.1**, the reflection coefficients are related to the refractive index n of the media. If we replace the refractive index term to the complex refractive index, which includes both n and k , ρ will be in terms of both n and k . By fitting Ψ and Δ with appropriate modeling equation, both optical constants can be extracted from ellipsometry spectra.

1.2.2 Pseudo-Dielectric Function

The pseudo-dielectric function $\langle \epsilon \rangle$ is a dielectric function determined directly from measured Ψ and Δ . The calculation of $\langle \epsilon \rangle$ assumes perfectly flat surface with infinite thickness. If there is any surface roughness on the sample, $\langle \epsilon \rangle$ varies depending on the surface roughness. Since it is inevitable that any sample has surface roughness, $\langle \epsilon \rangle$ is not exactly the same as the dielectric function of the sample itself. However, if sample has surface roughness of several Å, which can be obtained from cleaved surface of single crystal or commercially available substrates, the effect of surface roughness can be neglected. $\langle \epsilon \rangle$ is also affected by optical interference, which is presented in a thin-film structure. The interference occurs between the reflected ray from the surface and the reflected ray from interface between film and substrate. Let's recall some equations derived in **Chapter 1.1**. The expression for reflection coefficients of p- and s- waves are given in **Equation (1.6)** and **Equation (1.9)**, respectively. In **Chapter 1.2.1**, the expression for ellipsometric parameter ρ was derived, in terms of reflection coefficients of p- and s- waves. By plugging in the expressions of reflection coefficients in **Equation (1.6)** and **Equation (1.9)** to the expression of ρ in **Equation (1.11)**, we can obtain the following relationship:

$$\rho = \frac{\sin^2\theta_i - \cos\theta_i[\epsilon_t/\epsilon_i - \sin^2\theta_i]^{1/2}}{\sin^2\theta_i + \cos\theta_i[\epsilon_t/\epsilon_i - \sin^2\theta_i]^{1/2}} \quad (1.12)$$

Where ϵ_t and ϵ_i are dielectric function of medium and ambient, respectively. If we assume that

$\varepsilon_i = 1$ and $\varepsilon_t = \langle \varepsilon \rangle$, we can get the following relationship:

$$\langle \varepsilon \rangle = \varepsilon_t = \sin^2 \theta_i \left[1 + \tan^2 \theta_i \frac{(1 - \rho)}{(1 + \rho)} \right] \quad (1.13)$$

Equation (1.13) is the expression of $\langle \varepsilon \rangle$ in terms of incident angle θ_i . As mentioned in the introduction, $\langle \varepsilon \rangle$ is also represented as a complex number, simply $\langle \varepsilon \rangle = \langle \varepsilon_1 \rangle + i \langle \varepsilon_2 \rangle$. The pseudo-dielectric constant can also be converted to pseudo-optical constants:

$$\langle \varepsilon \rangle = \langle \varepsilon_1 \rangle + i \langle \varepsilon_2 \rangle = (\langle n \rangle + i \langle k \rangle)^2 \quad (1.14)$$

As mentioned above, since pseudo-dielectric function and pseudo-optical constants are directly calculated from Ψ and Δ , they directly represent optical constants of a material itself when there is no surface roughness and the thickness is thick enough not to have back reflection.

1.2.3 Jones Matrix

Jones matrix is a matrix representation that represents polarization states of light¹. This mathematical representation can be utilized to explain ellipsometry measurements. The 2 x 1 Jones vector defines the light in x and y direction, which are perpendicular to each other. The two directions are defined with the assumption that z direction is the direction of propagation of light. For the two cases of linearly polarized light in x and y direction, we have:

$$E_{x,linear} = \begin{bmatrix} 1 \\ 0 \end{bmatrix}, \quad E_{y,linear} = \begin{bmatrix} 0 \\ 1 \end{bmatrix} \quad (1.15)$$

The different types of Jones vector for each type of light polarization is listed in **Table (1.1)**. Note that Jones vector is always normalized, meaning that the magnitude of the vector is always 1. Meanwhile, Jones matrices, which are 2 x 2, are operators that act on the Jones vector. The Jones matrices explain coordinate transformation of the light polarization by optical elements, such as polarizer, analyzer, compensator, and etc. These matrices can be utilized when considering various optical elements in ellipsometry. Examples of Jones matrices are listed in **Table (1.2)**.

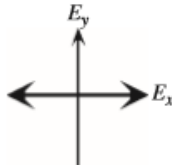
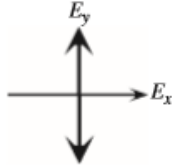
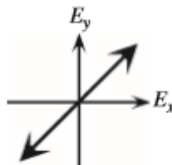
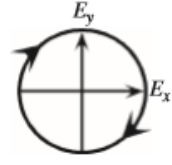
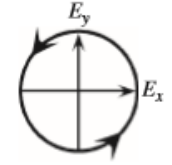
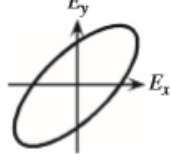
Polarization	Polarization state	Jones vector
Linear polarization parallel to x axis		$\begin{bmatrix} 1 \\ 0 \end{bmatrix}$
Linear polarization parallel to y axis		$\begin{bmatrix} 0 \\ 1 \end{bmatrix}$
Linear polarization oriented at 45°		$\frac{1}{\sqrt{2}} \begin{bmatrix} 1 \\ 1 \end{bmatrix}$
Right-circular polarization		$\frac{1}{\sqrt{2}} \begin{bmatrix} 1 \\ i \end{bmatrix}$
Left-circular polarization		$\frac{1}{\sqrt{2}} \begin{bmatrix} 1 \\ -i \end{bmatrix}$
Elliptical polarization		$\begin{bmatrix} \sin \psi \exp(i\Delta) \\ \cos \psi \end{bmatrix}$

Table 1.1 Jones vectors with corresponding polarization states of light¹. The x and y axis shown here are two directions perpendicular to the direction of propagation of light.

Now, considering the notation, the Jones matrix in ellipsometry measurement that corresponds to the reflection of the light can be represented by:

$$J = \begin{bmatrix} r_p & 0 \\ 0 & r_s \end{bmatrix} \quad (1.16)$$

This Jones matrix is for the case of simple isotropic media. For the case of anisotropic

media, where refractive indices are different with the crystallographic direction of the materials, the off-diagonal terms become nonzero. For the simple case, let's consider the incident light is polarized in 45° and then reflected in the case of isotropic media. The light reflection can be expressed as:

$$\begin{bmatrix} E_{rp} \\ E_{rs} \end{bmatrix} = \begin{bmatrix} r_p & 0 \\ 0 & r_s \end{bmatrix} \begin{bmatrix} E_{ip} \\ E_{is} \end{bmatrix} = \begin{bmatrix} r_p \\ r_s \end{bmatrix} \quad (1.17)$$

With this example, we realize that Jones vectors and matrices can be used to explain polarization state of light in ellipsometry measurement^{1,4}. This will further be discussed in the later chapter.

Optical element	Jones matrix
Polarizer ^a (Analyzer) $P(A)$	$\begin{bmatrix} 1 & 0 \\ 0 & 0 \end{bmatrix}$
Compensator ^b (Retarder) C	$\begin{bmatrix} 1 & 0 \\ 0 & \exp(-i\delta) \end{bmatrix}$
Photoelastic modulator ^c M	$\begin{bmatrix} 1 & 0 \\ 0 & \exp(i\delta) \end{bmatrix}$
Coordinate rotation ^d $R(\alpha)$	$\begin{bmatrix} \cos \alpha & \sin \alpha \\ -\sin \alpha & \cos \alpha \end{bmatrix}$
Sample ^e S	$\begin{bmatrix} \sin \psi \exp(i\Delta) & 0 \\ 0 & \cos \psi \end{bmatrix}$

Table 1.2 Example of Jones matrices with corresponding optical elements. δ is phase difference caused by a compensator (retarder) and α is angle of coordinate rotation¹.

1.3 Optical Constants Models

In this section, several optical oscillator models will be discussed. For the section, the following three optical spectrum models will be discussed: Lorentz, Tauc-Lorentz, and Drude. One cannot fit the ellipsometry data without understanding these models. Each model explains the behavior of optical dielectric constants in the specific range of spectra (usually from infrared to visible and UV) in specific cases of media. Along with three models, Sellmeier model, interband transition, and effective media theories, which explains optical constants of surface roughness of the media, will be discussed briefly.

1.3.1 Lorentz Model

In this section, classical Lorentz model will be discussed. Let's think about the case of insulating media. For insulating media, electrons are tightly bounded to nuclei and they can only move around a little bit. Lorentz model assumes that electrons are bounded to nuclei with very stiff spring. The schematic diagram of classical Lorentz model is illustrated in **Figure 1.5**. Normally, without any external field, the center of electron coincides with the center of protons. However, if we apply some electric field in a certain direction, the electron will move toward the opposite direction, according to Lorentz force relationship without external magnetic field, $\mathbf{F} = q\mathbf{E}$, where F is force, q is charge, and E is electric field. Here, note that F and E are vectors, and q is scalar quantity. Now, as we learned from undergraduate elementary physics, the natural angular frequency ω_0 of a spring can be represented as:

$$\omega_0 = \sqrt{k/m} \quad (1.18)$$

With the attached mass m and spring constant k . The natural angular frequency is the frequency, at which any unperturbed mechanical system would like to vibrate. This is also called resonant frequency. Now, let's look at the **Figure 1.5** and assume that light is shed on this one nuclei in

x-z plane. In this scheme, the x direction is horizontal, z direction is vertical, and y is out of plane direction. We know that light is electromagnetic wave, so we can consider it as an oscillating AC electric field. Under the AC electric field, the electron will oscillate back and forth. The electric field of light can be expressed as:

$$E_{\text{light}} = E_0 e^{i(kz - \omega t)} \hat{x} \quad (1.19)$$

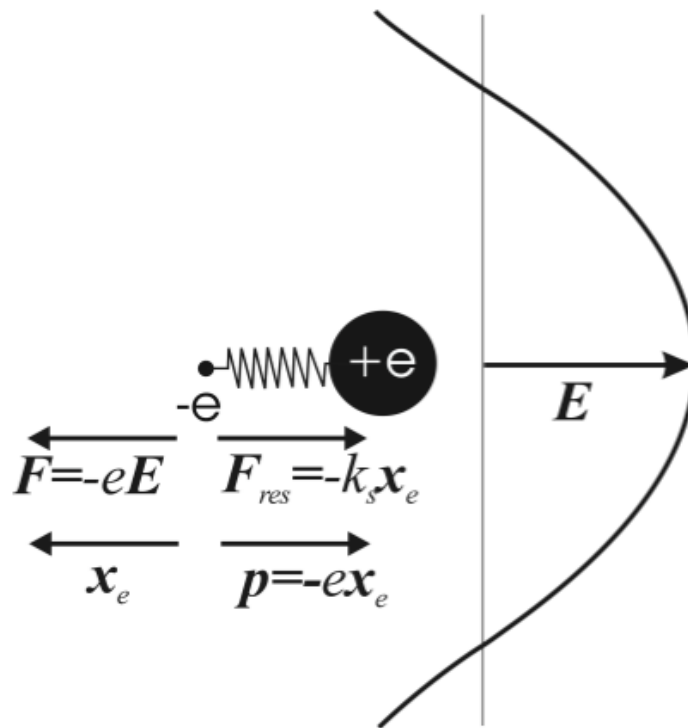


Figure 1.5 Lorentzian Single electron spring model. Electron particle moves opposite to the direction of applied electric field. In this scheme, vertical direction is z and horizontal direction is x, so that the scheme plane lies in x-z plane⁵.

Where E_0 is amplitude of light, ω is frequency of light, and k is wavevector. **Equation (1.19)** represents AC electric field that is propagating along z direction (vertical) and oscillates along x direction (horizontal). If we reconsider the Lorentz force equation mentioned previously in this section. Simple Newton's law shows that $\mathbf{F} = m\mathbf{a}$, where \mathbf{F} is force, m is mass and \mathbf{a} is acceleration. Now, equating Newton's Law with Lorentz force equation and considering **Equation (1.19)**, we get:

$$F_{net} = m \frac{d^2x}{dt^2} = (eE_0 e^{i(kz-\omega t)} - kx)\hat{x} \quad (1.20)$$

Where F_{net} is net force in the system, e is elementary charge. This is a differential equation in terms of displacement x . If we rewrite **Equation (1.20)** by using the expression for the resonant frequency in **Equation (1.18)**, we have:

$$\frac{d^2x}{dt^2} + \omega_0^2 x = \frac{eE_0}{m} e^{i(kz-\omega t)}\hat{x} \quad (1.21)$$

The steady state solution of this differential equation comes out to be:

$$x = \frac{eE_0}{m(\omega_0^2 - \omega^2)} e^{i(kz-\omega t)}(-\hat{x}) = \frac{-eE_{light}}{m(\omega_0^2 - \omega^2)} \quad (1.22)$$

From **Equation (1.22)**, we can note several points. The first is that the spring displacement x becomes larger, as the amplitude of light E_0 becomes larger. Therefore, if we increase the intensity of incidence light on the media, the oscillation displacement of electron will become also large. The second is that electron oscillates with the same frequency as that of light. The third is that the displacement is opposite to the oscillation of external electric field when ω is smaller than ω_0 , and it is along the oscillation direction of electric field when ω is larger than ω_0 . This is very intuitive. The fourth is that the displacement becomes infinite when ω is equal to ω_0 . This is indeed exaggerated, and we shall discuss more on this in the later chapter.

Now, let's get back to the Lorentz model shown in **Figure 1.5**. We know that electrons attached to nuclei will oscillate back and forth under incident light that is composed of external AC electric field. From elementary physics, we know that dipole moment is created if there is any displacement between positive charge and negative charge. As a result of oscillating displacement of electrons, there exists oscillating electrical dipole moment. The dipole moment p is given by:

$$p = (-e)x = \alpha E_{light} \quad (1.23)$$

Where x is displacement represented in **Equation (1.22)**, E_{light} is an electric field of light, and α is called polarizability. This quantity tells you how much you can polarize an atom with given electric field. By using **Equation (1.22)**, we can express polarizability α as:

$$\alpha = \frac{e^2}{m(\omega_0^2 - \omega^2)} \quad (1.24)$$

Now, recall that it is exaggerated the displacement becomes negative when the frequency of light becomes equal to resonant frequency. The one thing we are missing here is damping of the spring. In reality, a spring does not oscillate forever, since there always exists frictional force that dampens the oscillation with time. The damping force is proportional to velocity of the mass and constant of proportionality Γ , which is related to viscosity of medium, in which the motion occurs. If we add the damping term in **Equation (1.20)**, we get the following equation:

$$F_{net} = m \frac{d^2x}{dt^2} = \left(eE_0 e^{i(kz-\omega t)} - kx - \Gamma \frac{dx}{dt} \right) \hat{x} \quad (1.25)$$

If we rewrite the equation in terms of resonant frequency, we get the similar expression as **Equation (1.21)**:

$$\frac{d^2x}{dt^2} + \Gamma \frac{dx}{dt} + \omega_0 x = \frac{eE_0}{m} e^{i(kz-\omega t)} \hat{x} \quad (1.26)$$

This is differential equation in terms of displacement x . The steady state solution for this differential equation is given by:

$$x = \frac{eE_0}{m(\omega_0^2 - \omega^2 - i\Gamma\omega)} e^{i(kz-\omega t)} (-\hat{x}) = \frac{-eE_{light}}{m(\omega_0^2 - \omega^2 - i\Gamma\omega)} \quad (1.27)$$

Note that the displacement does not become zero even though the light frequency is equal to resonant frequency. This represents Lorentz model with light absorption of the media.

Recall the expression for the polarizability α expressed in **Equation (1.23)**. With the consideration of damping term, α becomes:

$$\alpha = \frac{e^2}{m(\omega_0^2 - \omega^2 - i\Gamma\omega)} \quad (1.28)$$

Now, we can turn our attention to refractive indices of media. The complex refractive index N ($N = n + i k$) can be expressed as:

$$N^2 = \varepsilon = (1 + \chi_e) = 1 + \frac{fN_e\alpha}{\varepsilon_0} \quad (1.29)$$

Where ε is complex optical dielectric function ($\varepsilon = \varepsilon_1 + i \varepsilon_2$), χ_e is electrical susceptibility, f is the fraction of atoms that has resonant frequency ω_0 , N_e is number of atoms per unit volume, and ε_0 is vacuum permittivity. Then, by relating **Equation (1.25)** to **Equation (1.26)**, we can rewrite **Equation (1.29)** as:

$$N^2 = \varepsilon = 1 + \frac{fN_e e^2}{m\varepsilon_0(\omega_0^2 - \omega^2 - i\Gamma\omega)} \quad (1.30)$$

In general, multiple Lorentz functions exist in the spectral range. Therefore, one can rewrite **Equation (1.30)** as:

$$N^2 = \varepsilon = 1 + \sum_j \frac{f_j N_e e^2}{m\varepsilon_0(\omega_{0,j}^2 - \omega^2 - i\Gamma\omega)} \quad (1.31)$$

Where subscript j refers to different kinds of oscillator. By looking at the **Equation (1.31)**, we know that the function is a complex function that is composed of real and imaginary part. By separating **Equation (1.31)** to real and imaginary part, we get the following function:

$$\begin{aligned} N^2 = \varepsilon = 1 + \sum_j \frac{f_j N_e e^2}{m\varepsilon_0} \frac{(\omega_{0,j}^2 - \omega^2)}{(\omega_{0,j}^2 - \omega^2)^2 + (\Gamma\omega)^2} \\ + i \left(\frac{f_j N_e e^2}{m\varepsilon_0} \frac{\Gamma\omega}{(\omega_{0,j}^2 - \omega^2)^2 + (\Gamma\omega)^2} \right) \end{aligned} \quad (1.32)$$

The real part of **Equation (1.32)** explains real part of dielectric function (ϵ_1) and the imaginary part is imaginary dielectric function (ϵ_2) when there is only one Lorentz model in the spectrum. The dielectric function spectra of single Lorentz model are shown in **Figure 1.6**. Note that imaginary part of dielectric function (ϵ_2) has a peak at resonant frequency (ω_0), and the center of declination of real part of dielectric function is also located in ω_0 . Now, the equation for Lorentz model is indeed derived. This is very useful since most of the media has at least one absorption peak that can be explained by Lorentz model. One should get very used to Lorentz model and the equation when modeling ellipsometry data.

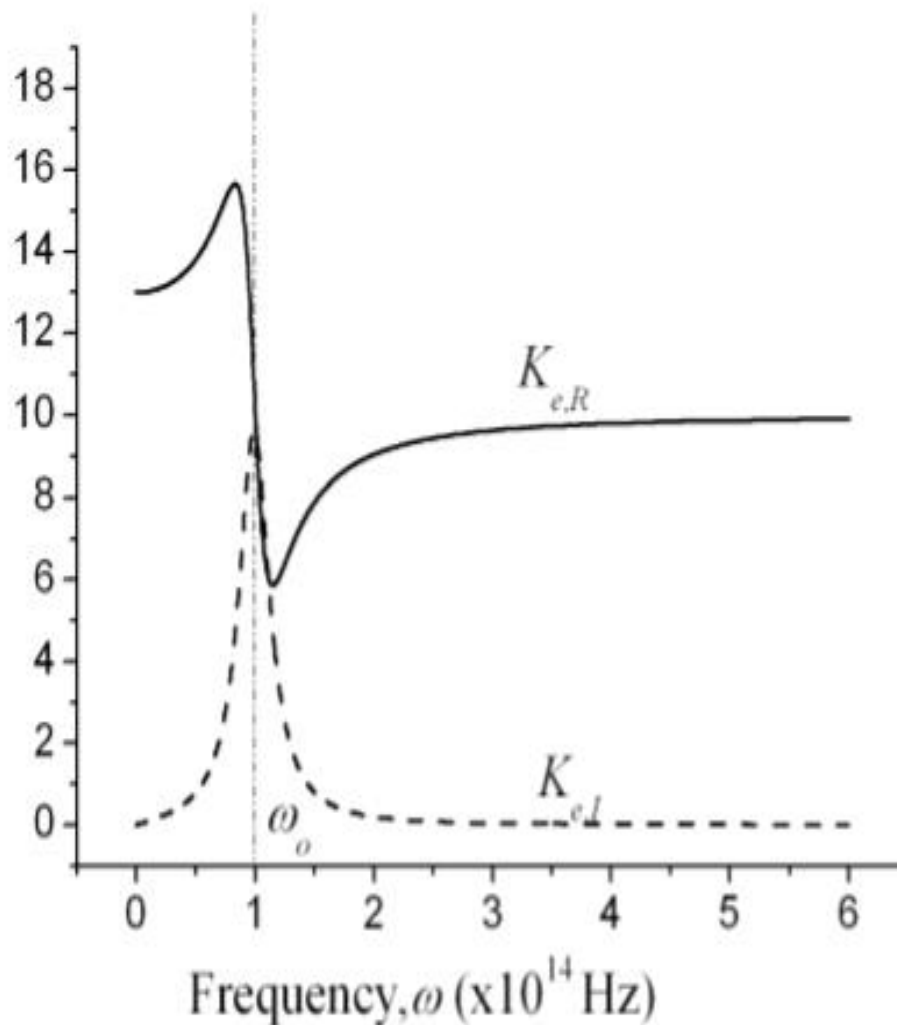


Figure 1.6 Dielectric function spectra of real ($K_{e,R}$) and imaginary ($K_{e,I}$) of single Lorentz model in terms of angular frequency in 10^{14} Hz⁶. Note the resonant frequency is located at 1 eV.

1.3.2 Drude Model

In this section, Drude model for free electron will be discussed. Different from Lorentz model that deals with the case of electrons bounded to the nuclei, Drude model assumes that the system is a conductor, in which electrons are free to move in the media^{1,7}. The motion of free electron is described by $\langle v \rangle$ and $\langle \tau \rangle$, the average drift velocity and the average scattering time of electron:

$$F_f = m^* \frac{dv}{dt} = m^* \frac{\langle v \rangle}{\langle \tau \rangle} \quad (1.33)$$

Where m^* is effective mass of electron. Let's assume that we shine light on metals. The motion of electron is now affected by applied AC electric field. Then, the equation of motion for free electrons become:

$$m^* \frac{dv}{dt} = -F_f + F_e = -m^* \frac{\langle v \rangle}{\langle \tau \rangle} + e * E_0 e^{i(kz - \omega t)} \quad (1.34)$$

Note the negative sign of F_f . This represents that the accelerated carriers lose their acceleration by scattering. Now, with the equation of motion, we can calculate dielectric function, by setting $\Gamma = \langle \tau \rangle^{-1,7}$:

$$\epsilon_1 = 1 - \frac{N_f e^2}{m \epsilon_0 (\omega^2 + \Gamma^2)} = 1 - \frac{\omega_p^2}{(\omega^2 + \Gamma^2)}, \quad \epsilon_2 = \frac{N_f e^2}{m^* \epsilon_0 \omega} \frac{\Gamma}{(\omega^2 + \Gamma^2)} \quad (1.35)$$

Where N_f is number of free electrons in the system. In the **Equation (1.35)**, there is an important quantity, $\omega_p^2 = N_f e^2 / (m^* \epsilon_0)$, which is called plasma frequency. This is the frequency at which free electron naturally oscillates without any external fields. Plasma frequency is very important quantity when explaining optical dielectric function spectra of metallic media. For metallic media, if we set $\Gamma = 0$ for idealistic case, plasma frequency is where real dielectric

spectra hits zero, as represented in **Figure 1.7**. Plasma frequency is also a standard point, below which reflection and absorption dominate, and above which transmission dominates. Having said this, if the frequency of the light is below the plasma frequency, the light will mostly be reflected or absorbed by the medium, whereas the light will mostly transmit through the metallic media if the frequency of the light is above the plasma frequency. Also, note that ϵ_2 , which is responsible for absorption, rapidly increases as we go to infrared range, and ϵ_1 decreases rapidly correspondingly.

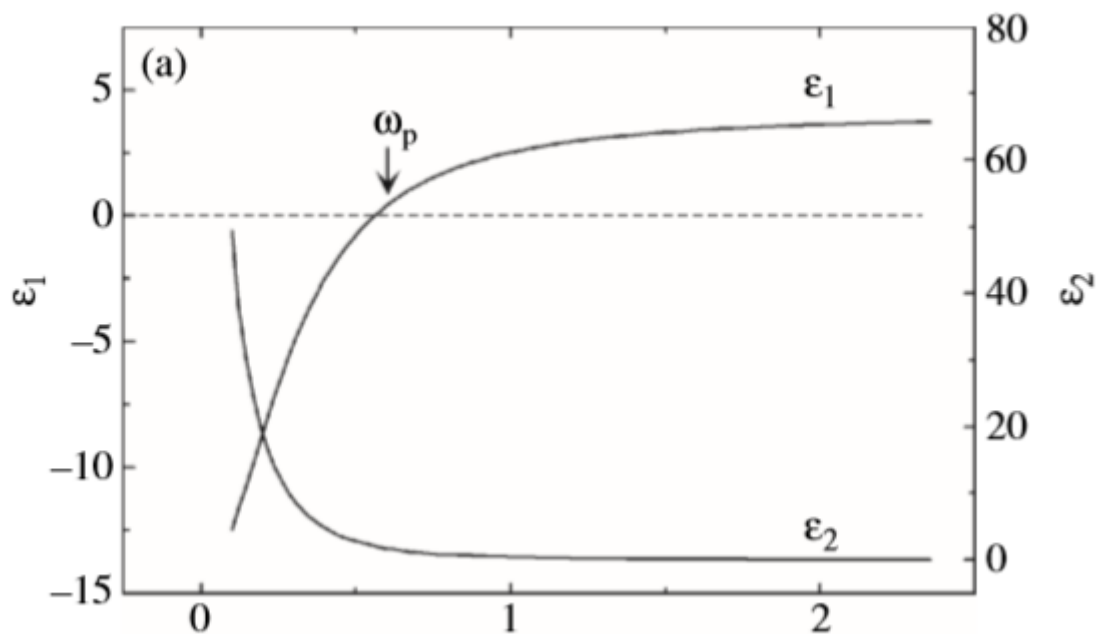


Figure 1.7. Optical spectra of Drude model⁷. Plasma frequency ω_p , is denoted as where real part of dielectric function ϵ_1 hits zero.

This is the general behavior of optical spectra of metals, and this is also called Drude tail. The reflectance spectra of common metals are represented in **Figure 1.8**. Note that the spectra are in terms of wavelength. As shown in **Figure 1.8**, most of the metals reflect light in visible range but are transparent in UV range (>300 nm).

We can also think of Drude model as a Lorentz model without a damping term. Note that in Lorentz model, the damping term arises due to damping of spring that connects the

bound electrons and the nuclei. However, since Drude model deals with the media with free electrons, there is no damping due to springs.

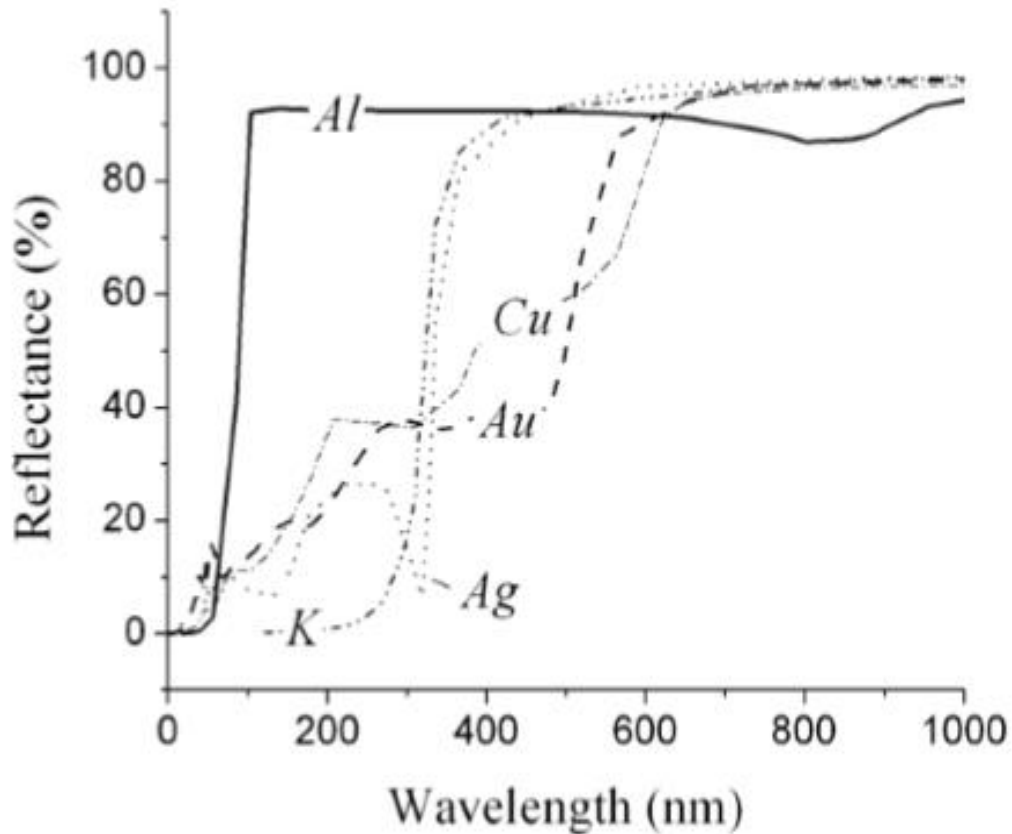


Figure 1.8. Reflectance (%) vs. wavelength of common metals⁸. Plasma frequency is the turning point of high and low reflection, where the slope of function gets infinite.

1.3.3 Tauc-Lorentz Model

Tauc-Lorentz model can be utilized for fitting ellipsometry spectra of amorphous materials⁹. Recently, this model has been applied to fit the ellipsometry spectra of transparent conducting materials¹⁰. When considering Tauc-Lorentz model, one can just simply think of it as general Lorentz model with asymmetric ϵ_2 peak. Note that, from **Chapter 1.3.1**, the imaginary part of dielectric function of Lorentz model has symmetric peak. The reason that Tauc-Lorentz model is usually applied to amorphous materials is that amorphous materials typically show asymmetric peak in ϵ_2 spectra. Tauc-gap ω_g , which represents asymmetry of

the absorption peak in imaginary dielectric function ε_2 , is given by the following equation:

$$\varepsilon_2 = \frac{A_{Tauc}(\omega - \omega_g)^2}{\omega^2} \quad (1.36)$$

Where ω is wavelength of light in eV, and A_{Tauc} is amplitude of Tauc gap. If we multiply **Equation (1.36)** to the imaginary part of **Equation (1.31)**, we will get the equation of ε_2 for Tauc-Lorentz model:

$$\varepsilon_2 = \frac{A\omega_0\Gamma(\omega - \omega_g)^2}{(\omega^2 - \omega_0^2)^2 + (\Gamma\omega)^2} \frac{1}{\omega} \quad (\omega > \omega_g), \quad (1.37)$$

$$0 \quad (\omega < \omega_g)$$

Where A denotes the amplitude of the peak. The real part of dielectric function of Tauc-Lorentz model is rather complicated, but it can be derived from well-known Kramers-Kronig relationship^{1,11}:

$$\varepsilon_1(\omega) = 1 + \frac{2}{\pi} P \int_0^{\infty} \frac{\omega' \varepsilon_2(\omega')}{\omega'^2 - \omega^2} d\omega' \quad (1.38)$$

Where P denotes principal value of integral, which is given by:

$$P \int_0^{\infty} d\omega' = \lim_{\delta \rightarrow 0} \left(\int_0^{\omega-\delta} d\omega' + \int_{\omega+\delta}^{\infty} d\omega' \right) \quad (1.39)$$

For more information on Kramer's Kronig relationship, you can read Kittel's *Introductions to Solid State Physics, 8th edition*¹¹. **Figure 1.9** shows dielectric function spectra of single Tauc-Lorentz model of amorphous silicon (a-Si). As shown in **Figure 1.9**, the absorption peak in imaginary dielectric function is not symmetric anymore. The real part of dielectric function looks very similar to that of general Lorentz model. We can treat Tauc-Lorentz model as Lorentz model and we can choose either of them to describe absorption peak. However, one has to make choice in that one has less fitting parameter to simplify the fitting

function, as Tauc-Lorentz model has one extra fitting parameter, Tauc gap, compared to Lorentz model.

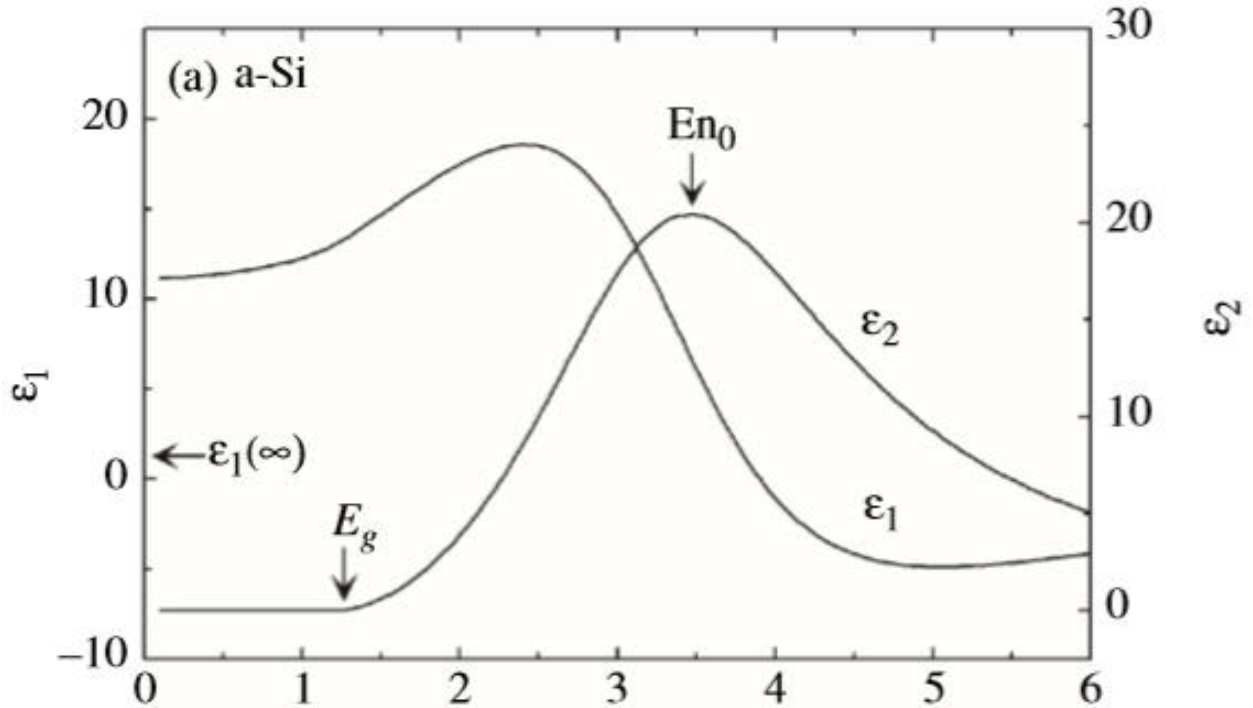


Figure 1.9. Tauc-Lorentz dielectric function spectra of amorphous silicon (a-Si)¹. Note that ϵ_2 peak is not symmetric anymore.

1.3.4 Sellmeier Model

Sellmeier model describes refractive index spectra of transparent materials^{1,4}. Since we assume that the media is transparent in this model, $\epsilon_2 = 0$. The equation of dielectric function of Sellmeier model can be described as:

$$\epsilon = \epsilon_1 = n^2 = A + \sum_j \frac{B_j \lambda^2}{(\lambda^2 - \lambda_{0j}^2)} \quad (1.40)$$

Where λ is wavelength. Sellmeier model is indeed very useful when modeling optical constants of thin film substrates, since most of them are transparent in visible range. With this model, one can simply obtain optical constants, since there are only two fitting parameters, A and B. Also, Sellmeier model can be used as pole equations, which describes the behavior of

real part of optical dielectric function that is not in the ellipsometry spectral range. I will discuss more on this model in the later section.

1.3.5 Drude-Lorentz Model

In section 1.3.2, we discussed Drude model for metallic media. In reality, Drude model itself is not enough to describe the optical constant spectra. For the ideal case, all the electrons in metal are free to move, but in reality, there are also some bound electrons that contributes to the dielectric function spectra. Hence, Drude-Lorentz model, which is combination of Drude and Lorentz model, is used to describe the optical dielectric function spectra of metallic media⁷. The equation for Drude-Lorentz model is just the summation of Drude and Lorentz model equations.

1.3.6 Interband Absorption: Band Structure and Density of States

When analyzing ellipsometry spectra, one can utilize band structure and density of states (DOS). For instance, let's consider calculated band structure and DOS of 2D correlated metal 1-T TiS₂, shown in **Figure 1.10 (a) and (b)**, respectively. 1-T represents trigonal unit cell described by one layer. In solid state physics, DOS represents number of states at different energy that electrons are allowed to occupy. In **Figure 1.10 (b)**, the vertical axis denotes number of states $N(E)$ and horizontal axis denotes the energy. Let's focus on the very bottom plot of **Figure 1.10 (b)**, which is denoted as "Total". We see that there are many peaks at each discrete level of energy. Let's consider that we shine light, which is electromagnetic wave, to the media. What happens next is that electrons in the media obtain energy from the light and start to excite. As a result, the electrons are allowed to hop from one available state to another available state. The energy difference of those states is where absorption occurs in the imaginary part of dielectric function in Lorentz or Tauc-Lorentz model. For this reason, it is very useful to obtain optical constant spectra in function of eV. Now, let's look at the band

structure, shown in **Figure 1.10 (a)**. The Fermi level is denoted as dotted line at 0 eV for convention. From elementary solid-state physics, we know that the band structure describes the metallic system, since we see no bandgap near Fermi level. The important fact of excitation of electrons is that hopping does not occur from unoccupied states to unoccupied states, from unoccupied states to occupied states, or occupied states to occupied states. The excitation only occurs from occupied to unoccupied states. We simply know that the Fermi level, which is denoted as dotted line in both **Figure 1.10 (a) and (b)**, is the highest level that electrons can occupy. Most of the calculations assume absolute zero temperature, but let's ignore this fact for simplicity. Therefore, in this case, we can think of the situation, where electrons are fully filled up to Fermi level. So, below Fermi level, the states are fully occupied by electrons and excitation does not occur. Also, above Fermi level, since all of the energy levels are unoccupied, the excitation does not occur between these energy levels. However, the excitation can occur from the energy below Fermi level to the energy above Fermi level. From this fact, we can conjecture where the excitation, or in other word, interband transition, occurs.

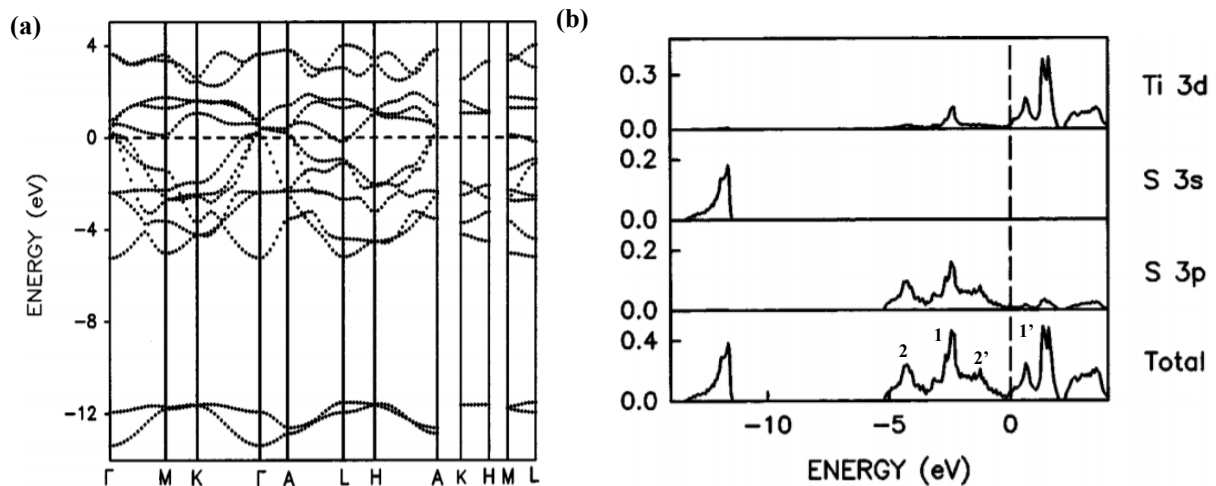


Figure 1.10 (a) Band structure and **(b)** Density of States (DOS) of 1-T phase TiS_2 ¹². The dotted line denotes 0 eV, which is Fermi level. In Figure 1.10 (b), the numbers denote specific DOS peak to explain interband transition in the text.

Now, let's look at the imaginary dielectric function spectra of 1-T TiS_2 determined from spectroscopic ellipsometry as a function of eV, shown in **Figure 1.11**. Drude tail is not

shown in this spectrum; it may be shown if the spectrum is in infrared regime. If we carefully look at the spectra, we notice that we have several ϵ_2 peaks. The peaks are located at about 1.1, 1.9, 3.3 and 3.8 eV. If we go back to the DOS plot shown in **Figure 1.10 (b)**, we can relate the absorption peaks to the ϵ_2 spectrum in **Figure 1.11**. The 1.1 eV peak can occur due to interband transition from any two energy levels very near the Fermi level. The 1.9 eV peak can occur due to transition from the two distinct DOS peaks (denoted as 1 and 2') across the Fermi level. The 3.3 and 3.8 eV peaks can occur between any energy levels or any DOS peaks across the Fermi level that have the corresponding energy differences. If we want to deduce in which specific band the transition occurs, we have to look at the DOS of each kind of band. For example, if we look at **Figure 1.10 (b)**, we have DOS for 3d band from Ti atom, 3s band from S atom, and 3p band from S atom. Let's choose the case of 3.3 eV absorption. If we see total DOS, 3.3 eV excitation can occur from the DOS peak right below the Fermi level, denoted as 1, to the largest DOS peak above the Fermi level, denoted as 1', or it can occur from the largest DOS peak below the Fermi level, denoted as 2 to the small DOS peak right above the Fermi level, denoted as 2'. If we carefully look at the 3p band of S, we notice that the DOS peaks 1 and 2 in total DOS belong to the 3p band. Also, we can notice that 1' and 2' peaks belong to 3d bands of Ti. Therefore, we can assume that the absorption peak at 3.3 eV, which is due to 1 to 1' or 2 to 2' transition, occurs due to interband transition of electrons from 3p band of S anion to the 3d band of Ti cation.

With band structure and DOS plots, we can deduce the energy gap between which the interband transition occurs. Due to this fact, the band structure, along with DOS plot, is very useful for analysis of ellipsometry data. However, we can't determine the exact wavevector, at which the band transition occurs. Frankly speaking, for the case of 3.1 eV transition, it can occur anywhere the energy gap is 3.3 eV between 3p and 3d bands. It is rather a matter of probability.

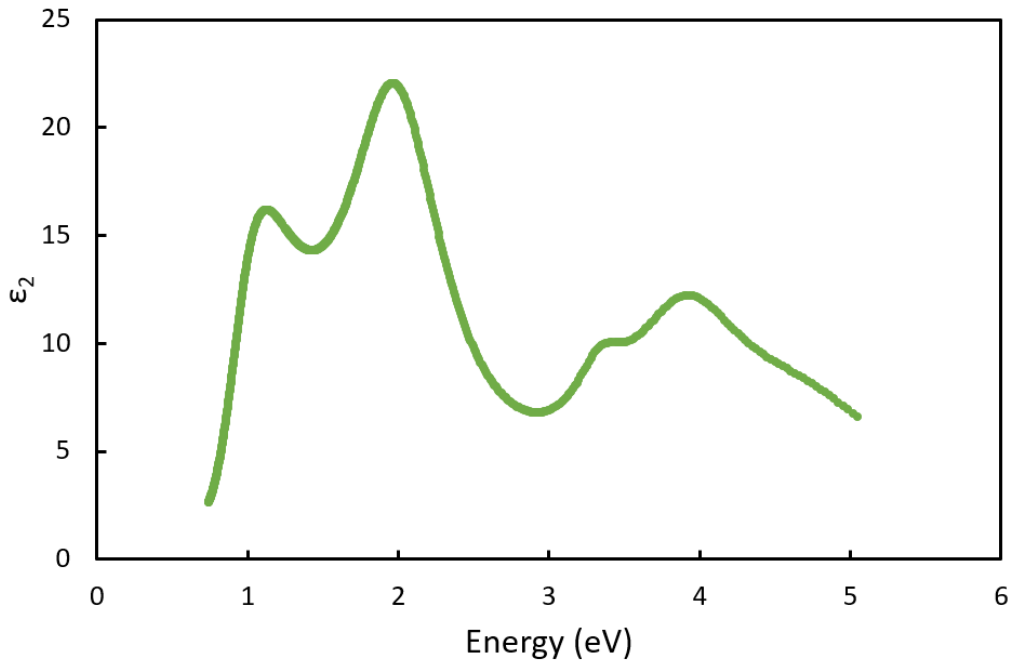


Figure 1.11 Imaginary optical dielectric constant (ϵ_2) of 1-T TiS₂ as a function of energy (eV), determined from spectroscopic ellipsometry.

1.3.7 Effective Medium Theories

When analyzing ellipsometry data, one should be careful of surface roughness or interface roughness of the sample, since the data is very sensitive to these factors^{1,4}. Therefore, it is important to incorporate these structures into optical model in ellipsometry data analysis. There are two general models for surface roughness characterization: Maxwell-Garnett and Bruggeman, which is also called Effective Medium Approximation (EMA). The derivations of these two models will briefly be discussed in this section.

1.3.7.1 Maxwell-Garnett

Let us consider a spherical dielectric sandwiched by a capacitor, shown in **Figure 1.12 (a)**. If a capacitor is connected to an electrical source, it will generate an electric field across the two electrodes of the capacitor. The spherical dielectric then will have polarization charges in the outer surface. Consequently, the atoms inside the sphere will receive an electric field

induced by these polarization charges, in addition to the external electric field. Let the applied electric field by capacitor be E , and the electric field induced by polarization charges be E' . Considering the spherical geometry of dielectric, as shown in **Figure 1.12 (b)**, the equation for E' is given by:

$$E' = \int_0^\pi r^{-2} (2\pi r \sin\theta) (rd\theta) (P \cos\theta) (\cos\theta) = \frac{4\pi P}{3} \quad (1.41)$$

Where r is radius of the sphere, θ is polar angle in spherical coordinate (should not be confused with azimuthal angle ϕ), and P is induced dielectric polarization induced by polarization charges in the outer surface. The electric field E' is also called Lorentz Cavity Field. The final expression in **Equation (1.41)** is in terms of Gaussian CGS unit. If we directly convert this expression to SI unit, simply $4\pi \rightarrow 1/\epsilon_0$, we have $4\pi P/3 = P/(3\epsilon_0)$. Therefore, the total electric field, $E+E'$, can be represented as:

$$E_{\text{total}} = E + \frac{P}{3\epsilon_0} \quad (1.42)$$

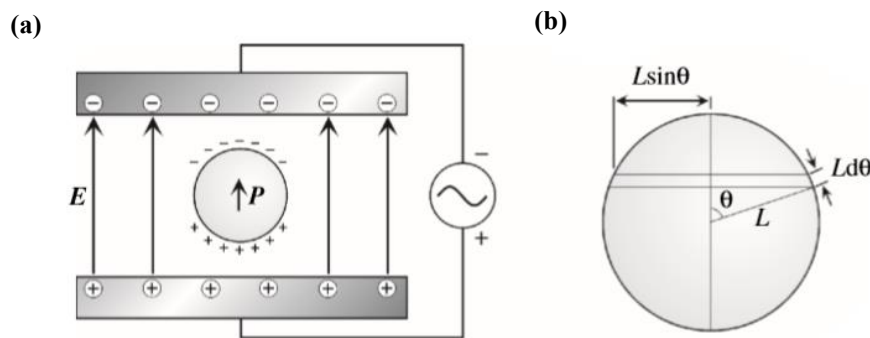


Figure 1.12 (a) spherical dielectric surrounded by a capacitor. The polarization arises due to external electric field generated by capacitor and surface polarization charge and **(b)** Spherical geometry of dielectric. L is the radius of the sphere, which is denoted by r in Equation (1.38)¹.

Here, we know that $P = N_e \alpha E_{\text{total}}$, where N_e is number of electrons in the system and α is polarizability. By plugging this expression into **Equation (1.39)**, it yields:

$$P = N_e \alpha E / \left(1 - \frac{N_e \alpha}{\epsilon_0}\right) \quad (1.43)$$

If we relate **Equation (1.43)** to **Equation (1.29)**, we have a formula called Clausius-Mossotti relation:

$$\frac{\epsilon - 1}{\epsilon + 2} = \frac{N_e \alpha}{3\epsilon_0} \quad (1.44)$$

The EMA generally assumes that the media is composed of two different phases. For surface roughness characterization, we assume that the media is composed of two different phases, the material and void. Let's assume that the above spherical dielectric is composed of two phases, simply called a and b. Then from **Equation (1.44)**, we obtain:

$$\frac{\epsilon - 1}{\epsilon + 2} = \frac{(N_a \alpha_a + N_b \alpha_b)}{3\epsilon_0} \quad (1.45)$$

If we rewrite Equation (1.42) in terms of volume fraction of each phase, we get:

$$\frac{\epsilon - 1}{\epsilon + 2} = f_a \frac{\epsilon_a - 1}{\epsilon_a + 2} + (1 - f_a) \frac{\epsilon_b - 1}{\epsilon_b + 2} \quad (1.46)$$

Where f denotes volume fraction, and ϵ_a and ϵ_b denotes dielectric constants of phase a and b, respectively. **Equation (1.46)** is called Lorentz-Lorentz relation. If we assume that the spherical dielectric is surrounded by some host materials with dielectric constant of ϵ_h , **Equation (1.46)** turns into the form:

$$\frac{\epsilon - \epsilon_h}{\epsilon + 2\epsilon_h} = f_a \frac{\epsilon_a - \epsilon_h}{\epsilon_a + 2\epsilon_h} + (1 - f_a) \frac{\epsilon_b - \epsilon_h}{\epsilon_b + 2\epsilon_h} \quad (1.47)$$

In Maxwell-Garnett model of EMA, we assume that $\epsilon_a = \epsilon_h$. With this assumption, we have the following equation:

$$\frac{\epsilon - \epsilon_h}{\epsilon + 2\epsilon_h} = f_a \frac{\epsilon_a - \epsilon_h}{\epsilon_a + 2\epsilon_h} + (1 - f_a) \frac{\epsilon_b - \epsilon_h}{\epsilon_b + 2\epsilon_h} \quad (1.48)$$

The Maxwell-Garnett model assumes that one phase is surrounded by the other phase, and their

volume ratio determines the volume fraction f_a . Even though Maxwell-Garnett well explains the case of two separated phases in the media composed of two different phases, there are some limitations. As we can easily notice from **Equation (1.48)**, if one exchange ε_a and ε_b , the case when the phase a is surrounded by the phase b, the resulting dielectric constant ε will be totally different. Therefore, one has to assume that the volume fraction of one phase dominates over the other, so that the proper choice of host dielectric constant should be made. Also, since Maxwell-Garnett assumes that one phase is surrounded by the other, the model cannot solely explain the media that is composed of mixture of two phases.

1.3.7.2 Bruggeman

Most of the surface roughness characterization of ellipsometry data follows Bruggeman model for effective medium theory. Bruggeman model is also called Effective Medium Approximation (EMA). From **Equation (1.46)**, Bruggeman model rather assumes that $\varepsilon = \varepsilon_h$, which, in turn, gives:

$$f_a \frac{\varepsilon_a - \varepsilon}{\varepsilon_a + 2\varepsilon} + (1 - f_a) \frac{\varepsilon_b - \varepsilon}{\varepsilon_b + 2\varepsilon} = 0 \quad (1.49)$$

The Bruggeman model assumes that two different phases in the media are randomly mixed. Therefore, the volume fraction f_a also denotes the probability of finding each phase in the media. This model can be incorporated into describe the media that is composed of more than two different phases:

$$\sum_{i=1}^n f_i \frac{\varepsilon_i - \varepsilon}{\varepsilon_i + 2\varepsilon} = 0 \quad (1.50)$$

Figure 1.13 (a) and (b) schematically show the case of Maxwell-Garnett model and Bruggeman model, respectively, in the case of two different phases in the media. As shown in **Figure 1.13 (a)**, Maxwell-Garnett model assumes that one phase is surrounded by the other,

and the grains of surrounded phase is separated by the other phase. However, as shown in **Figure 1.13 (b)**, Bruggeman model assumes that the media is rather composed of mixture of two different phases. The volume fraction denotes the probability of having each phase in the media.

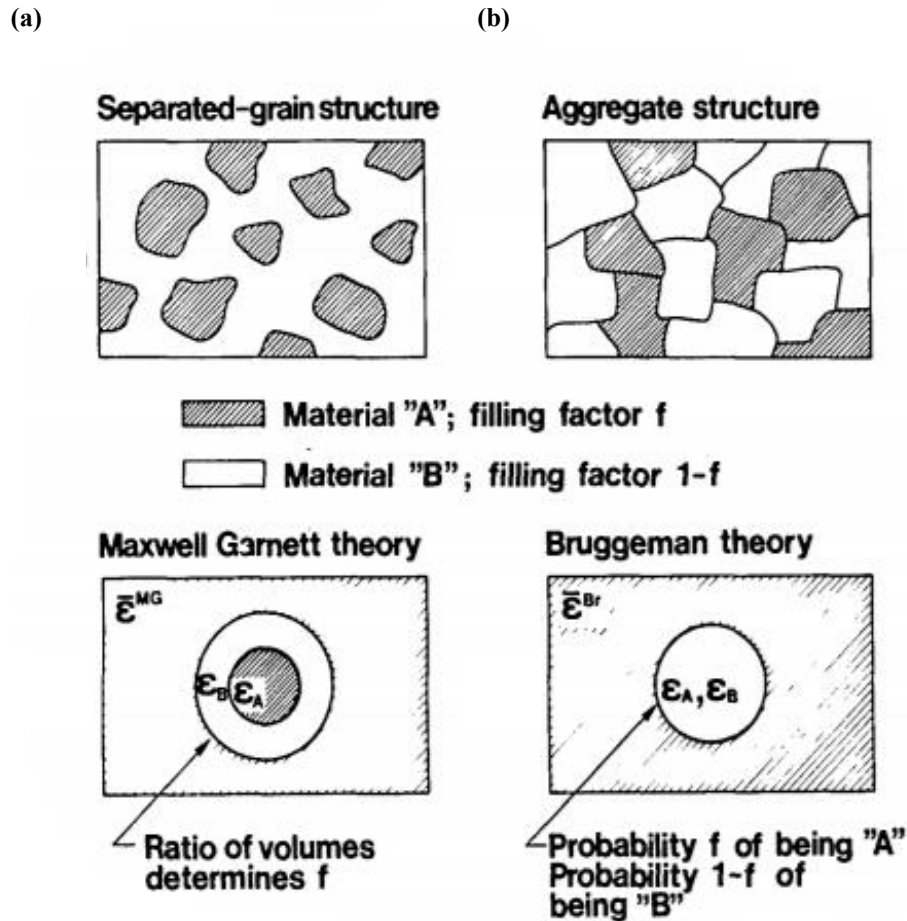


Figure 1.13 (a) Schematics of Maxwell-Garnett model and (b) Schematics of Bruggeman Effective Medium Approximation¹³.

1.4 Ellipsometry Measurement Method

In this section, experimental procedure of ellipsometry will be discussed. The method proper sample preparation for single crystals and thin films, calibration and data acquisition with J.A.Woollam's M-2000 ellipsometry and CompleteEase software will be discussed⁴. There are also many types of ellipsometry and corresponding software that are commercially available by other companies besides J.A.Woollam. For different types of ellipsometers which

are not discussed in this chapter, one should carefully read the corresponding manual to properly operate them.

1.4.1 Sample Preparation

A proper preparation of sample is needed prior to any ellipsometry measurement. For reflection geometry, the sample should have smooth and reflecting surface. If the surface of the sample is too rough, the light will barely be reflected from the sample surface and ellipsometer cannot detect the reflected light.

Different types of samples need different method of preparation. If the sample is single crystal, one can find a way to cleave the crystal to get a clean and smooth surface. If it is not possible to cleave the single crystal sample, one should polish the sample surface. If one has thin film sample, one does not need to polish the surface of the thin film, since it generally has very smooth and reflecting surface. However, one should make sure that the back side of the substrate is grinded, so that there is no reflection from it. If the back side of the substrate is not grinded, the ellipsometry will detect the reflected light not only from the surface, but also from the back side of the substrate, as shown in **Figure 1.14 (a)**. This reflected light from the back side of the substrate will give much complexity when analyzing the data.

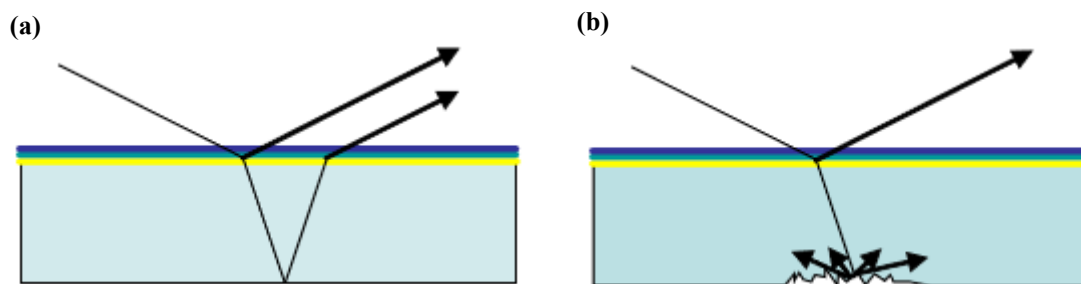


Figure 1.14 Light propagation in multilayer sample when (a) light is reflected from both the surface and back side of the substrate and (b) the light is scattered by rough surface of back side of the substrate⁴.

1.5 Data Analysis

For analyzing ellipsometry data, one can either make use of their own coding, or utilize

specific software. There are several softwares that are available commercially. One can choose any software that fits to one's taste. For this section, Method of utilizing CompleteEase software for ellipsometry data analysis will be discussed. The modeling can also be done with WVASE software, which is also provided by J.A.Wollam. The detailed measurement method with M-2000 Ellipsometry (J.A.Woollam) and measurement and fitting method with CompleteEase software are described in the Appendix of the thesis.

The data analysis is composed of three steps. First, the layer model should be defined. For example, if one wants to analyze ellipsometry raw data for single crystal, the layer optical model should be composed of air, surface roughness and the sample. If one wants to analyze the data for thin film sample, the layer optical model should be composed of air, surface roughness, film and the substrate. One should also consider if any anisotropy exists for each layer, or if any layer is graded.

Second, one should assign optical functions to each layer. In order to do so, one should know the physical properties of each layer. For example, in the case of single crystal, if the sample is an insulator, one must utilize Lorentz or Tauc-Lorentz model. If the sample is a metal, one must apply Drude-Lorentz model. After determine which model to use for analyzing ellipsometry data, one should know the strength of the oscillators. This can be determined from calculated band structure and DOS plots or calculated optical dielectric function spectrum. One should also consider film thickness, which can be determined from X-ray Diffraction method. Lastly, one should also consider surface roughness, which can be modeled by Bruggeman effective medium approximation. The analysis of surface roughness can be done based on atomic force microscopy (AFM) technique. By considering surface roughness and surface morphology, one should determine the thickness of surface roughness layer and ratio of air and film in the roughness.

Lastly, one should fit the data by adjusting fitting parameters and minimize mean-square error (MSE). For example, Drude model has two fitting parameters: resistivity and electron scattering time. Lorentz model has three fitting parameters: amplitude, broadness and central energy (position of the peak). Tauc-Lorentz, compared to Lorentz model, has extra fitting parameter, called Tauc-Gap. The acceptable MSE should be less than 10, and it is lower the better. After finishing the fitting, one should evaluate the fitting. If the fitting result does not physically make sense, for example, one of the oscillators has negative amplitude or has central energy that is out of the spectral range, or layer thickness is negative, the fitting is meaningless. Once one finds that the fitting is meaningless, one should redo the fitting, so that all the fitting parameters make sense.

Chapter 2 Transparent Conducting Correlated Metal SrNbO₃

2.1 Correlated Electron System

Correlated electron materials refer to the system, in which the interactions among electrons, mostly coulombic repulsion, dominates the physical properties. Note that conventional theory of semiconductors and metals relies on the consideration of individual, non-interacting electrons. Some of the emerging physical phenomena, such as Mott insulating phase^{14,15}, colossal magnetoresistivity^{16,17} and high-temperature superconductivity¹⁸ that cannot be explained by conventional theory of solid-state physics, can be explained by electron correlation.

In correlated metals, coulomb interactions among electrons cannot be treated as being negligibly small. The coulombic interactions among electrons can yield the electronic structures that deviates from speculations of non-interacting band structures. If, taken to the extreme, electron correlation tends to localize all the electrons, the system becomes an insulator (Mott insulating phase). However, If the correlation does not reach the extreme, the system maintains metallic conductivity even though electron correlation still exists.

The strength of electron correlation can be determined by the factor called renormalization factor Z_k . Z_k is the ratio m^*/m_{band}^* , where m^* is enhanced electron effective mass by electron correlation, and m_{band}^* is effective mass with no correlation, determined by conventional band theory. In the case of Mott insulating phase, in which all the electrons are localized, Z_k is equal to 0; in the case of no electron correlation, Z_k is equal to 1. **Figure 2.1** shows several correlated electron systems, with their electrical conductivities and renormalization factor Z_k . Note that Z_k for correlated metals is close to 1, these for correlated metals lie between 0.1 to 0.8, and these for Mott insulator lie at 0. Also, note that most of the correlated electron systems, even in vicinity of Mott insulator, possess metallic conductivity.

There are a number of types of correlated electron systems including transition metal oxide¹⁹⁻²², iron pnictides²³⁻²⁵, and transition metal dichalcogenides^{26,27}.

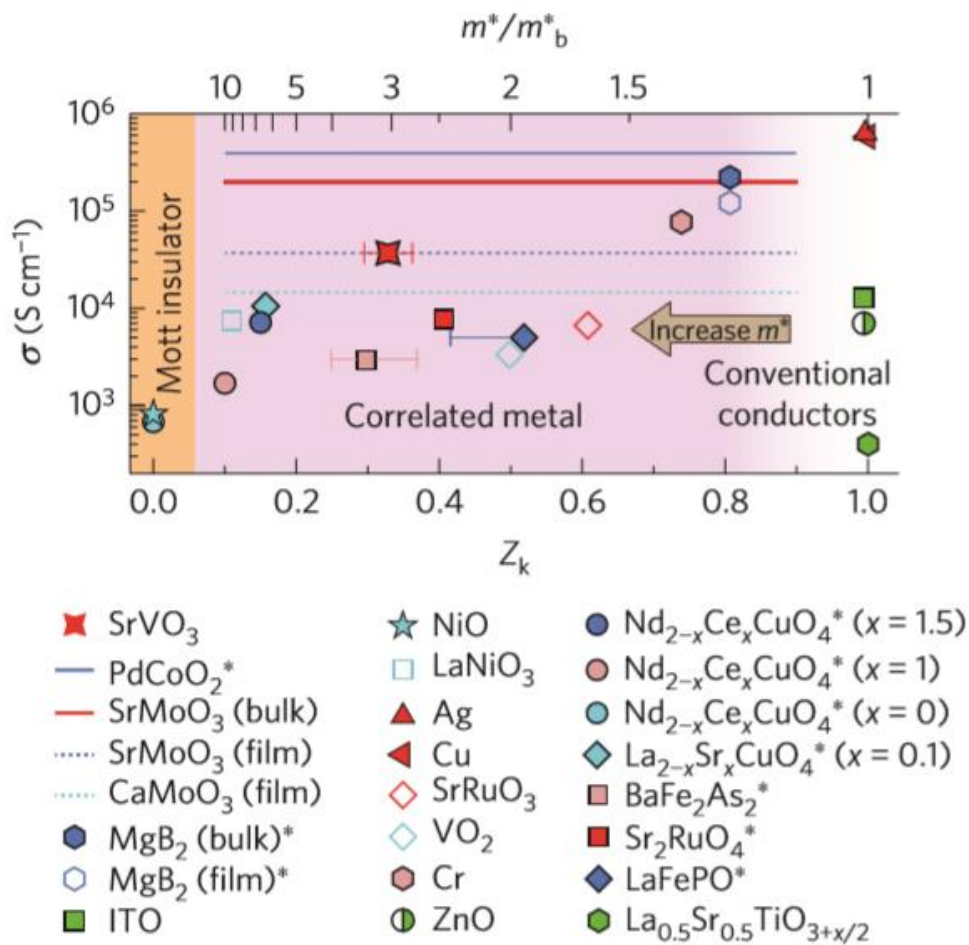


Figure 2.1 Electrical conductivity (σ) as function of renormalization factor Z_k of several metallic system²⁸. Note that conventional conductors have $Z_k = 1$, whereas correlated electron systems have $Z_k < 1$.

2.2 Transparent Conductors

Transparent conductors refer to the class of material that exhibits both high electrical conductivity and optical transparency. Due to their unique properties, they are being utilized in a variety of optoelectronic applications, such as liquid crystal display, photovoltaic cells, solid-state lighting, and smart windows. In general, it is very challenging to obtain both high electrical conductivity and optical transparency. The reason can be explained when comparing the properties of both metals and insulators. We all know that metals are composed of sea of

free electrons thus they have high electrical conductivity. However, as already discussed in **Chapter 1.3.2**, almost all of the metals absorb or reflect visible light, due to the fact that they have plasma frequency in deep UV regime. Metals tend to absorb and reflect light when the light has frequency below the plasma frequency and tend to transmit the light when the light has frequency above the plasma frequency. Meanwhile, many insulators or semiconductors have optical transparency in the visible regime. This is because they have wide bandgaps, so that interband absorptions occur at the high energy, usually in UV regime. However, insulators, as discussed in **Chapter 1.3.1**, have very low conductivity, due to the fact that electrons are bounded to the nuclei and not free to move around.

Conventionally, researchers tried to obtain both high electrical conductivity and optical transparency by degenerately doping high-bandgap semiconducting materials. First, the host material of wide bandgap semiconductor is chosen so as to ensure optical interband transition occurring above the visible range (> 3.25 eV). Then, the dopant concentration is maximized to obtain the optimal electrical conductivity. Most of the chosen host materials are called transparent conducting oxides (TCOs), which consist of post transition metal cations, such as Sn^{4+} , Zn^{2+} , and Cd^{2+} . The so-called post transition metals possess spatially spread vacant s-orbitals, which form largely disperse conduction bands with small electron effective mass²⁹. Among TCOs, indium-tin oxide (ITO) is the most widely used as transparent conductors, with high electrical conductivity ($5\text{-}10 \times 10^3$ S/cm) and optical transparency in the visible range ($1.7 - 3.25$ eV)³⁰. However, there exists the problem with ITO. **Figure 2.2 (a)** shows the abundance of elements in Earth crust. The elements in green area are called “rock-forming elements” which represents most abundant elements, and the elements in yellow area are called “Rarest metals” which denotes the least abundant elements. As shown in the figure, indium lies right above the yellow area, which are the least abundant elements. **Figure 2.2 (b)** shows indexed demand of indium, with the value in 1994 as the standard point of 100. This figure shows that

the demanding has been dramatically increased due to the usage of indium to ITO. Based on two figures, it is obvious that the increasing demanding with limited resource of indium is most likely to cause the scarcity of indium, which in turn will dramatically increase the price of ITO. Therefore, alternatives are significantly needed that can benchmark against ITO in terms of “performance” and “cost-effectiveness”. Nowadays, there are a number of design strategies for transparent conductors including ultrathin metallic thin films, metallic nanowires, other TCOs, and correlated metals. In the following chapters, pros and cons of these alternatives will be further discussed.

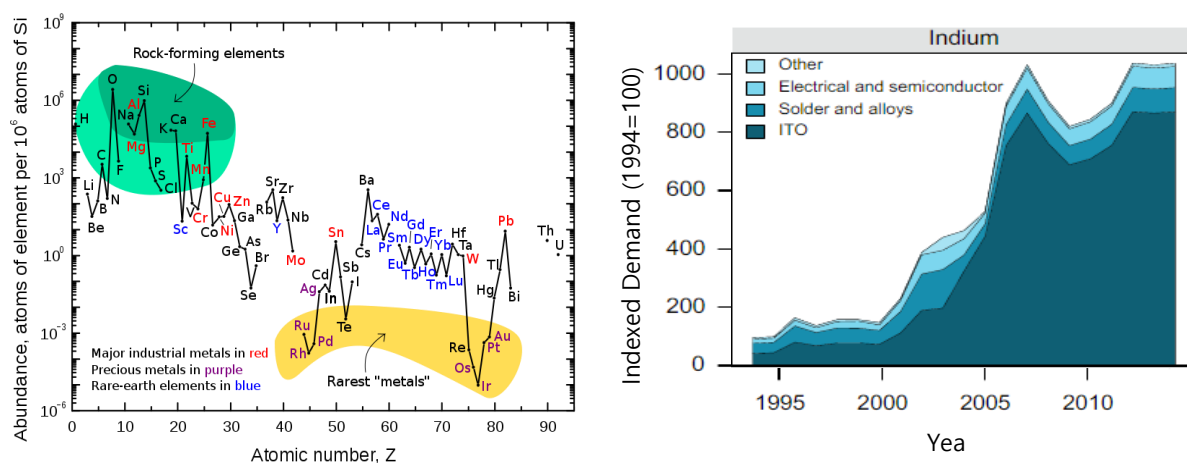


Figure 2.2 (a) Abundance of elements in Earth crust in function of atomic number Z and (b) indexed demanding of indium as function of year.

2.2.1 Ultrathin Metallic Film

There are several reports on ultrathin metallic thin film composed of conventional metals, such as silver (Ag) or gold (Au), can be used as transparent electrode in optoelectronic devices^{31,32}. The positive aspect of ultrathin metallic films is that they have high electrical conductivity. Note that silver is the most conductive materials by so far. However, as one tries to reduce thickness for more transparency, electrical conductivity of ultrathin metallic film tends to decrease, because of surface scattering of electrons. The electron mean-free path

(EMFP) is an important factor that determines whether the system undergoes electron surface scattering in a certain film thickness. EMFP is given by the following expression³³:

$$\Lambda = \hbar(3\pi^2)^{\frac{1}{3}}(\tau/N_f^{\frac{2}{3}})(N_f/m^*) \quad (2.1)$$

Where \hbar is reduced Planck constant, τ is scattering time of electron, N_f is number of carrier, so called carrier concentration, and m^* effective mass of electron. The EMFP of Ag and Au is 52 nm and 50 nm, respectively. This means that if the film thickness is below ~ 50 nm, the scattering of electrons drastically increases. The scattering of electrons adversely affects the conductivity of the system.

Also, for metallic thin films, there exists percolation limit. If one tries to sputter metallic thin film below the percolation limit, one faces challenge to grow smooth and uniform thin films due to their preference for Vollmer-Weber growth mode. This means that aggregated islands of the metals are formed instead of uniform thin metallic film. Since the films are not uniform anymore, the resistivity of metallic films below percolation threshold tends to be much less than that of bulk, and they can even have insulating behavior³⁴⁻³⁶. Furthermore, island growth mode prevents the metallic thin film below percolation limit from having optical transparency, since the light can be more absorbed and scattered by ununiform surface of aggregated islands of the metals³⁷.

2.2.2 Metallic Nanowires

It has been recently reported that metallic nanowires, especially silver nanowires, can be used as transparent conductors³⁸⁻⁴¹. They can possess high electrical conductivity and optical transparency at the same time. Furthermore, due to their flexibility, they can be utilized in the flexible organic light emitting diode (OLED) display panel. However, metallic nanowires face to several critical problems, such as high contact resistance between many wires, percolation

problem, which requires a long, thin and smooth wires that imposes the significant challenges on finding cost-effective synthesis method, long-term stability, and high contact resistance between wires and the active electronic materials⁴²⁻⁴⁵.

2.2.3 Transparent Conducting Oxides (TCOs).

There have been many attempts to obtain transparent conductor by degenerately doping wide-bandgap semiconductors. These wide-bandgap materials consist of oxide semiconductors, such as In_2O_3 , ZnO , and CdO ²⁹. While the most widely used TCO is ITO, there are several other TCOs, such as Al- and Ga-doped ZnO ⁴⁶, Ga- and In-doped CdO ⁴⁷, and Sn-doped $\beta\text{-Ga}_2\text{O}_3$ ^{48,49}.

Widely known problem for TCOs is that the conductivity and optical properties heavily depend on the growth method^{30,48}. Therefore, one must obtain optimal growth method and conditions, which are hard to achieve in general. Furthermore, doping solubility limit prevents TCOs from possessing carrier concentration above the order of $10^{21} /\text{cm}^3$, and the highest conductivity that ITO, the most widely used TCO, can achieve is in the order of $5\text{-}10 \times 10^3 \text{ S/cm}$ ^{30,46}, which is 2 orders lower than those of metals. If one ignores the solubility limit just in order to increase conductivity when growing films, there exists a possibility that the films can lose optical transparency^{30,42,48}.

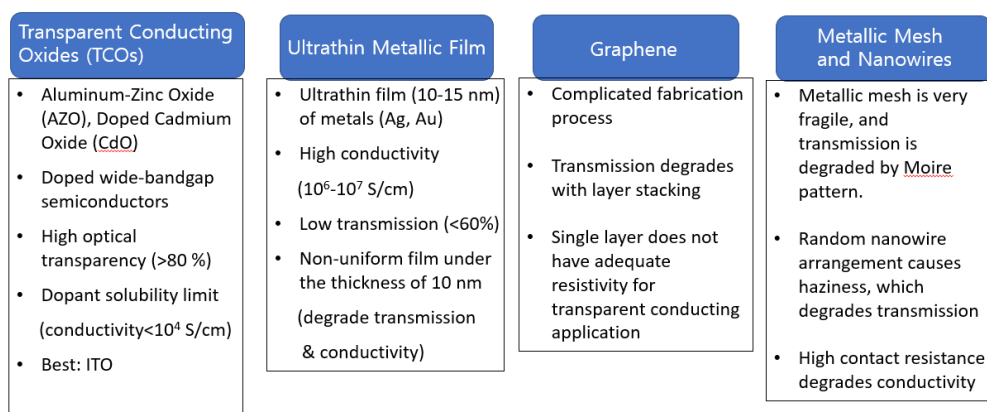


Figure 2.3 Comparative chart for candidates of transparent conductors: transparent conducting oxides (TCOs), ultrathin metallic film, graphene, metallic mesh and nanowires.

2.2.4 Figure of Merit (Φ_{TC})

Figure of Merit (Φ_{TC}), refers to the performance of transparent conductor. Φ_{TC} is determined by two important factors, optical transmission (T) and sheet resistance (R_s). Φ_{TC} can be expressed by the following equation, proposed by Haccke⁵⁰:

$$\Phi_{TC} = T^{10}/R_s \quad (2.2)$$

Also, there exists another expression for figure of merit⁵¹, which is:

$$\Phi_{TC} = \frac{\sigma}{\alpha} \quad (2.3)$$

With conductivity σ and absorption coefficient α . However, this expression is not accurate in that it can overestimate the performance of transparent conductors. For example, consider the case of very thick (1 mm) silver film and 40 nm of ITO. Let's fix α by taking average value from 400 – 700 nm, since α is the function of wavelength. If we calculate figure of merit for each case based on this formula, we have 0.755 S and 0.86 S for silver and ITO, respectively. According to this expression, performance of 1 mm of silver is similar to that of 40 nm ITO. It is very obvious that 1 mm of silver film cannot even be used as transparent conductor, since it is not transparent at all. This overestimation of figure of merit is due to that the expression does not consider the film thickness and only consider intrinsic properties.

The optical transmission T can be determined from the optical constants of the materials determined by spectroscopic ellipsometry. The absorption coefficient α can be determined by:

$$\alpha = \frac{4\pi k}{\lambda} \quad (2.4)$$

Where k is extinction coefficient and λ is the wavelength of the light. Considering the case of freestanding thin film, sandwiched by two dielectric media (air) with the normal incidence of

light, the optical transmission is given by⁵²:

$$T = \frac{I}{I_0} = \frac{(1 - R)^2 + 4R\sin^2\Psi}{e^{\alpha t} + R^2e^{-\alpha t} - 2R\cos 2(\Psi + \Phi)} \quad (2.5)$$

Where t is the film thickness, R is normal incidence reflectivity, which is expressed in terms of refractive index n and extinction coefficient k :

$$R = \frac{(n - 1)^2 + k^2}{(n + 1)^2 + k^2} \quad (2.6)$$

With Ψ and Φ given by:

$$\Psi = \frac{4\pi n t}{\lambda}; \quad \Phi = \tan^{-1} \frac{2k}{n^2 + k^2 - 1} \quad (2.7)$$

The term $2R\cos 2(\Psi + \Phi)$ takes into account the fact that there exists an interference arising from upper and lower interfaces of the film.

As mentioned in **Chapter 2.2.1**, electron tends to have surface scattering if the thickness of the film is in vicinity of EMPF. When considering sheet resistance R_s of thin film, one must take into account of the effect of surface scattering and grain boundary scattering of electrons on the resistivity. The following equation for conductivity in the consideration of surface scattering effect was proposed by Fuch⁵³ and Sondheimer³³:

$$\sigma_{FS} = \sigma_0 \left[1 - \frac{3(1 - p)}{2\kappa} \int_1^\infty \left(\frac{1}{\xi^3} - \frac{1}{\xi^5} \right) \frac{1 - e^{-\kappa\xi}}{1 - p e^{-\kappa\xi}} d\xi \right] \quad (2.8)$$

Where σ_0 is bulk conductivity, ξ is integration parameter that vanishes after the integration, κ is normalized length, defined by $\kappa = t/\Lambda$, and p is electron/surface reflection coefficient, ranging from 0 to 1. In the case of electrons diffused by the surface, p is 0, and in the case of elastic scattering of electrons, p is 1. Mayadas and Shatzkes⁵⁴ further expanded Fuch and Sondheimer model by considering background scattering, grain boundary scattering, and external surface scattering. Mayadas and Shatzkes model is given by:

$$\sigma_{MS} = \sigma_0 \left[1 - \frac{3}{2}\zeta + 3\zeta^2 - 3\zeta^3 \ln \left(1 + \frac{1}{\zeta} \right) \right]; \quad \zeta = \frac{\Lambda}{D} \frac{R}{1-R} \quad (2.9)$$

Where D is average grain size and R is reflection coefficient of electron/grain boundary.

Conductivity can be converted to resistivity with the following relationship:

$$\rho = \frac{1}{\sigma} \quad (2.10)$$

The total resistivity with the consideration of both surface scattering effect and grain boundary effect is then:

$$\rho_{total} = \rho_{FS} + \rho_{MS} - \rho_0 \quad (2.11)$$

The sheet resistance is defined by:

$$R_s = \rho_{total}/t \quad (2.12)$$

The expression for Figure of Merit Φ_{TC} has two variables: film thickness t and wavelength λ . If one wants to obtain Φ_{TC} in the visible range in terms of film thickness, one should take the average values of transmission (done by integration) over the visible range (400 – 800 nm). If one wants to obtain Φ_{TC} in terms of wavelength, the film thickness should be fixed.

2.2.5 Key Descriptors for Transparent Conductors

The Figure of Merit Φ_{TC} depends on the following four descriptors: Conductivity:

$\sigma = \frac{e^2 \tau N_f}{m^*}$, electron mean-free path (EMFP): $\Lambda = \hbar(3\pi^2)^{\frac{1}{3}}(\tau/n^{\frac{2}{3}})(N_f/m^*)$, plasma energy:

$\hbar \sqrt{\frac{N_f e^2}{m^* \epsilon_0 \epsilon_r}}$, and interband absorption. The variables for the descriptors are already shown in the

previous chapters. In order to assure high Φ_{TC} , the conductivity should be higher than 10^4 S/cm, which is maximum conductivity that ITO can achieve. The EMFP should be less than 10 nm, in order to prevent dramatic degradation of conductivity of thin film that has thickness in

vicinity of EMFP or lower than EMFP. The plasma energy should sit below red energy (1.77 eV) and strong interband absorption should sit above purple energy (3.1 eV) in order to assure optical transparency in the visible range. These requirements immediately reveal potential trade-off. The three key descriptors, conductivity, EMFP and plasma energy depend on the ratio of carrier concentration n and effective mass of electron m^* . In order to achieve high conductivity, this ratio should be maximized; however, since EMFP and plasma energy should be minimized, this ratio should also be minimized. This trade-off shows that satisfying the requirements to optimize Φ_{TC} is indeed challenging. These key descriptors for transparent conductors will further be discussed in the later chapter.

Key Descriptors

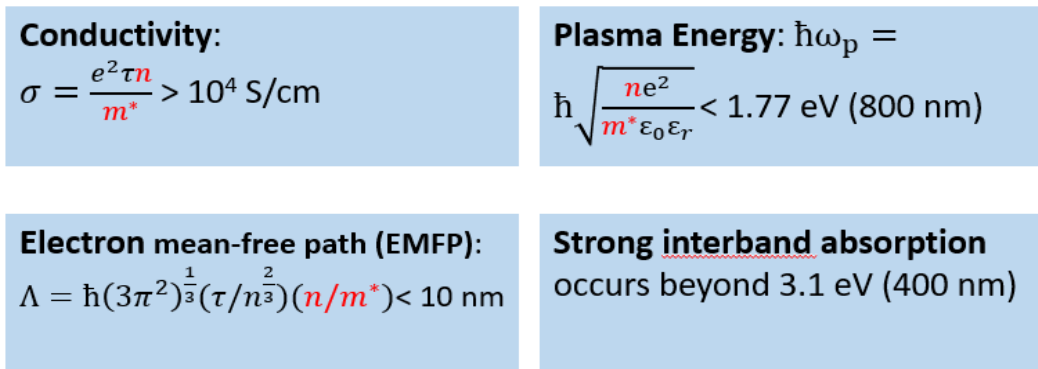


Figure 2.4 Key descriptors for figure of merit of transparent conductors. Red characters denote the ratio of carrier concentration (n) and effective mass of electrons (m^*).

2.3 Correlated Metals for Transparent Conductor Applications

It was first proposed by Zhang *et al*²⁸ that correlated metals can be utilized as transparent conductors. The mechanism lies under the fact that the effective mass of electron is enhanced by electron correlation. As already mentioned in **Chapter 2.1**, the strength of electron correlation can be defined as:

$$m^* = m_{\text{band}}^*/Z_k \quad (2.13)$$

Where m^* is enhanced effective mass by electron correlation, Z_k is renormalization factor that represents correlation strength, and m_{band}^* is effective mass with no correlation. Now, recall the

discussion on plasma frequency of metals in **Chapter 1.3.2**. The plasma frequency is given by the expression:

$$\omega_p = \sqrt{\frac{N_f e^2}{m^* \epsilon_0 \epsilon_r}} \quad (2.14)$$

Where N_f is number of carrier, so called carrier concentration, e is elementary charge, m^* is effective mass of electron, ϵ_0 is vacuum permittivity, and ϵ_r is relative permittivity. As shown in **Equation (2.14)**, plasma frequency depends on the effective mass of electron in the system. Now, from **Chapter 1.3.2**, recall that most of the metals possess plasma frequency in the UV regime. However, with the aid of electron correlation, which increases electron effective mass, the plasma frequency can be shifted below the visible regime, so that the system can obtain optical transparency in the visible regime.

Meanwhile, electron effective mass not only affects plasma frequency, but also changes electrical conductivity. The conductivity of metal is given by the following equation:

$$\sigma = \frac{e^2 \tau N_f}{m^*} \quad (2.15)$$

Where σ is electrical conductivity, and τ is scattering time of electron. As shown in **Equation (2.15)**, as electron effective mass increases, the conductivity decreases. Therefore, in order to utilize correlated metals as transparent conductor, one must understand that there exists a give-and-take caused by enhanced effective mass by electron correlation. However, numbers of correlated metals, as also shown in **Figure 2.1**, has similar or higher electrical conductivity than ITO, thus one can obtain high electrical conductivity with strong electron correlation.

2.3.1 Cost-Effectiveness of Transparent Correlated Metals

As discussed in **Chapter 2.2**, due to limited resource of indium, along with increasing demanding, the alternative transparent conductor has to meet the following criteria: “cost-

effectiveness” and “performance”. In order to see if correlated metals are indeed cost-effectiveness, both abundance of the elements that composes correlated metals and how well the elements are supplied, should be confirmed. There are two correlated metals that has been proved as excellent transparent conductors, SrVO_3 and CaVO_3 , and SrNbO_3 , which is proposed as an excellent transparent conductor through this thesis. By simply checking the abundance of each elements with **Figure 2.2 (a)**, it is obvious that the elements compose correlated metals are much more abundant than indium; Even the abundance of Nb, which shows the lowest abundance among the elements that compose such correlated metals, is about 1000 times abundant than indium.

Indium is a by-product of zinc and tin processing operations⁵⁵. There is no existing indium mine in the world. Therefore, in order to increase indium production, the zinc and tin production should also be increased. Because of such a fact, indium production is severely limited, and the price hits up to 1000 dollars/kg. Meanwhile, according to U.S Geological Survey⁵⁶, strontium is supplied in the form of celestite (SrSO_4), which is 77 dollars/ton. Vanadium is in general supplied in the form of vanadium pentoxide (V_2O_5), which is about 5 dollars/kg. Calcium, which is one of the most abundant elements in the world, can be extracted from calcite (CaCO_3), which is only 11 dollars/ton. Niobium exists in the form of ferroniobium (FeNb), which is 18 dollars/kg. Therefore, in terms of availability in supply and price, transparent correlated metals can be regarded as being much more cost-effective than ITO.

2.3.2 Performance of Transparent Correlated Metals

In order to see if transparent correlated metals are competitive in terms of performance, the key descriptors, which was discussed in **Chapter 2.2.5**, should be addressed. **Figure 2.5** shows electrical conductivity σ as function of plasma frequency ω_p of several doped semiconductors, metals and correlated metals. As shown in **Figure 2.5**, doped semiconductors

have ω_p far below the visible regime, but have low σ , compared to metals. Also, metals have high σ , but have ω_p in the UV regime that prevents optical transparency in the visible range. Correlated metals listed in **Figure 2.5**, however, possess both high σ ($> 10^4$ S/cm) and ω_p right below the red energy, so it meets the requirements for the key descriptors.

Correlated metals also get benefits from short EMFP, due to enhanced electron effective mass. As mentioned in **Chapter 2.2.1**, thin films that are composed of conventional metals suffer from degradation of conductivity due to long EMFP. However, most correlated metals have much shorter EMFP, in the range of several nanometers (5.6 nm for SrVO₃ and 3.9 nm for CaVO₃). The short EMFP enables thin films of correlated metals to possess high electrical conductivity with extremely thin film thickness, allowing a more aggressive thickness scaling without suffering from degradation of conductivity due to surface and interface scattering of electrons. Therefore, with correlated metals, one can take advantage of not only reduce deposition time for device manufacturing.

2.3.3 SrVO₃

SrVO₃ is the first the correlated metal that was proved to be a competing transparent conductor. As already mentioned in **Chapter 2.3**, it has several benefits from enhanced electron effective mass. **Figure 2.6 (a)** shows thickness dependence conductivity of several transparent conductors, along with the values of EMFP. As shown in **Figure 2.6 (a)**, conventional metals, such as Ag or Au, possess high electrical conductivity, but suffer from degradation of conductivity below the thickness of about 20 nm, due to long EMFP. The degradation of conductivity is possible to be more severe, as the thickness goes down below 10 nm, due to percolation threshold. However, SrVO₃, with much shorter EMFP compared to conventional metals, suffers less from the degradation, while maintaining higher conductivity compared to ITO.

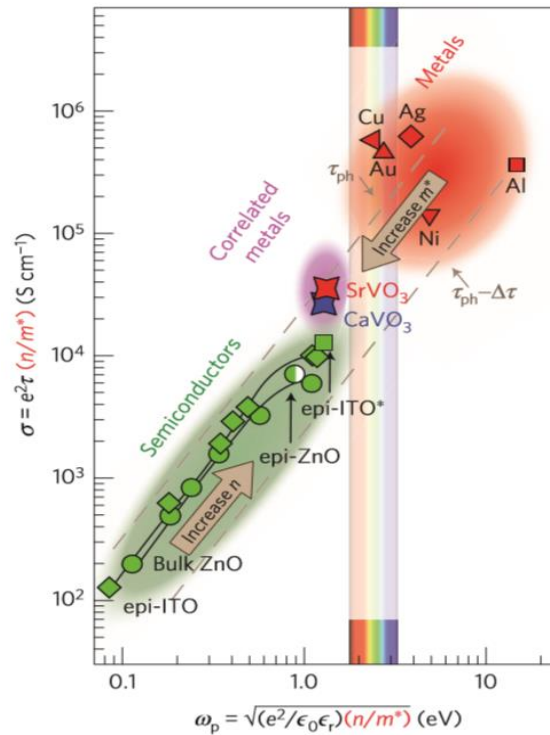


Figure 2.5 Electrical conductivity (σ) of several transparent conductors as a function of plasma frequency (ω_p)²⁸. Note that both quantities depend on carrier concentration (N_f) and electron effective mass (m^*).

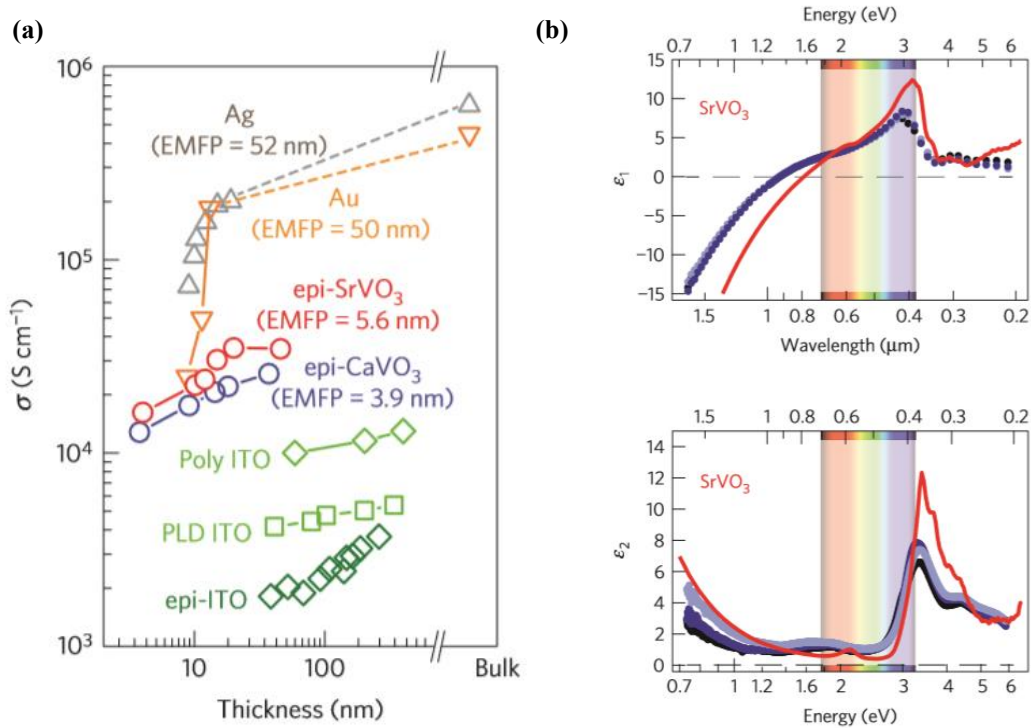


Figure 2.6 (a) thickness dependence of conductivity of several transparent conducting materials and **(b)** real and imaginary part of dielectric function spectra of SrVO₃ determined from density functional theory (red lines) and spectroscopic ellipsometry (purple dots)²⁸.

Figure 2.6 (b) shows complex dielectric function spectra ($\epsilon_1 + i\epsilon_2$) of SrVO₃,

determined from density functional theory (DFT) and spectroscopic ellipsometry. Since DFT calculation does not consider electron correlation effect, it can be compared to spectroscopic ellipsometry data in order to see the effect of enhanced m^* on the dielectric function spectra. As mentioned in **Chapter 1.3.2**, plasma frequency is where ϵ_1 hits zero. The plasma frequencies determined from DFT and spectroscopic ellipsometry are quite different, due to electron correlation effect. The ω_p determined from DFT is 1.58 eV, whereas ω_p determined from spectroscopic ellipsometry is 1.33 eV. As shown in **Figure 2.6 (b)**, the plasma frequency is shifted to lower energy, about 0.25 eV lower, due to the increase in m^* . Meanwhile, ϵ_2 spectra shows that SrVO₃ has only a small absorption peak on the visible range, marked by rainbow color, and a big absorption peak near 3.2 eV, which is outside the visible spectrum.

The renormalization factor Z_k for SrVO₃ is 0.33, determined from square of ratio of unscreened plasma frequency of experimental (determined from spectroscopic ellipsometry) to that of theory (DFT). Unscreened plasma frequency is the plasma frequency that can be determined without the effect of interband absorption. Note that, from **Chapter 1.3.6**, interband absorption can change plasma frequency, if applied to a ϵ_2 spectra of sole Drude model. Even though SrVO₃ has strong correlation ($Z_k = 0.33$) and heavy m^* , its conductivity is still higher than that of ITO, and it has optical transparency in the visible range, as determined from spectroscopic ellipsometry.

2.4 Strong Interband Absorption in SrVO₃ and SrNbO₃ as Transparent Conductor

Even though correlated metal SrVO₃ was verified as an excellent transparent conductor, there occurs a large interband absorption edge in the Blue energy (2.7 eV), as shown in **Figure 2.6 (b)**, causing significant loss in the average optical transparency in the visible regime. This absorption is mostly due to the electron transition from 2p orbital of oxygen to t_{2g} orbital of vanadium cation. In order to resolve this issue is a different selection of transition metal cation,

which occupies B site of Perovskite unit cell. The interband absorption can be shifted to the higher energy if the choice is made in the way that electronegativity difference ($\Delta\chi$) between transition metal cation and oxygen anion is larger. When considering this fact, one can simply choose transition metal cation from periodic table, with the fact that the electronegativity (χ) tends to decrease as one goes to the left or down in the table. Since oxygen anion has larger χ than any other transition metal cations, one can consider going down or left in the periodic table when making the choice. However, by switching transition metal cation, one should also consider that it can change the electron correlation strength, which can affect both electrical conductivity and plasma frequency that determines optical transparency. Therefore, the criteria become much more complicated in this sense.

SrNbO_3 , in bulk form, has a cubic Perovskite-type unit cell, with a lattice constant of 4.023 Å. **Figure 2.7** shows unit cell of SrNbO_3 . Like other Perovskite-type materials, SrNbO_3 has ABO_3 configuration, with A site occupied by Sr^{2+} cation, B site occupied by Nb^{4+} cation, surrounded by oxygen octahedra. It has been reported that SrNbO_3 is a correlated metal with metallic conductivity⁵⁷. Both SrVO_3 and SrNbO_3 are transition metal oxides (TMOs) that have partially filled d-orbital with one electrons per unit cell.

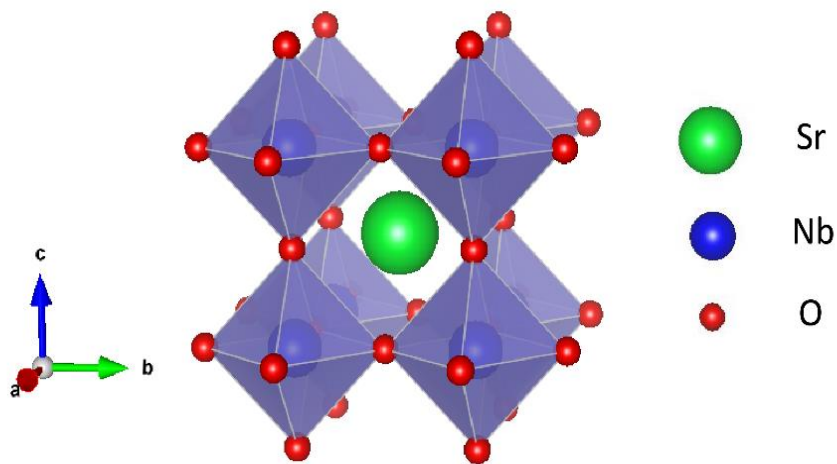


Figure 2.7 Unit cells of SrNbO₃. SrNbO₃ has Perovskite unit cell with A site occupancy of Sr cation, B site occupancy with Nb cation, which is surrounded by oxygen octahedra.

The major difference between SrVO₃ and SrNbO₃ comes from the difference between Vanadium cation (V⁴⁺) and Niobium cation (Nb⁴⁺). Both have partially filled d-orbital with one electron, but have different electron configuration, as that for V⁴⁺ is 3d₁, and that for Nb⁴⁺ is 4d₁. There are two major differences: electronegativity χ and electron correlation strength. In the periodic table, Niobium is located right below vanadium. Actually, the χ of vanadium is 1.63, whereas that of niobium is 1.6, so, it follows the rule of thumb that was mentioned above. Since Niobium has lower χ , considering electronic band structure, the energy gap between niobium and oxygen anion is larger. This causes interband absorption to occur at the higher energy, possibly pushing the absorption edge beyond the visible into UV regime. If the absorption edge is pushed to the higher energy, the system can obtain more optical transparency in the visible range.

The difference in transition metal cations can also alter the correlation strength. Note that, as mentioned earlier in this chapter, V⁴⁺ has electron configuration of 3d₁, whereas Nb⁴⁺ has that of 4d₁. This means that, even though both cations have one electron in the outer shell, larger d-orbital of Nb⁴⁺ will cause more overlaps between the d-orbitals of each unit cell. The more overlap in the d-orbital consequently make the bandwidth of t_{2g} orbital wider, and the wider t_{2g} bandwidth results in weaker electron correlation, as the curvature of the band ($\frac{\partial^2 E}{\partial k^2} = \frac{2\hbar}{m^*}$) increases. In principle, the weaker electron correlation in SrNbO₃ results in higher electrical conductivity, yet the shift of plasma frequency ω_p becomes smaller. If the shift is small so that it sits above the visible range, it will negatively affect the optical transparency. However, it is still possible that ω_p sits below the visible regime, since that of SrVO₃ is 1.33 eV, which is far below the red energy (~1.7 eV).

2.5 Theoretical and Experimental Results

2.5.1 Sample Growth and X-ray Diffraction

Six epitaxial SrNbO₃ thin films, with thicknesses of 10.6, 23.2, 29.2, 37, 40, and 60 nm, were grown on cubic [100] oriented KTaO₃ by Dr. Oka Daichi at Department of Chemistry at the University of Tokyo, by pulsed laser deposition (PLD) method. A sintered pellet of Sr₂Nb₂O₇ was used as a target and irradiated by KrF excimer laser, with the wavelength of 248 nm. before the growth, KTaO₃ substrate were heated at optimal temperature by using an infrared heating lamp. The film thicknesses were measured by using X-ray diffraction method. The films were tetragonally distorted, due to compressive strain caused by lattice mismatch between SrNbO₃ and KTaO₃ ($a = 3.989 \text{ \AA}$), with lattice mismatch of -0.85 %. Only 00 l diffraction peaks were observed, as shown in **Figure 2.8**, indicating (001) orientation of the film to the out of plane direction. An electrical pattern was attached to the surface of 37 nm SrNbO₃ thin film for electrical characterization.

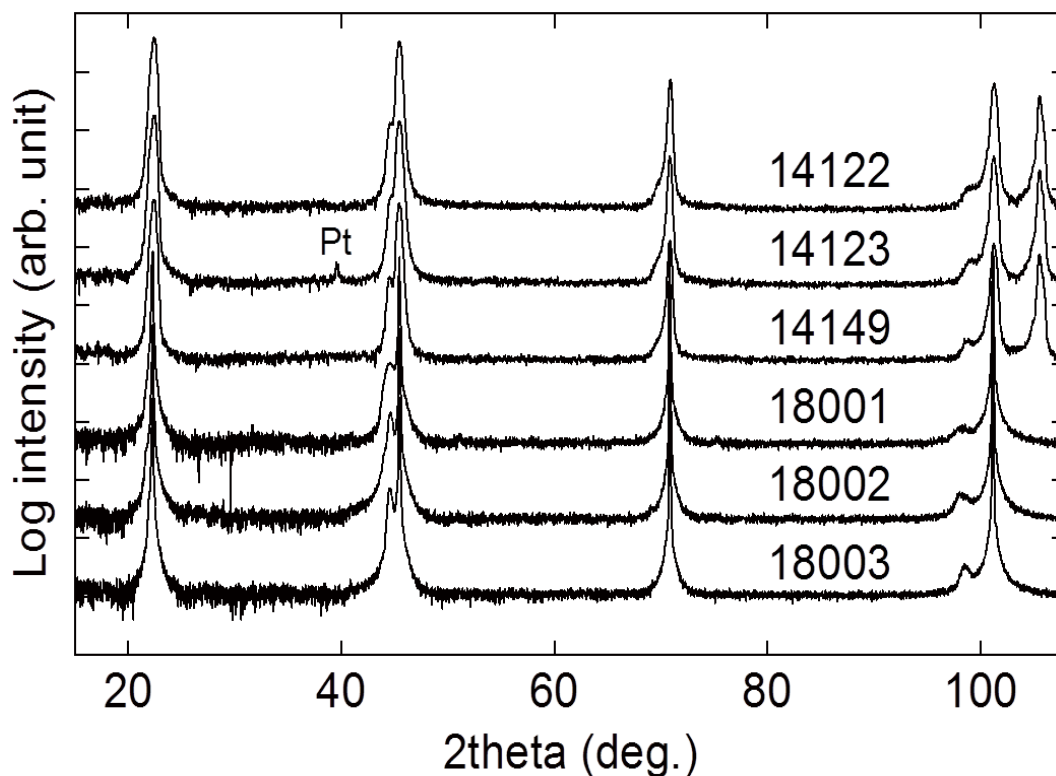


Figure 2.8 X-ray diffraction peaks for six SrNbO₃ thin films. The 5-digit numbers correspond to the thickness of 10.6 nm (18001), 23.2 nm (18003), 29.2 nm (18002), 37 nm (14149), 40 nm (14122) and 60 nm (14123).

2.5.2 Spectroscopic Ellipsometry for SrNbO₃ on KTaO₃

2.5.2.1 Experimental Procedure

Spectroscopic ellipsometry measurements were done on five SrNbO₃ thin films. The thin film with thickness of 37 nm has electrical pattern, so it was not possible to do ellipsometry measurements on the sample. Prior to any ellipsometry measurements, the backside of substrate for each sample was grinded with 30 μm alumina powder, in order to avoid complexity of reflection from the backside. Two types of ellipsometers were used for measurements: Infrared ellipsometry and UV-visible ellipsometry. For infrared range ellipsometry measurements, IR-VASE Mark II ellipsometer (J.A.Woollam Co.) was used, with the spectral range from 0.01 to 0.7 eV. IR ellipsometry measurements were performed by Dr. Alexej Pogrebnyakov. For UV-visible ellipsometry measurements, The variable angle spectroscopic ellipsometry (VASE) M-2000 ellipsometer (J.A.Woollam Co.) with the spectral range from 0.7 to 5.1 eV was used for measuring ellipsometric Ψ and Δ of the thin films. For modeling, Sellmeier, Drude, and Tauc-Lorentz models were used to minimize mean-square error (MSE) for the fitting. For surface roughness analysis, Bruggeman EMA method was used, assuming 50 % of air and 50 % of the medium.

2.5.2.2 Modeling Procedure

In order to model ellipsometry data for thin film samples, the ellipsometry data for substrate must be obtained first. KTaO₃ is an insulating material, with the bandgap of 4.9 eV. According to Jellison *et al*⁵⁸, the interband transition occurs at near 4.6 eV. So, it should be considered that the interband absorption occurs near that energy. This interband absorption can be fitted with either Tauc-Lorentz or Lorentz model.

The absorption peak may not be composed of single Lorentz model if the band has

some broadness. The absorption peak can be composed of more than two Lorentz oscillators. By placing an additional peak near 4.6 eV, adjusting fitting parameters (amplitude and broadness of the peaks), and applying Bruggeman effective medium approximation for surface roughness, I was able to get really nice fit, as shown in **Figure 2.9**. The fitting line, which is denoted as dotted line, well follows the ellipsometry raw data, Ψ and Δ . From this fitting, I was able to obtain optical constants of KTaO_3 substrate. Once this process is done, the optical modeling of SrNbO_3 can be done.

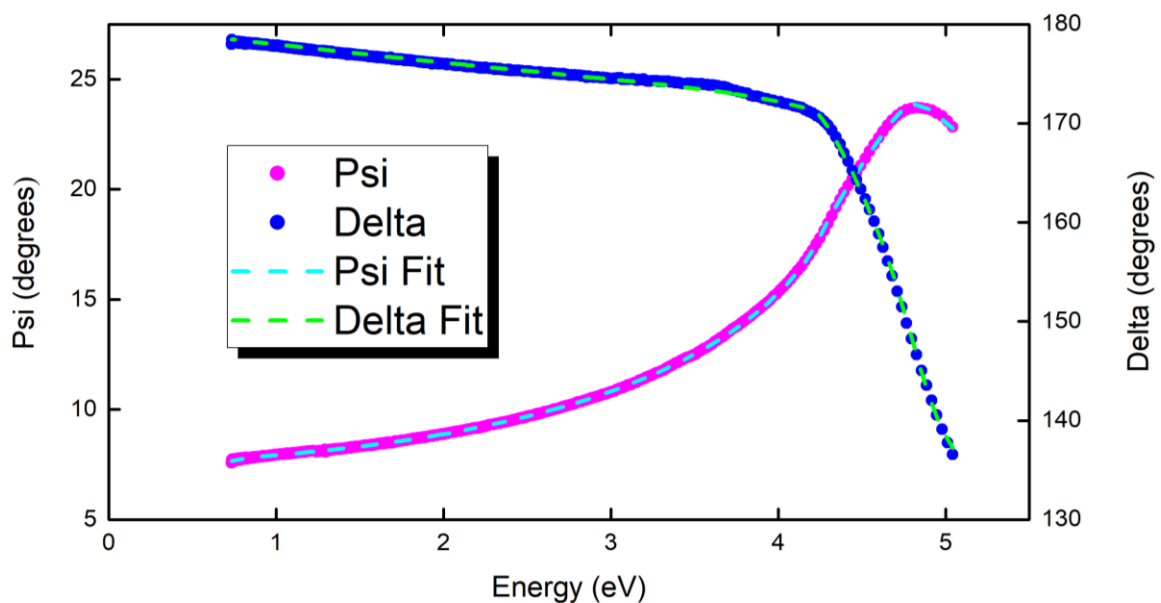


Figure 2.9 Spectroscopic ellipsometry data (Ψ and Δ) for KTaO_3 and fitting result. The data was fitted with two Lorentz oscillators.

Ψ and Δ for the thin film is more complicated, since it contains reflected light from surface of the thin film, as well as reflected light from the film/substrate interface. In order to fit Ψ and Δ for SrNbO_3 , proper layer optical modeling should be done first. I assumed that the substrate is composed of KTaO_3 with optical constant obtained from previous procedure and that the thickness is infinite, since the backside of the substrate was grinded, so that there is no reflection from it. When setting up the layer optical model for the SrNbO_3 thin film, I utilized the film thickness that was determined from X-ray diffraction data. For optical modeling,

assuming that SrNbO_3 is a metal, I decided to use Drude-Lorentz model, which describes optical properties of metals. For interband absorption, I utilized information on interband transition, provided by Sun *et al*⁵⁹. According to the paper, the interband absorption occurs at 2.7, 3.3 and 5.1 eV. By applying Drude model for free-carrier absorption in IR range and applying Lorentz and Tauc-Lorentz oscillators for interband transitions, I was able to get the fitting results, as shown in **Figure 2.10**. The fitting does not look okay. Therefore, the refinement of the fitting is needed.

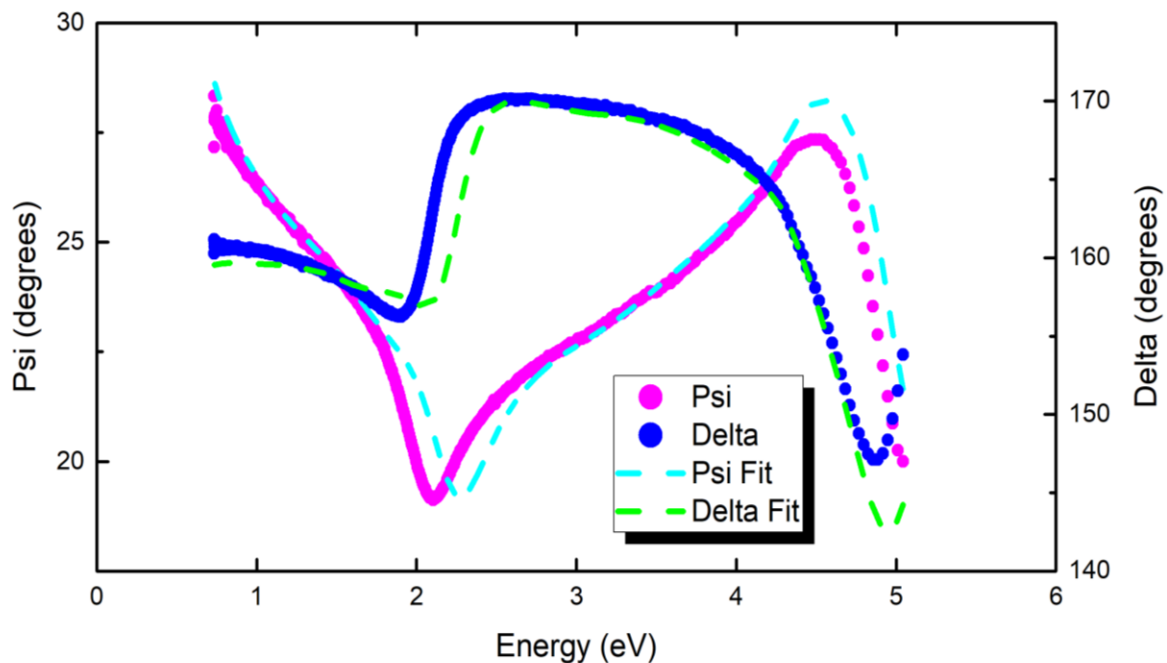


Figure 2.10 Ellipsometry fitting result after properly setting up oscillators and layer optical model for substrate and thin film.

In order to get the better fitting, I tried to adjust fitting parameters. For Drude model, I adjusted two fitting parameters, resistivity and electron scattering time. For Lorentz model, I tried to adjust amplitude, broadness, and central energy (position) of the peaks. For Tauc-Lorentz model, I also tried to adjust an additional fitting parameter, Tauc-gap. I also assumed that each interband absorption peak is not only composed of single oscillator, so I added Lorentz models near each absorption energy. I also applied Bruggeman effective medium

approximation for characterizing surface roughness. Finally, I got the fitting, as shown in **Figure 2.11**. The mean-square error was only about 1.4. After getting a good fit, I evaluated the fitting. All the oscillators were within the spectral range, and all the fitting parameters physically made sense (no negative amplitude values, Drude resistivity on the level of 10^{-4} - 10^{-5} Ohms.cm, thickness value, surface roughness value). Especially, the thickness value should not be largely different from that determined from X-ray diffraction, and surface roughness should not be too large (> 2 nm).

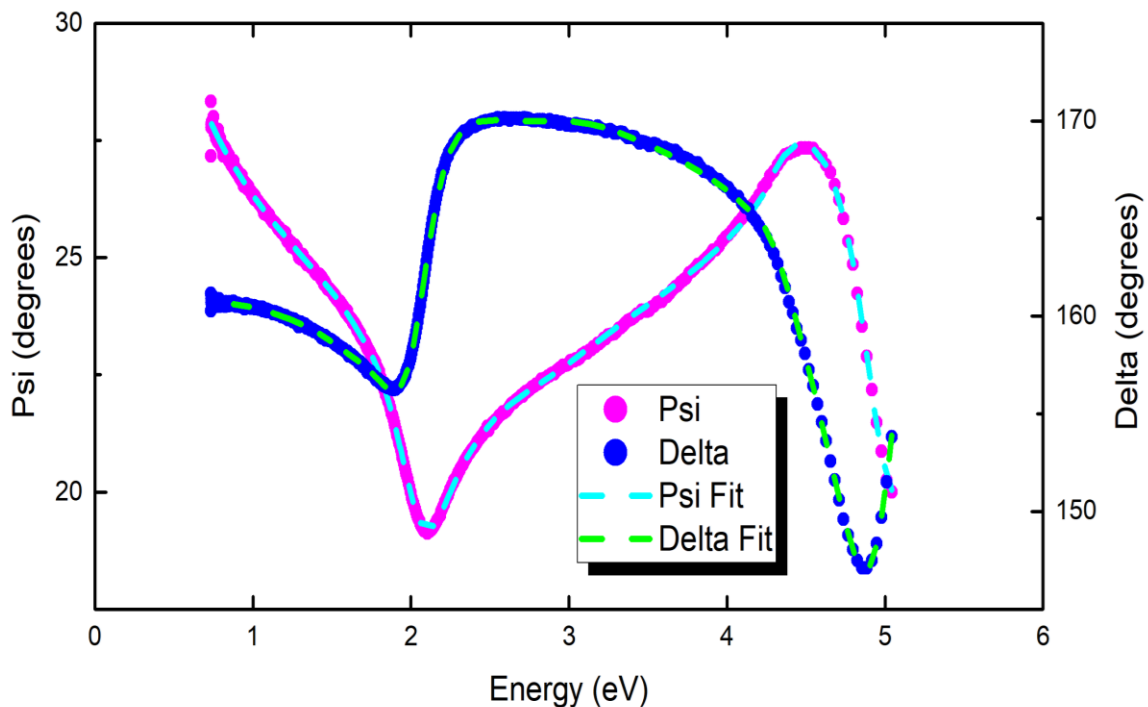


Figure 2.11 Ellipsometry fitting results after the refinement. The refinement includes adjustment of the fitting parameters, and consideration of surface roughness.

2.5.2.3 Results

Figure 2.12 shows dielectric function spectra ($\epsilon_1 + i\epsilon_2$) for five SrNbO₃ thin films, determined from spectroscopic ellipsometry, along with the dielectric function determined from DFT calculation. The spectra were separated into two parts for lower energy (infrared,

from 0.05 to 1.5 eV) and higher energy (near infrared + visible + UV, from 1.5 to 5.1 eV). The dielectric function spectra in the lower energy regime follows Drude model (free carrier absorption, increasing of ϵ_2 in infrared regime), demonstrating metallic property of SrNbO₃. In the higher energy regime, experimental ϵ_2 spectra (lower left of **Figure 2.12**) shows no absorption peak in the visible range, and absorption edge is presented near 5.1 eV, which is a deep UV range.

The DFT dielectric function spectra was intentionally plotted together with experimental results in order to show the effect of electron correlation on the screened plasma frequency ω_p . Note that average ω_p SrNbO₃ thin films determined from spectroscopic ellipsometry results is 1.97 eV, whereas ω_p determined from DFT is 2.21 eV. Note that the ratio of experimental ω_p to theoretical ω_p of SrNbO₃ is smaller than that of SrVO₃, due to weak electron correlation. The shifting of ω_p by amount of -0.24 eV is due to enhanced electron effective mass. From this fact, it is shown that SrNbO₃ is benefitted from electron correlation, in that ω_p is shifted from the middle to the edge of visible range, obtaining more optical transparency in the visible range. Even though the ω_p sits slight above red energy (1.77 eV), ϵ_2 spectra shows no absorption from the visible range to the deep UV range. Therefore, with spectroscopic ellipsometry results, it is demonstrated that SrNbO₃ has optical transparency from visible to deep UV.

There are some significant discrepancies in dielectric function spectra between experiment and theory. Note that, from the ϵ_2 spectra of lower energy, DFT has larger free carrier absorption (more rapid increasing in ϵ_2 as heading to lower energy). Also, in the higher energy, DFT ϵ_2 spectra shows several absorption peaks near 2.6 eV, 3.1 eV, and 3.9 eV, whereas experimental results show no absorption peaks. The reason for the difference is not so clear, but it could be that DFT often overestimates both free carrier absorption and interband absorption²⁸.

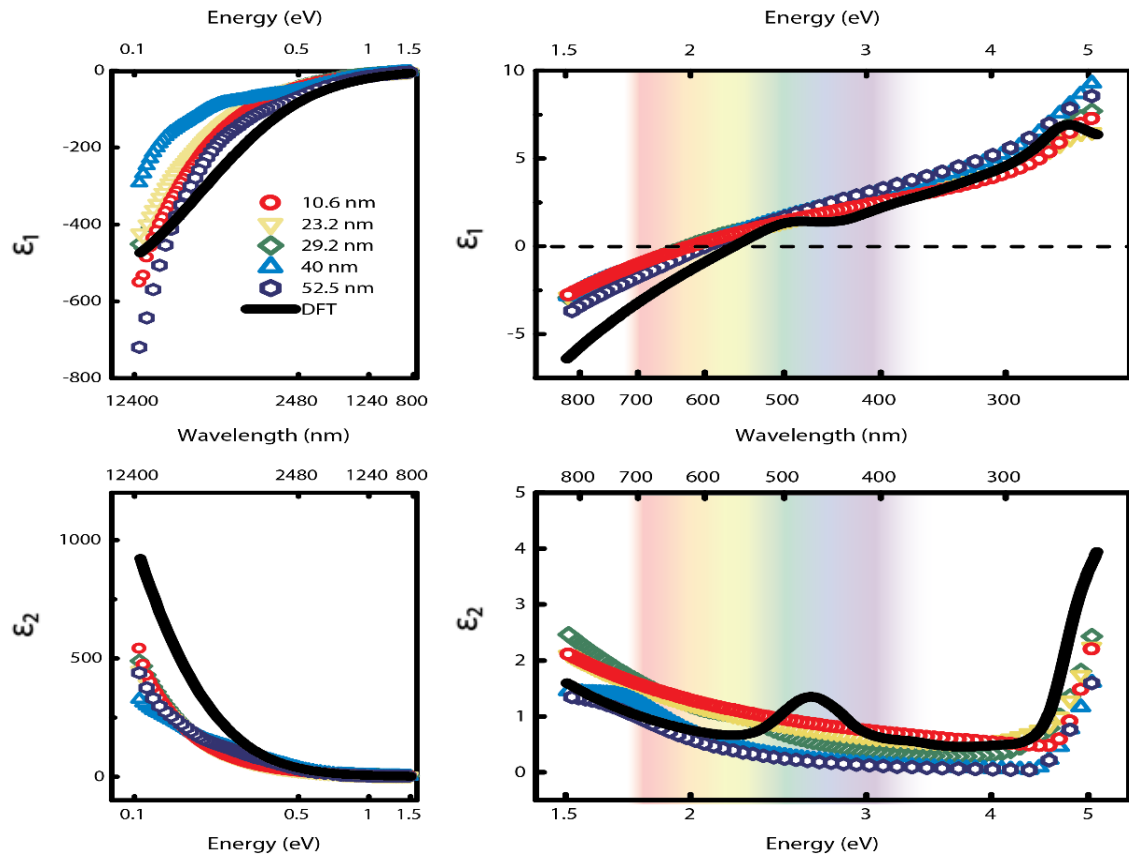


Figure 2.12 Dielectric function spectra of five SrNbO₃ samples with different thicknesses determined from spectroscopic ellipsometry, along with DFT calculation. The spectral range is from 0.1 eV to 5.1 eV. Rainbow in the background denotes the visible range.

2.5.3 Spectroscopic Ellipsometry for SrNbO₃ on LSAT

Spectroscopic ellipsometry measurements were also performed on four SrNbO₃ thin films grown on (LaAlO₃)_{0.3}(Sr₂AlTaO₆)_{0.7} (LSAT) substrate. These four films were grown by Joseph Roth, a graduate student at Dr. Engel-Herbert's lab, with sputtering method. Ellipsometry measurements were done with M-2000 variable angle spectroscopic ellipsometry, with the spectral range from 0.7 to 5.1 eV. For analysis of spectroscopic ellipsometry data for these films, the optical constants of LSAT was first investigated by modeling optical constants with Lorentz and Tauc-Lorentz oscillators. **Figure 2.13** shows optical dielectric function spectra of four different SrNbO₃ thin film samples with different thicknesses, along with DFT calculation results.

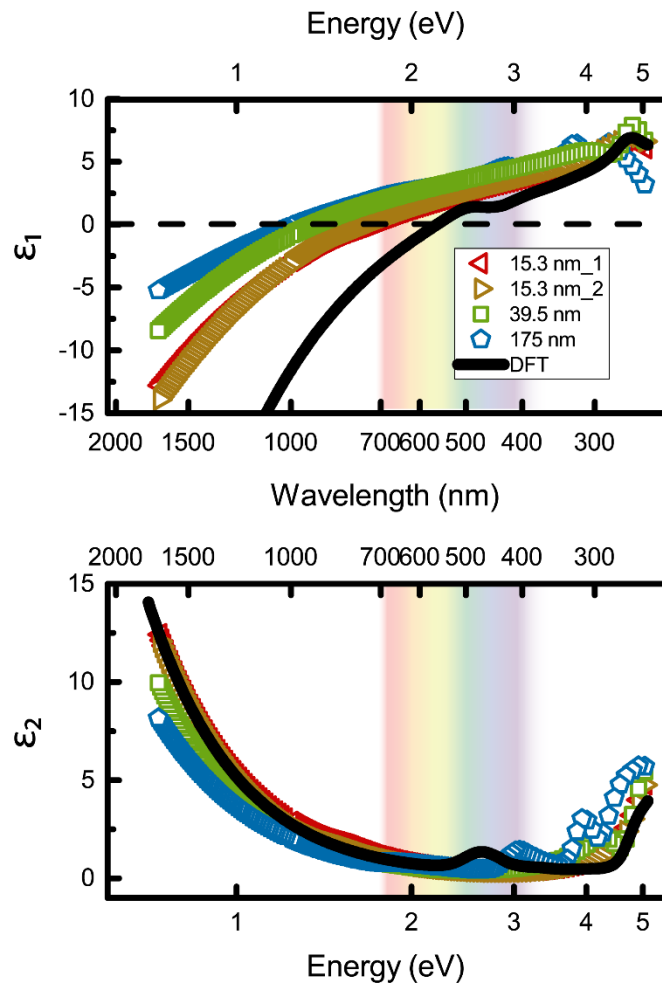


Figure 2.13 Optical dielectric function of four sputtered SrNbO₃ thin films determined from spectroscopic ellipsometry, along with DFT calculation. The spectral range is from 0.7 eV to 5.1 eV.

The sputtered thin films show huge variation of plasma energy values, varying from 1.4 eV to 1.7 eV. This can be partially due to different resistivity values, which is originated from different growth conditions. **Table 2.1** shows the values of resistivity and growth conditions for four different sputtered thin films. As discussed in **Chapter 2.2.5**, conductivity and plasma energy depends on the ratio of carrier concentration to the electron effective mass. When comparing films on LSAT and those on KTaO₃, the formers have higher resistivity thus lower conductivity. When ignoring the effect of scattering time (assume the value is similar in both cases), the ratio is lower for the films on LSAT. If the ratio is lower, the plasma energy should also be lower, according to **Chapter 2.2.5**

Thickness (nm)	15.3 nm_1	15.3 nm_2	39.5 nm	175 nm
Resistivity (Ω .cm)	2.92×10^{-4}	3.72×10^{-4}	1.23×10^{-3}	1.21×10^{-3}
Deposition time (mins)	30	30	30	120
RF power (W)	12	12	12	20
Pressure (mT)	10	6	10	16
Substrate temperature ($^{\circ}$ C)	700	700	800	800

Table 2.1 Resistivity and growth conditions of four different SrNbO₃ thin films grown by sputtering technique. Numbering (#) denotes two different thin films with the same film thickness. In courtesy of Joseph Roth.

Also, the sputtered thin films have stronger absorption peak at 5.1 eV, compared to SrNbO₃ grown on KTaO₃. The reason that it happens can be due to different strain states that come from different kinds of substrate (lattice mismatch with LSAT = -4 %). Because Sample with the different strain state have different band structure and DOS, it is possible that optical dielectric functions can be different for the samples on KTaO₃ and LSAT.

2.5.4 DFT and DMFT Calculation

DFT and DMFT calculations were conducted by Dr. Turan Birol at Department of Materials Science and Engineering of University of Minnesota, in order to see the potential of SrNbO₃ as a transparent conductor. **Figure 2.14** shows calculated band structures of DFT with the correction of DMFT of SrVO₃ and SrNbO₃, in the vicinity of Fermi level, denoted as 0 eV. From the both band structure, we can simply figure out that SrNbO₃ is metallic, since the Nb-t_{2g} band is across the Fermi level. The t_{2g} bands are partially occupied (one electron in three

bands) and are responsible for metallic conductivity of SrNbO₃. Also, the bandgap between oxygen 2p bands and Nb-t_{2g} band is wider in the case of SrNbO₃, so it is possible that interband absorption, which potentially degrades optical transparency, occur in the higher energy. Also, the t_{2g} bandwidth of SrNbO₃ is wider than that of SrVO₃, showing weaker electron correlation in SrNbO₃. The renormalization factor Z_k for SrNbO₃ was determined from the slope of self-energy of the t_{2g} orbitals calculated from both DFT and DMFT. Z_k for SrNbO₃ was founded to be 0.72, which represents much weaker electron correlation than that of SrVO₃, which has Z_k of 0.33.

As shown in **Figure 2.14**, the bandwidth of the t_{2g} bands determined from DMFT is narrower than that determined from DFT. This is due to the fact that DFT does not consider the effect of electron correlation, whereas DMFT does. With the effect of electron correlation, the electron effective mass increases and causes narrower bandwidth. The narrower bandwidth represents lower electrical conductivity, as the slope of band structure is the group velocity of the electrons. This agrees with the fact that electron correlation decreases conductivity, due to enhanced electron effective mass.

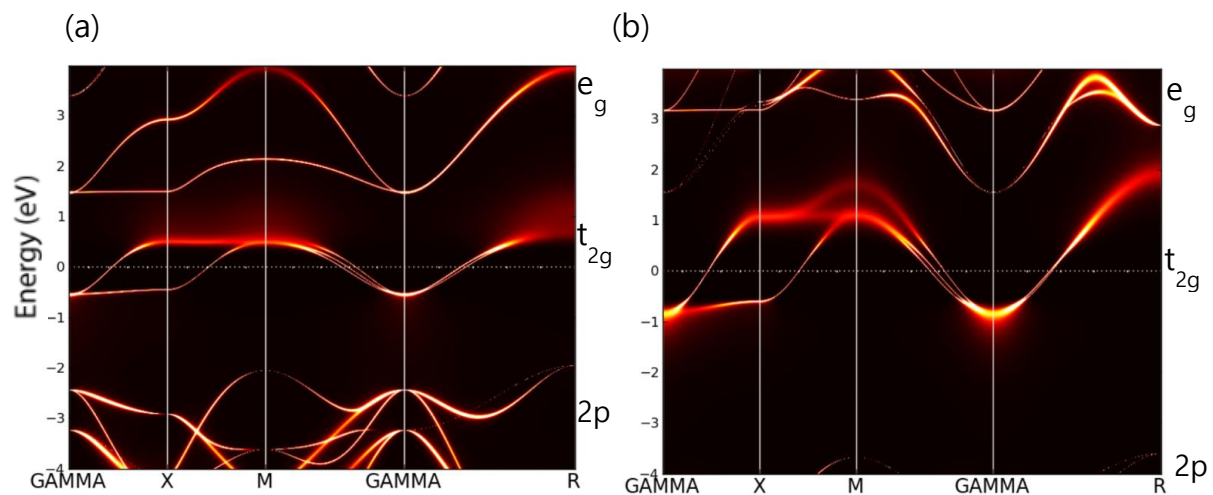


Figure 2.14 Band structure of (a) SrVO₃ and (b) SrNbO₃ determined from DFT with DMFT correction. Fermi level is denoted as white line (DMFT) at 0 eV. For DFT band structure, Nb-e_g bands, Nb-t_{2g} bands, and oxygen 2p bands are presented. In Courtesy of Dr. Turan Birol.

The band structure can be related to the interband absorption presented in ϵ_2 spectra in **Figure 2.12**. As we see the ϵ_2 spectra determined from DFT, we have small peaks at 2.6, 3.1, 3.9 eV and a large peak at 5.1 eV. The peaks at 2.6, 3.1 and 3.9 eV are mostly due to the interband transition occurring between Nb-eg band and Nb-t2g bands, since the gap is very large between Nb-t2g bands and Oxygen 2p bands. The large peak at 5.1 eV is mostly due to the interband transition occurring between Oxygen 2p bands and Nb-t2g bands, since there exists no such gap between Nb-eg band and Nb-t2g bands that exceeds 4 eV.

2.5.5 Hall Coefficient Measurement

The Hall coefficient measurements were conducted by Joseph Roth, a graduate student at Dr. Roman Engel-Herbert's lab, using Van der Pauw setup. The Van der Pauw setup was first designed by Van der Pauw, in order to extract resistivity (ρ), carrier concentration (n), and carrier mobility (μ) of conducting materials by utilizing Hall effect⁶⁰. Briefly speaking, Hall effect is the creation of voltage difference (Hall Voltage) due to carriers' movement under magnetic field that exert transverse force on the carriers. By measuring Hall Voltage, one can determine n and μ , and from these values, one can also determine ρ . Hall coefficient measurements were done on five SrNbO₃ thin films, with the thicknesses of 10.6, 23.2, 29.2, 37 and 40 nm. For 60 nm film, only the sheet resistance was measured. The film thickness dependent sheet resistance (R_s) is shown in **Figure 2.15 (a)**. The line fitting shows Fuchs-Sondheimer (FS) effect for electron surface scattering effect and Mayadas-Shatzkes (MS) effect for grain boundary scattering, which was already discussed in **Chapter 2.2.4**. The FS/MS fitting is in a good agreement with experimental data. All the sheet resistance data show metallic behavior of SrNbO₃. For 10.6 nm and 60 nm thick SrNbO₃ thin films, sheet resistance of 67.5 Ω /sq. and 15.3 Ω /sq were determined, respectively. These values show that our SrNbO₃ thin films have significantly lower sheet resistance than other TCOs^{46,61}. The fact that

experimental sheet resistance for 40 nm and 60 nm thin films are slightly off from the fitting line can be due to different laser source in PLD system. Figure 2 (b) shows thickness dependence of mobility (μ). The average value of $7.91 \text{ cm}^2 \text{ V}^{-1} \text{ s}^{-1}$ was determined. This mobility value is slightly higher than those of other correlated metal transparent conductors, such as SrVO_3 and CaVO_3 ²⁸, and about one magnitude lower than conventional TCOs^{42,46,61}. The lower values of μ compared to those of conventional TCOs result from electron correlation effect, which increases m^* . The thickness dependence of carrier concentration (n) is shown in Figure 2 (c). The n values are on par with other correlated metals, and about one order of magnitude higher than conventional TCO. From comprehensive electrical data above, it is noticed that lower μ is compensated by high n , and consequently, the compensation results in competing R_s among other transparent conductors.

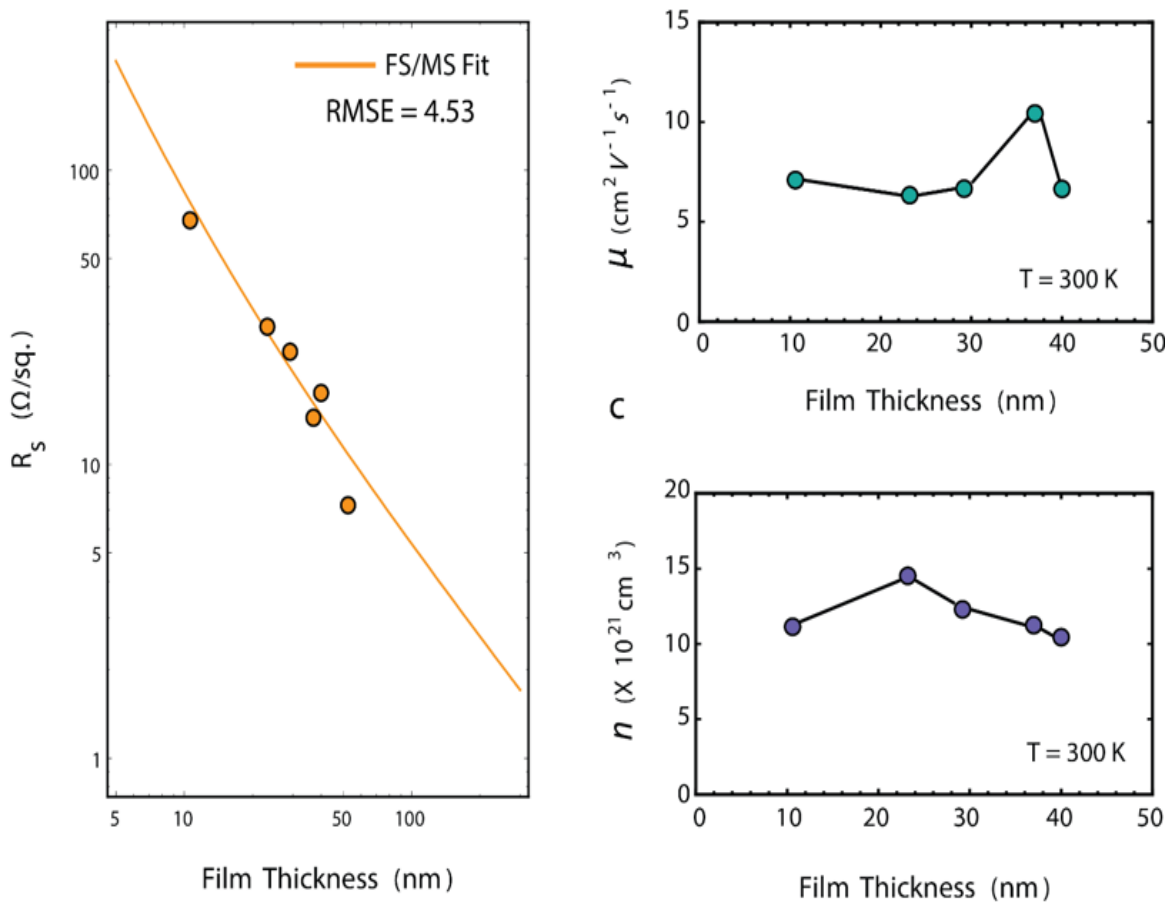


Figure 2.15 (a) Sheet resistance, **(b)** mobility, and **(c)** carrier concentration as function of film thickness at the room temperature. The line fit in Figure 2.8 (a) shows Fuch and Sondheimer (FS) and Mayadas and Shatzkes (MS) model. The experimental error bars are smaller than the legends.

One of the advantages of utilizing correlated metals for transparent conductor is small EMFP, $\Lambda = \hbar(3\pi^2)^{1/3}(\tau n^{2/3})(n/m^*)$, which allows growth of ones of nanometer-scale thin film with less suffering from surface and grain boundary scattering of electrons. For SrNbO₃, the average EMFP of 3.5 nm was determined based on experimentally determined n and μ . This value of EMFP is comparable to those of SrVO₃ ($\Lambda = 5.6$ nm) and CaVO₃ ($\Lambda = 3.9$ nm), and much lower than those of conventional metals, such as silver ($\Lambda = 52$ nm)³². Due to small EMFP, the thickness dependence resistivity is smaller in SrNbO₃, allowing more aggressive thickness scaling for more transparency with less loss in conductivity.

2.5.6 Figure of Merit for SrNbO₃

The performance of transparent conductor is determined by Figure of Merit, $\Phi_{TC} = T^{10}/R_s$, with T optical transmittance and R_s sheet resistance, proposed by Haacke⁵⁰, as mentioned in **Chapter 2.2.4**. **Figure 2.16** shows thickness dependence of Φ_{TC} of conventional transparent conductors and SrNbO₃ in the visible range (400 – 800 nm), UV A (315 – 400 nm), UV B (280 – 315 nm) and germicidal UV range (250 – 280 nm). In general, UV light is divided into 3 parts: UV A, UV B and UV C. UV A is the wavelength range from 315 to 400 nm, UV B is from 280 to 315 nm and UV C is from 200 to 280 nm. The applications for UV light in each part are totally different. Especially, Germicidal UV range belongs to UV C range, and it usually ranges from 250 – 280 nm. The name “germicidal” comes from the fact that UV light in this specific range kills or inactive bacteria, germs, and virus. Germicidal UV range was specifically chosen to demonstrate Φ_{TC} of each material in the deep UV range. The thickness-dependent effects on transmission and sheet resistance, such as reflection at the film interfaces and surface scattering and grain boundary scattering of electron (FS/MS model),

were considered for the calculation. Note that, in **Figure 2.16**, like other correlated metal transparent conductors, maximum Φ_{TC} of SrNbO₃ is located in much thinner film thickness compared to ITO, a tremendous benefit in device industry (reduced deposition time with high output performance). **Figure 2.16 (a)** shows that conventional transparent conductors are outperformed by the maximum Φ_{TC} of SrNbO₃ at 10.6 nm, indicating SrNbO₃ as outstanding transparent conductor in visible range. In UV A range, as shown in **Figure 2.16 (b)**, however, silver starts to outperform any other transparent conducting materials. This is due to the fact that silver is the most conducting material in earth and has low absorption coefficients in this specific UV range. Nevertheless, the maximum Φ_{TC} of SrNbO₃ is higher than that of any conventional transparent conductors in UV B range and Germicidal UV range, as indicated in Figure 2.10 (c) and (d).

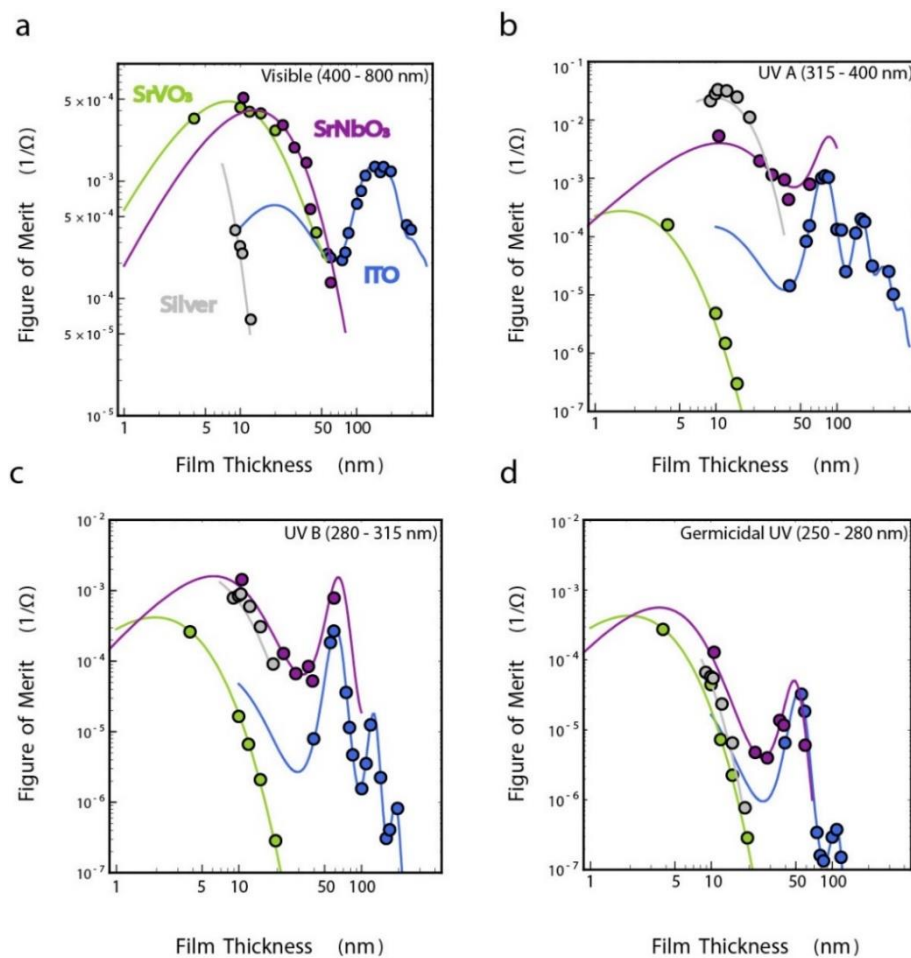


Figure 2.16 Figure of Merit as function of film thickness for conventional transparent conductors at (a) visible range (400-

800 nm), (b) UV A range (315 – 400 nm), (c) UV B range (280 – 315 nm), and (d) Germicidal UV range (250 – 280 nm). Experimental data points were extracted for silver^{32,62} (grey circles), ITO^{42,63}(blue circles), SrVO₃²⁸(yellow green circles) and SrNbO₃ from this work. Line fits are from Φ_{TC} calculation, discussed in **Chapter 2.2.4**.

2.6 SrNbO₃ as a Deep Ultraviolet Transparent Conductor

In the previous chapter, it was confirmed that SrNbO₃ has an excellent performance in both visible range and a deep UV range, especially in germicidal UV range. Specifically, the UV wavelength of 250 – 280 nm can be used as UV germicidal irradiation (UVGI), a method of using short UV rays to kill or inactive microorganisms, such as bacteria or virus. Because of such property, it is used in a variety of applications, such as water disinfection, air purifier and medical sterilization⁶⁴⁻⁶⁷. The current choice of light source for UVGI is low pressure mercury lamp, which can cause health and environmental risks. Under these circumstances, deep UV light emitting diodes (LEDs) can be outstanding light source for UVGI with non-biohazard and much higher efficiency^{64,68}. However, deep UV LEDs for typically wavelength below 300 nm have not been thoroughly developed and commercially very scarce⁶⁹. In order to resolve such issues, transparent electrode that has transparency in such deep UV range is in a significant need. Current choice for deep UV transparent conductor Sn doped β -Ga₂O₃, with the highest reported conductivity of $7.4 \times 10^{-4} \text{ S cm}^{-1}$, which corresponds to resistivity of $1.35 \times 10^{-3} \Omega \text{ cm}$, about two orders lower than that of SrNbO₃⁴⁸. Furthermore, optical transparency of β -Ga₂O₃ is very limited below 300 nm, hindering application of β -Ga₂O₃ to germicidal deep UV LED⁴⁹. With high electrical conductivity and transparency in those deep UV region, SrNbO₃ can effectively substitute the current choice of UV transparent conductors and boost commercial availability of deep UV LED.

Chapter 3 Spectroscopic Ellipsometry Results on Other Correlated Metals

In this chapter, spectroscopic ellipsometry results on other correlated metals, such as iron pnictide (10 % Co doped BaFe_2As_2) and 2-dimensional transition metal dichalcogenides (TMDs), will be briefly discussed. Even though they cannot be utilized as transparent conductors, due to large absorption in visible range, they helped me understand and build knowledge on spectroscopic ellipsometry.

3.1 Co Doped BaFe_2As_2

Cobalt doped BaFe_2As_2 is an iron pnictide superconductor with the space group of tetragonal $I4/mmm$. Its parental material, BaFe_2As_2 , is a bad metal. A “bad metal” refers to the material that has similar conductance behavior to the metal (band structure), but the conductivity is low compared to conventional metals due to electron correlation⁷⁰. By doping BaFe_2As_2 with Co, superconductivity phenomenon emerges and conductivity becomes higher^{70,71}. 10% Co doped BaFe_2As_2 was grown by Dr. Jie Xing at Department of Physics at University of Los Angeles, using flux method. The sample was easily cleaved with razor blade, so the surface was not needed to be polished for reflecting surface. The sample was measured with the incidence angle of 50° , 60° and 70° with spectral range from 0.7 to 5.1 eV. For modeling ellipsometry raw data, Drude and Lorentz models were used. For surface roughness characterization, Bruggeman EMA was used, assuming that roughness is composed of 50 % of air and 50 % of the material. **Figure 3.1 (a) and (b)** shows refractive index (n) and extinction coefficient (k) determined from spectroscopic ellipsometry. As it can be noticed from extinction coefficient (k) spectra, which is directly related to absorption coefficient α , the absorption is too high, as the value of it ranges from 1 to 2.5 in the visible range. Typical transparent conductors have extinction coefficients smaller than 0.5. Therefore, even though Co doped BaFe_2As_2 possesses high electrical conductivity.

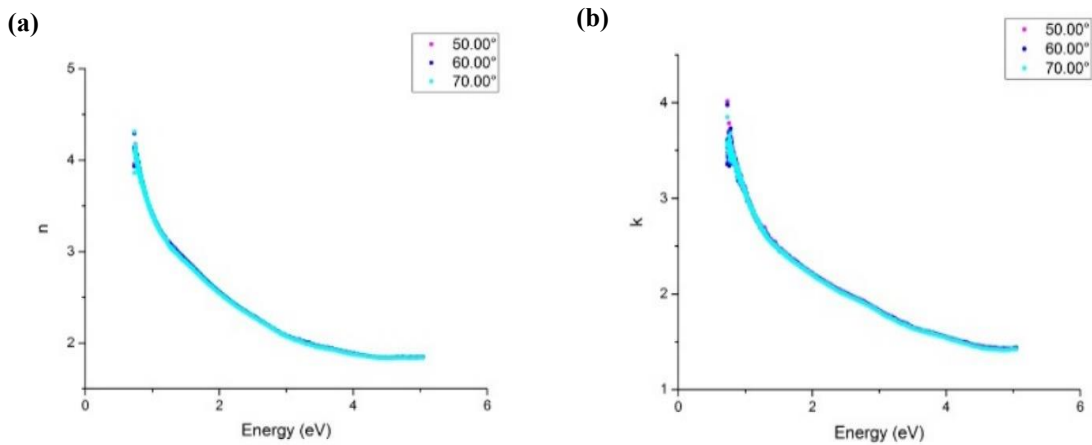


Figure 3.1 (a) Refractive index (n) and (b) extinction coefficients (k) of 10% Co doped BaFe_2As_2 determined from spectroscopic ellipsometry, with incident angle of 50° , 60° and 70° .

3.2 1-T TiS_2

1-T TiS_2 is 2D conducting transition metal dichalcogenides (TMDs). TMDs are materials with chemical formula MX_2 , where M denotes transition metals and X denotes chalcogens (S, Se, Te), which are also called “oxygen family”. 1-T denotes the unit cell is described by 1 layer of trigonal cells.

Single crystal of 1-T TiS_2 was grown by Dr. Jie Xing, using chemical vapor deposition (CVD) method. The crystal could also be easily cleaved, so no polishing was done on the surface of the sample. The measurements were done with 3 incident angles, 50° , 60° and 70° . For the ellipsometry data fitting, only Tauc-Lorentz and Lorentz models were used, since Drude behavior was not presented in the ellipsometry spectrum. For surface roughness characterization, Bruggeman EMA model was also used, assuming that the roughness layer is composed of 50 % of air and 50% of the material. **Figure 3.2** shows refractive index (n) and extinction coefficient (k) determined from spectroscopic ellipsometry. Note that absorption is also very large in the visible range, since the extinction coefficient ranges from 1.5 to 3 in the visible range.

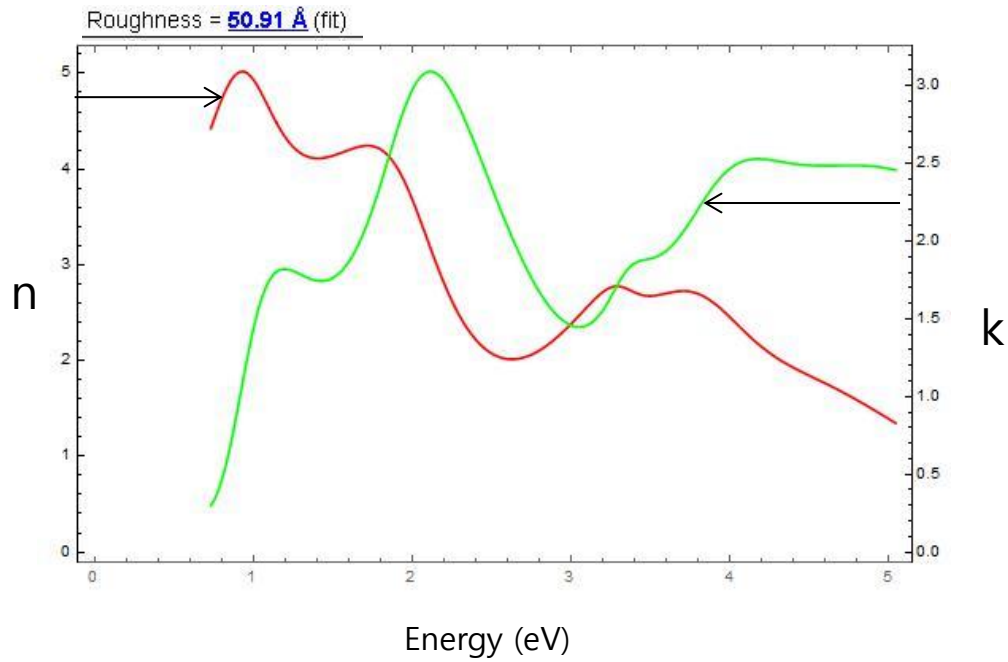


Figure 3.2 Refractive index (n , red) and extinction coefficients (k , green) of 1-T TiS₂ determined from spectroscopic ellipsometry. The Bruggeman EMA fitting gives the roughness thickness of about 5 nm.

3.3 2-H NbSe₂

2-H NbSe₂ is also a type of TMD that its unit cell is described by 2 layers of hexagonal cells (2-H). It is a superconducting material with critical temperature of 7 K. It has hexagonal unit cell, with the space group of $P6/mmc$. The sample was also easily cleaved, so reflecting surface could be obtained for ellipsometry measurement. The measurement and fitting method for ellipsometry of 2-H NbSe₂ is the same as those for 10% Co doped BaFe₂As₂, as described in **Chapter 3.1**. **Figure 3.3** shows dielectric function spectra of NbSe₂, determined from spectroscopic ellipsometry, in the spectral range from 0.7 to 5.1 eV. The plasma frequency determined from ϵ_1 spectra (where it crosses zero) is about 0.8 eV, which is far below the visible range. If we only consider the plasma frequency, NbSe₂ can potentially be a transparent conductor. However, as it can be noted from the imaginary dielectric function spectra (ϵ_2), there exist strong interband absorption near 2.5 eV, which could potentially harm optical transparency in the visible range.

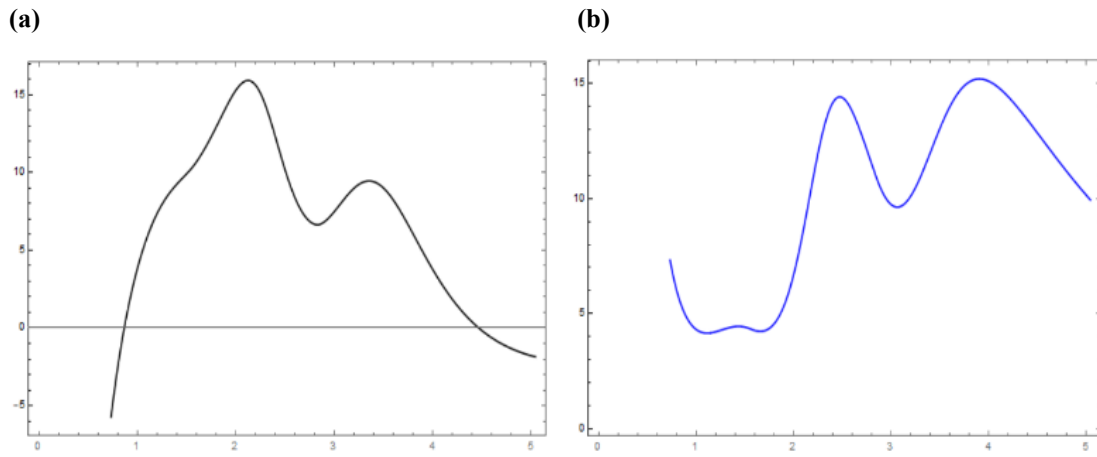


Figure 3.3 (a) real (ϵ_1) and (b) imaginary (ϵ_2) part of dielectric function spectra of NbSe₂, as a function of energy (eV). The line in the plot of ϵ_1 is parallel to 0 value in order to denote plasma frequency.

Chapter 4 Conclusion and Future Work

The spectroscopic ellipsometry is a very powerful tool for obtaining material's optical dielectric constants and corresponding Ellipsometer measures Ψ and Δ , which is amplitude ratio and phase difference of s- and p- polarized wave. The measured Ψ and Δ can be converted to pseudo-optical dielectric function $\langle \epsilon \rangle$, which can be fitted with general oscillator functions and surface roughness modeling. After raw ellipsometry data is fitted properly, one can obtain optical constants and corresponding optical properties of materials, such as transmission, reflection and absorption.

In this thesis, SrNbO₃ was proposed as both a visible transparent conductor and a deep-UV transparent conductor. The weaker electron correlation strength compared to SrVO₃ resulted in more transparency in visible range. DFT and DMFT calculations guided us to anticipate SrNbO₃ as a weakly correlated metal with absorption edge pushed to deep UV range. Spectroscopic ellipsometry and transport measurement confirmed the results of DFT and DMFT and demonstrated SrNbO₃ as a visible - deep UV transparent conductor with exceptional Φ_{TC} . Such a property of SrNbO₃ enables it to be utilized as transparent electrode in germicidal deep-UV LED for better performance and efficiency. The discovery of SrNbO₃ as a germicidal deep-UV transparent conductor is just the tip of an iceberg – Many more correlated metals, such as transition metal oxides, transition metal dichalcogenides, iron pnictides, and intermetallic compounds, await exploration of their rich optical and electrical properties

References

1. Fujiwara, H., *Spectroscopic ellipsometry : principles and applications*. (2007): John Wiley & Sons, Ltd. xviii, 369 pages.
2. Gopalan, V., *Gopalan Note Chapter 5 "Light at Interfaces: Reflection, Refraction and Transmission"*. (2017).
3. *Introduction to Polarization*. DOI: <https://www.edmundoptics.com/resources/application-notes/optics/introduction-to-polarization/>.
4. Co., J.A.W., *CompleteEase Software Manual*. (2014).
5. Gopalan, V., *Gopalan Note Chapter 3 "Light in Classical Lorentz Atom: Insulators"*. (2007).
6. Gopalan, V., *Gopalan Note Chapter 4 "Light in a Classical Lorentz Atom: II"*. (2007).
7. Gopalan, V., *Gopalan Note Chapter 6 "Light in Metals"*. (2008).
8. Palik, E.D. and G. Ghosh, *Handbook of Optical Constants of Solids Set: Handbook of Thermo-Optic Coefficients of Optical Materials with Applications*. (1997), San Diego: Academic Press Imprint Elsevier Science & Technology Books. 3224 p.
9. Jr., G.E.J. and F.A. Modine, *Parameterization of the optical functions of amorphous materials in the interband region*. Applied Physics Letters, (1996). **69**(3): p. 371-373.
10. Fujiwara, H. and M. Kondo, *Effects of carrier concentration on the dielectric function of ZnO:Ga and In₂O₃:Sn studied by spectroscopic ellipsometry: Analysis of free-carrier and band-edge absorption*. Physical Review B, (2005). **71**(7): p. 075109.
11. Kittel, C., *Introduction to solid state physics*. 8th ed. (2004): John Wiley & Sons. xix, 680 pages.
12. Fang, C.M., R.A. de Groot, and C. Haas, *Bulk and surface electronic structure of 1T-TiS₂ and 1T-TiSe₂*. Physical Review B, (1997). **56**(8): p. 4455-4463.
13. Niklasson, G.A., C.G. Granqvist, and O. Hunderi, *Effective medium models for the optical properties of inhomogeneous materials*. Applied Optics, (1981). **20**(1): p. 26-30.
14. Mott, N.F., *Metal-Insulator Transition*. Reviews of Modern Physics, (1968). **40**(4): p. 677-683.
15. Imada, M., A. Fujimori, and Y. Tokura, *Metal-insulator transitions*. Reviews of Modern Physics, (1998). **70**(4): p. 1039-1263.
16. Ramirez, A.P., *Colossal magnetoresistance*. Journal of Physics: Condensed Matter, (1997). **9**(39): p. 8171.
17. Tokura, Y. and Y. Tomioka, *Colossal magnetoresistive manganites*. Journal of Magnetism and Magnetic Materials, (1999). **200**(1): p. 1-23.
18. Basov, D.N. and T. Timusk, *Electrodynamics of high-T_c superconductors*. Reviews of Modern Physics, (2005). **77**(2): p. 721-779.
19. Urushibara, A., et al., *Insulator-metal transition and giant magnetoresistance in La_{1-x}Sr_xMnO₃*. Physical Review B, (1995). **51**(20): p. 14103-14109.
20. Kondo, S., et al., *LiV₂O₄: A Heavy Fermion Transition Metal Oxide*. Physical Review Letters, (1997). **78**(19): p. 3729-3732.
21. Tokura, Y. and N. Nagaosa, *Orbital Physics in Transition-Metal Oxides*. Science, (2000). **288**(5465): p. 462.
22. Lee, Y.S., et al., *Systematic trends in the electronic structure parameters of the 4d transition-metal oxides SrMO₃ (M = Zr, Mo, Ru and Rh)*. Physical Review B, (2003). **67**(11): p. 113101.
23. Skornyakov, S.L., et al., *Classification of the electronic correlation strength in the*

- iron pnictides: The case of the parent compound BaFe_2As_2 .* Physical Review B, (2009). **80**(9): p. 092501.
24. Qazilbash, M.M., et al., *Electronic correlations in the iron pnictides.* Nature Physics, (2009). **5**: p. 647.
 25. Dai, J., et al., *Iron pnictides as a new setting for quantum criticality.* Proceedings of the National Academy of Sciences, (2009). **106**(11): p. 4118.
 26. Castro Neto, A.H., *Charge Density Wave, Superconductivity, and Anomalous Metallic Behavior in 2D Transition Metal Dichalcogenides.* Physical Review Letters, (2001). **86**(19): p. 4382-4385.
 27. Ogawa, S., *Magnetic properties of 3d transition-metal dichalcogenides with the pyrite structure.* Journal of Applied Physics, (1979). **50**(B3): p. 2308-2311.
 28. Zhang, L., et al., *Correlated metals as transparent conductors.* Nature Materials, (2015). **15**: p. 204.
 29. Mizoguchi, H., et al., *A germanate transparent conductive oxide.* Nature Communications, (2011). **2**: p. 470.
 30. Hosono, H. and D.C. Paine, *Handbook of transparent conductors.* (2010): Springer Science & Business Media.
 31. Ghosh, D., et al., *Widely transparent electrodes based on ultrathin metals.* Optics letters, (2009). **34**(3): p. 325-327.
 32. O'Connor, B., et al., *Transparent and conductive electrodes based on unpatterned, thin metal films.* Applied Physics Letters, (2008). **93**(22): p. 433.
 33. Sondheimer, E.H., *The mean free path of electrons in metals.* Advances in physics, (1952). **1**(1): p. 1-42.
 34. Fukuda, K., S.H. Lim, and A. Anders, *Coalescence of magnetron-sputtered silver islands affected by transition metal seeding (Ni, Cr, Nb, Zr, Mo, W, Ta) and other parameters.* Thin Solid Films, (2008). **516**(14): p. 4546-4552.
 35. Hövel, M., B. Gompf, and M. Dressel, *Dielectric properties of ultrathin metal films around the percolation threshold.* Physical Review B, (2010). **81**(3): p. 035402.
 36. Heun, S., et al., *Conductance of Ag on Si (111): a two-dimensional percolation problem.* Journal of Physics: Condensed Matter, (1993). **5**(18): p. 2913.
 37. Yun, J., *Ultrathin metal films for transparent electrodes of flexible optoelectronic devices.* Advanced Functional Materials, (2017). **27**(18).
 38. Tokuno, T., et al., *Fabrication of silver nanowire transparent electrodes at room temperature.* Nano research, (2011). **4**(12): p. 1215-1222.
 39. Daniel, L., et al., *Flexible transparent conductive materials based on silver nanowire networks: a review.* Nanotechnology, (2013). **24**(45): p. 452001.
 40. Sannicolo, T., et al., *Metallic Nanowire-Based Transparent Electrodes for Next Generation Flexible Devices: a Review.* Small, (2016). **12**(44): p. 6052-6075.
 41. Zeng, X.Y., et al., *A new transparent conductor: silver nanowire film buried at the surface of a transparent polymer.* Advanced materials, (2010). **22**(40): p. 4484-4488.
 42. Ellmer, K., *Past achievements and future challenges in the development of optically transparent electrodes.* Nature Photonics, (2012). **6**(12): p. 809.
 43. Hu, L., D. Hecht, and G. Grüner, *Percolation in transparent and conducting carbon nanotube networks.* Nano letters, (2004). **4**(12): p. 2513-2517.
 44. De, S., et al., *Size effects and the problem with percolation in nanostructured transparent conductors.* Acs Nano, (2010). **4**(12): p. 7064-7072.
 45. Lee, J.H., et al., *Large-scale synthesis and characterization of very long silver nanowires via successive multistep growth.* Crystal growth & design, (2012). **12**(11): p. 5598-5605.
 46. Tadatsugu, M., *Transparent conducting oxide semiconductors for transparent*

- electrodes*. Semiconductor Science and Technology, (2005). **20**(4): p. S35.
47. Jin, S., et al., *Tuning the properties of transparent oxide conductors. Dopant ion size and electronic structure effects on CdO-based transparent conducting oxides. Ga-and In-doped CdO thin films grown by MOCVD*. Chemistry of Materials, (2007). **20**(1): p. 220-230.
 48. Garten, L.M., et al., *Structure property relationships in gallium oxide thin films grown by pulsed laser deposition*. MRS Communications, (2016). **6**(4): p. 348-353.
 49. Orita, M., et al., *Deep-ultraviolet transparent conductive β -Ga₂O₃ thin films*. Applied Physics Letters, (2000). **77**(25): p. 4166-4168.
 50. Haacke, G., *New figure of merit for transparent conductors*. Journal of Applied Physics, (1976). **47**(9): p. 4086-4089.
 51. Gordon, R.G., *Criteria for choosing transparent conductors*. MRS bulletin, (2000). **25**(8): p. 52-57.
 52. Fan, H.Y., *Infra-red Absorption in Semiconductors*. Reports on Progress in Physics, (1956). **19**(1): p. 107.
 53. Fuchs, K. *The conductivity of thin metallic films according to the electron theory of metals*. in *Mathematical Proceedings of the Cambridge Philosophical Society*. 1938. Cambridge University Press.
 54. Mayadas, A. and M. Shatzkes, *Electrical-resistivity model for polycrystalline films: the case of arbitrary reflection at external surfaces*. Physical review B, (1970). **1**(4): p. 1382.
 55. Alfantazi, A. and R. Moskalyk, *Processing of indium: a review*. Minerals Engineering, (2003). **16**(8): p. 687-694.
 56. Thomas D. Kelly, G.R.M., *Historical Statistics for Mineral and Material Commodities in the United States*, U.S.D.o.t. Interior, Editor. (2014), U.S. Geological Survey.
 57. Oka, D., et al., *Intrinsic high electrical conductivity of stoichiometric SrNbO₃ epitaxial thin films*. Physical Review B, (2015). **92**(20): p. 205102.
 58. Jellison Jr, G.E., et al., *Optical functions of KTaO₃ as determined by spectroscopic ellipsometry and comparison with band structure calculations*. Physical Review B, (2006). **74**(15): p. 155130.
 59. Sun, C. and D.J. Searles, *Electronics, Vacancies, Optical Properties, and Band Engineering of Red Photocatalyst SrNbO₃: A Computational Investigation*. The Journal of Physical Chemistry C, (2014). **118**(21): p. 11267-11270.
 60. Van der Pauw, L., *A method of measuring specific resistivity and Hall effect of discs of arbitrary shape*. Philips research reports, (1958). **13**: p. 1-9.
 61. Minami, T., *Substitution of transparent conducting oxide thin films for indium tin oxide transparent electrode applications*. Thin solid films, (2008). **516**(7): p. 1314-1321.
 62. Polyanskiy, M. *Refractive Index Database (RefractiveIndex.INFO)*. [cited 2018 March 1st].
 63. *Refractive Index of ITO, Indium Tin Oxide*. [cited 2018 February 15th].
 64. Song, K., M. Mohseni, and F. Taghipour, *Application of ultraviolet light-emitting diodes (UV-LEDs) for water disinfection: A review*. Water research, (2016). **94**: p. 341-349.
 65. Chatterley, C. and K. Linden, *Demonstration and evaluation of germicidal UV-LEDs for point-of-use water disinfection*. Journal of water and health, (2010). **8**(3): p. 479-486.
 66. Randive, R. *Improved POU Disinfection with UVC LEDs*. 2016. DOI: <https://www.watertechonline.com/improved-pou-disinfection-with-uvc-leds/>.

67. Kowalski, W., *Ultraviolet germicidal irradiation handbook: UVGI for air and surface disinfection*. (2010): Springer Science & Business Media.
68. Huber, T., R.A. Reddick, and G. Kubica, *Germicidal effect of ultraviolet irradiation on paper contaminated with mycobacteria*. *Applied microbiology*, (1970). **19**(2): p. 383-384.
69. Kneissl, M. and J. Rass, *III-Nitride Ultraviolet Emitters*, in *Springer Series in Materials Science*. 2016, Springer. p. 1-25.
70. Pan, L., et al., *Evolution of the Fermi surface topology in doped 122 iron pnictides*. *Physical Review B*, (2013). **88**(21): p. 214510.
71. Hu, W., et al., *Origin of the Spin Density Wave Instability in AFe_2As_2 ($A = Ba, Sr$) as Revealed by Optical Spectroscopy*. *Physical review letters*, (2008). **101**(25): p. 257005.
72. Tompkins, H.G. and E.A. Irene, *Handbook of ellipsometry*. (2005), William Andrew Pub. ;Springer: Norwich, NY Heidelberg, Germany. p. xvi, 870 p.

Appendices

Appendix A Sample Calibration

One should do calibration before acquiring any ellipsometry data. The calibration can be done by using silica (SiO_2) thin film on silicon wafer, provided by J.A.Woollam company. The CompleteEase software controls the ellipsometry measurement. Here, specifically, the method of using M-2000 model, which is commercially available by J.A.Woollam, will be discussed. The very first step is turning on the ellipsometry machine and light source and running the CompleteEase software. Once the CompleteEase software is turned on, one can find 5 tabs menus in the upper right corner of the window. One should then click the fourth tab, named “Hardware”, and click “System Check”. When the software says “mount the calibration sample”, one should put the calibration wafer on the ellipsometry stage and move on to perform the calibration. The system will measure the optical constants of Si wafer and automatically fit the ellipsometry data with the tabulated values. The calibration process should not take longer than 5 minutes. After the calibration, one should first check if the fitting looks good. The mean square error (MSE) for the fitting should be around 1. One should also check if the thickness and surface roughness match with the values that is already given. The values should be written in the sample box of Si wafer. Lastly, one should check that depolarization rate does not exceed $\sim 5\%$. After checking that all the values match, one can start the measurement.

Figure A.1 shows the calibration result. In the lower part of the figure, there is a graph panel that includes double y-axis plot of psi (Ψ) and delta (Δ) vs. wavelength in nm, along with model, which is represented as dotted line. If one can just eyeball the plot, the model plot matches with the data very well. One can justify “goodness of the model” by looking at the value of MSE, which is shown in the top left corner in **Figure A.1**. The MSE value in this case is 0.999, which is pretty good. For an ideal model, the MSE value is around 1. While this value of MSE can be achieved on certain types of samples, such as SiO_2 layer on Si substrate, the

best model fit for more complex sample may exhibit higher MSE values. The acceptable MSE values should be less than 10. After checking MSE value, one should compare the thickness value of the sample determined by the fitting to the value that is already given. In this case, the thickness value listed in the sample box was 280.4 Å, which matches well with the measured thickness value of 28.41 nm. Also, one should check depolarization rate by clicking “Graph Type” on the upper left corner of the plot. If the depolarization rate values oscillate within 5 %, they are good. Now, one is ready to acquire ellipsometry data of your sample.

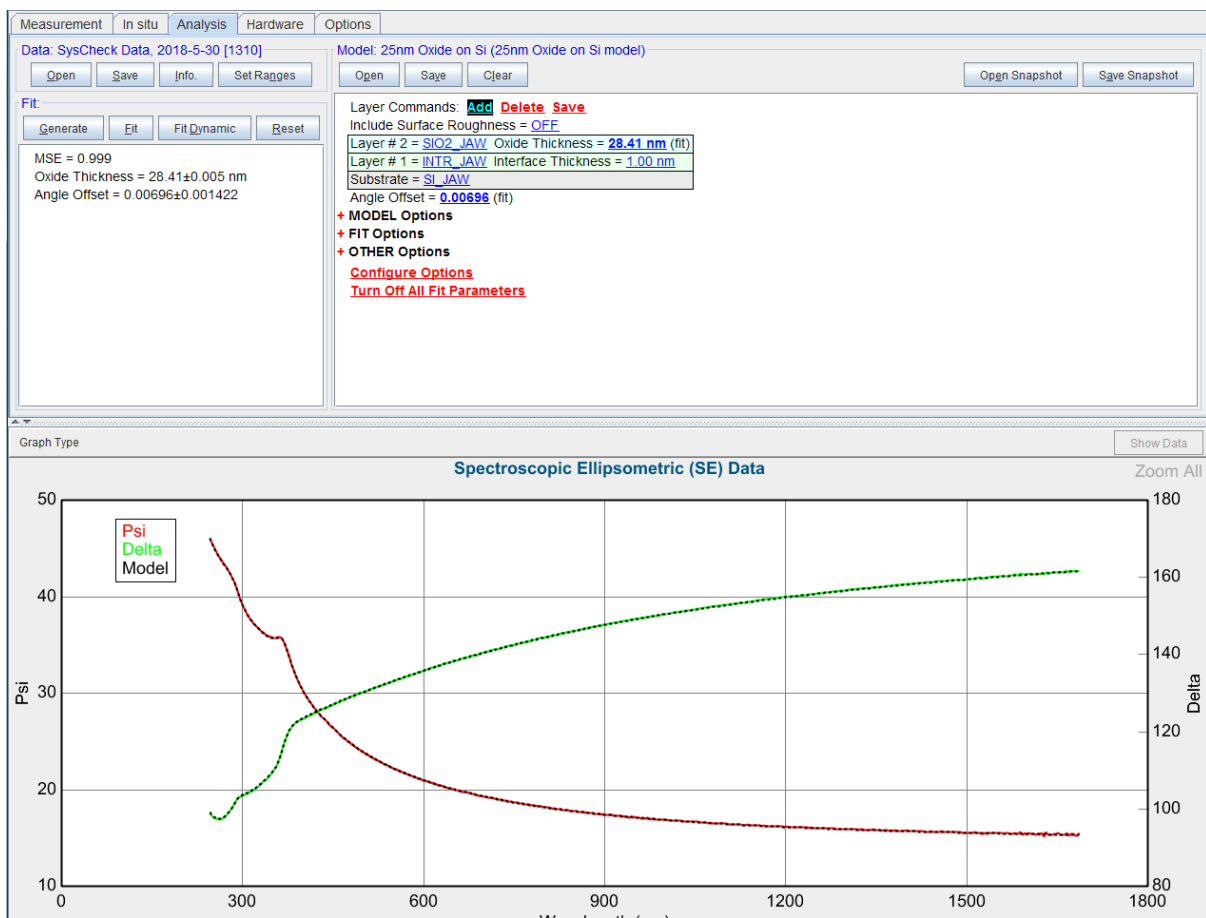


Figure A.1 CompleteEase software that shows the result of calibration. The MSE value and measured film thickness are listed in the upper left side of the figure. The plots of raw data and model are shown in the bottom part of the figure, as a function of wavelength in nm.

Appendix B Data Acquisition

After proper calibration, ellipsometry measurement can be done on one's own samples.

First, one should mount the sample on the ellipsometry stage. If the sample is optically isotropic,

the orientation of the sample in the stage will not matter. However, if your sample is optically anisotropic, it is strongly recommended to match the crystallographic direction of the sample with the ellipsometry stage. The measurement method and fitting of ellipsometry data for anisotropic sample will be further discussed later. After the sample is mounted properly on the stage, one clicks the “measurement” tab on the very upper left corner. If one chooses “prompt for acquisition parameters” under “recipe”, and click “measure”, one will see a small window popping up in the middle of the screen, named “Acquisition Parameters Setup”, as shown in **Figure B.1**.

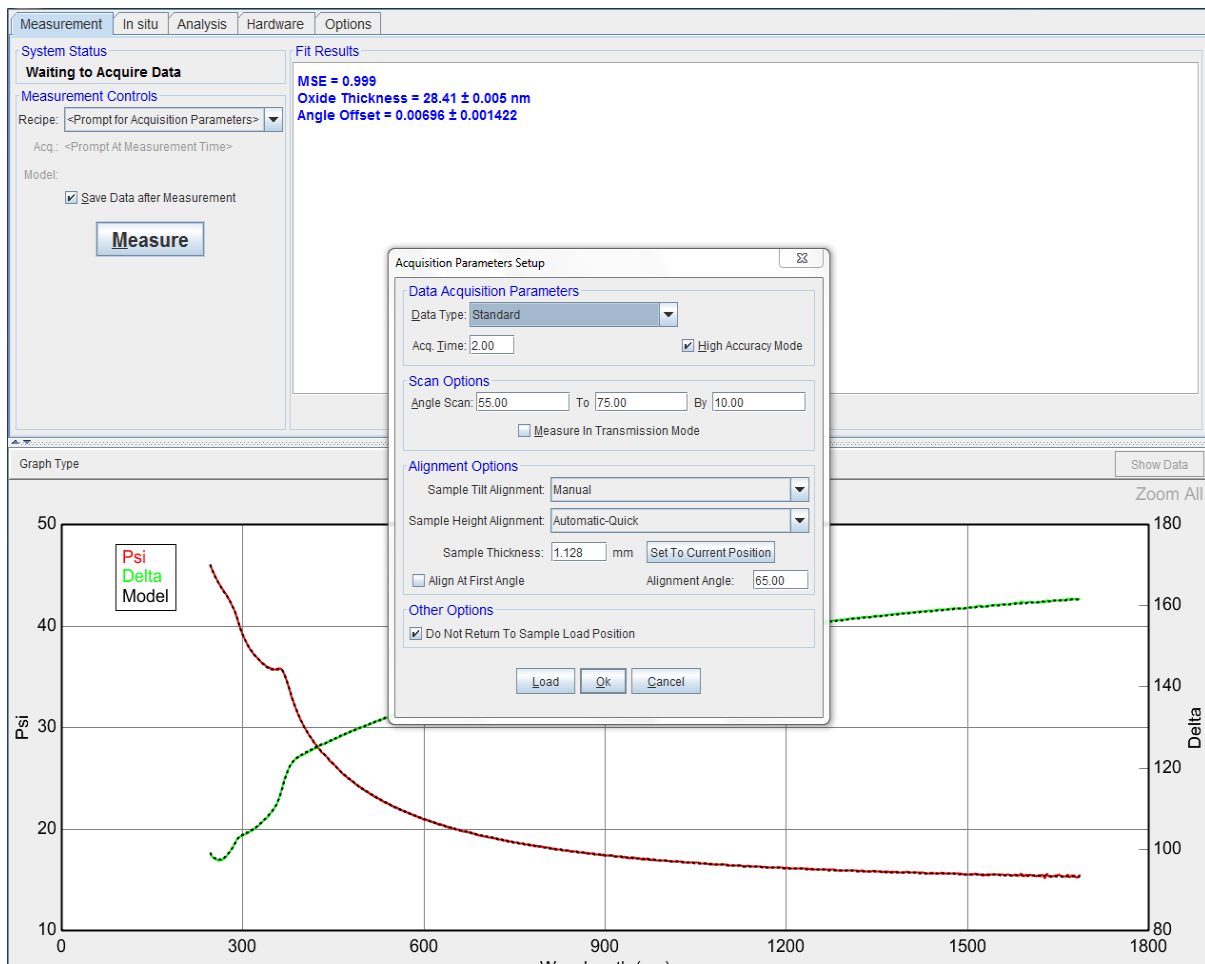


Figure B.1 Data acquisition procedure for CompleteEase software. The window in the middle is “Acquisition Parameters Setup”, which can control the measurement method.

In the “Acquisition Parameters Setup” window, there are three types of options for the measurement: “Data Acquisition Parameters”, “Scan Options” and Alignment Options”. For

“Other options” one just leaves it as it is. In the window under “Data Acquisition Parameters”, one clicks “Standard” for the measurement of isotropic sample. For the measurement of anisotropic sample, one should choose either “Generalized Ellipsometry” or “Mueller Matrix” options. With scan options, one can choose the range and step of incident angle of the beam. For precise ellipsometry measurement, it is important to perform the measurement with variable incident angle. Three different incident angles are good enough. For “Alignment Options”, one chooses “Manual” for “Sample Tilt Alignment” and “Automatic-Quick” for “Sample Height Alignment”. After properly choosing the options, one clicks “Okay” to go forward.

After clicking “Okay”, one will have the screens as shown in **Figure B.2 (a)** and will be asked to manually align the reflected beam to the detector. As shown in **Figure B.2 (a)**, the red cross is initially located far from the center of the black cross. One should adjust the knobs in the stage and get the red cross overlap with the black cross, as shown in **Figure B.2 (b)**. Once this step is done one presses “Enter” to go forward. One might be asked to do this process several times. Once this process is done, the ellipsometer starts the measurement. Each measurement usually takes 1-5 mins.

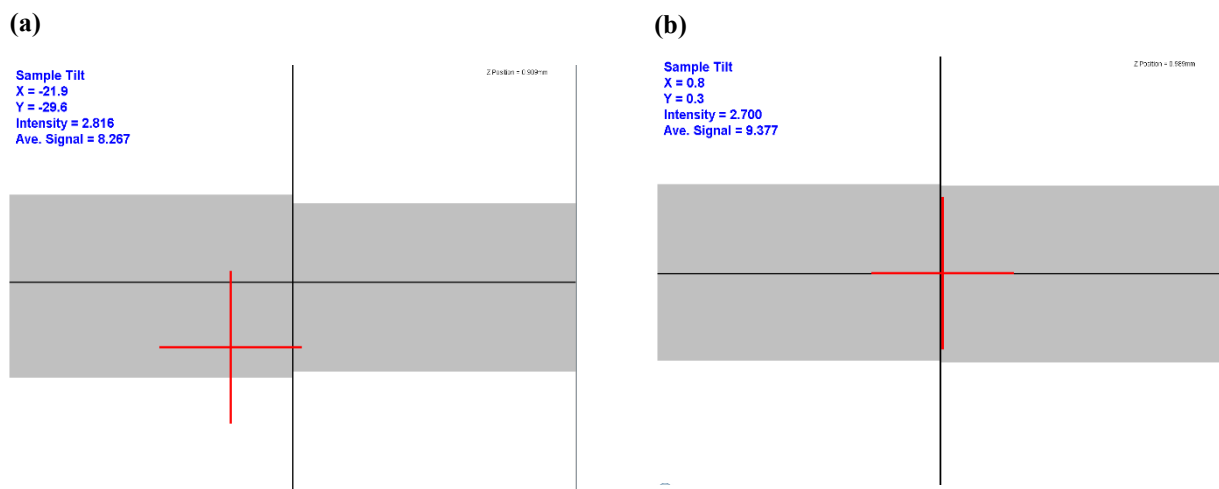


Figure B.2 Beam alignment window that shows **(a)** before the alignment and **(b)** after the alignment. For properly aligned reflected beam, the red cross should coincide with the black cross.

Once the measurement is done, one should see the screen, as shown in **Figure B.3**.

Figure B.3. shows the measurement result for 10 nm thick SiO₂ on Si substrate. The optical constants of SiO₂ can be easily fitted because there are already tabulated values for the fitting. However, in general, when one measures the material without known values of optical constant, one should model it by oneself. As shown in graph panel of **Figure B.3**, there are three plots for psi (Ψ) and 3 plots for delta (Δ). This is because three incident angles were chosen prior to the measurement. The incident angles of 55°, 65° and 75° are noted in the legend of the plot.

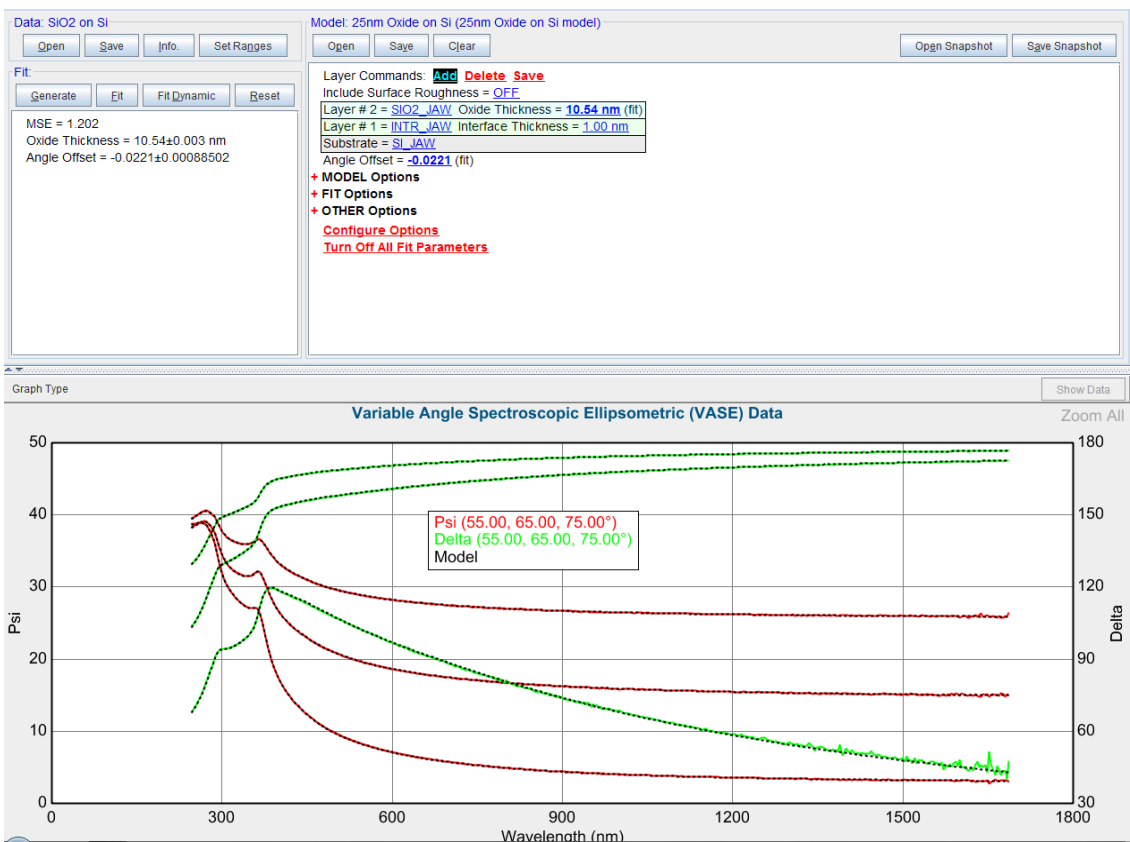


Figure B.3 CompleteEase software after ellipsometry measurement is done. The plot shows three sets of psi (Ψ) and delta (Δ) vs. wavelength in nm with incident angle of 55°, 65° and 75°.

After one is done with the measurements, one should check if the depolarization is less than ~5 %. After checking the depolarization, one can save the data file in SE. file format, which is only compatible with CompleteEase software. Now, one is ready to do the analysis. The ellipsometry measurement process itself is very simple and only takes at most 15 minutes per one measurement. What really important is data analysis, since raw data itself is not

meaningful at all. One should properly analyze ellipsometry raw data to extract optical constants of the sample.

Appendix C Single Crystal

Analyzing ellipsometry data of single crystal is simpler than analyzing that of multilayer sample. One has to only deal with 3 media: air, surface roughness, and the material of interest. In order to start analysis, one should first open the SE. data file with CompleteEase software and open “blank.mod” in the analysis tab. After opening “blank.mod”, one should see “Substrate = none” inside a gray rectangle in the analysis tab, which is on the right side of the CompleteEase window. One then clicks “none” and chooses “B-spline”, then clicks “fit”. The “B-spline” fit will automatically fit the entire function with MSE of around 1~2. One should then be able to find “B-spline” inside the gray rectangle. One right clicks it and click “Parameterize Layer”. One then should see a window named “Parameterize Layer” pops up in the middle of the screen, as shown in **Figure C.1**.

Now, one can start the analysis. Before starting the analysis, one should know what kind of material is one dealing with. For example, if one is dealing with metallic material, one should use Drude-Lorentz model mentioned in **Chapter 1.3.5**. One clicks “Add oscillators” to add Lorentz or Drude function. For one’s convenience, one can start fitting the imaginary part of dielectric constant first and move on to real part of the dielectric constant. For metallic media, add one Drude model and several Lorentz or Tauc-Lorentz models. The number of Lorentz or Tauc-Lorentz model should match with the number of absorption peaks in the imaginary part of dielectric constant. For asymmetric peak, one should use Tauc-Lorentz for better fit; however, if the peak is symmetric, one should use Lorentz in order to minimize the fitting parameter. For each Lorentz model, there are 3 parameters, denoted as “En”, “Br” and “Amp”. “En” is the resonant frequency, “Br” is the broadness of the peak, which is equivalent to Γ in **Equation (1.29)**. and “Amp” is the amplitude of the peak. One should see the spectra of imaginary part

first and determine where the peak is located. Then one should adjust “En” for the location of each Lorentz peak and adjust “Br” and “Amp” for the broadness and amplitude of the peak. For each Tauc-Lorentz model, there is one more fitting parameter, denoted as “Eg”. This represents Tauc-gap, which was already discussed in **Chapter 1.3.3**.

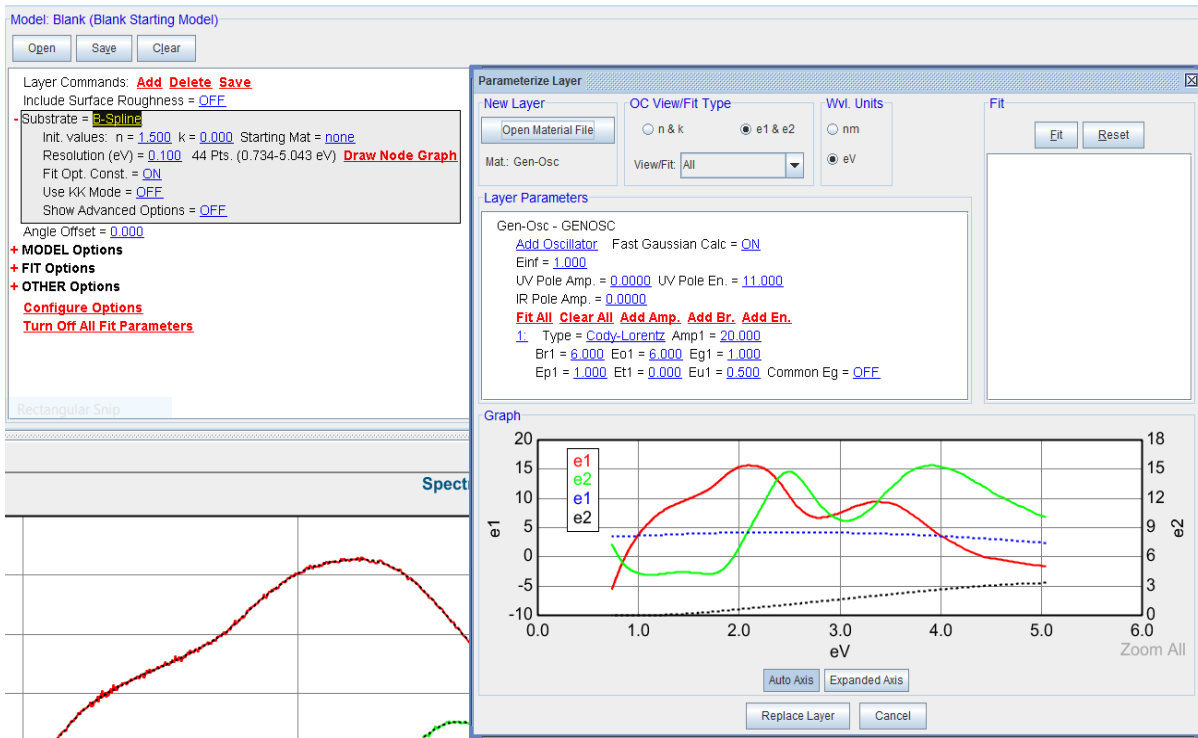


Figure C.1 Parameterize Layer window in CompleteEase software. The gray box mentioned in the text is on the upper left corner of the figure.

Once one is done with the modeling of imaginary part, one can start fitting the real part. The real part can be fitted by using pole equations, which is described by Sellmeier model. One should find that modeling real part is much simpler than modeling imaginary part. Once one is done with modeling the real part, one can finalize the fitting and click “Replace Layer”. Once the layer is replaced, one clicks “Fit” on the upper left corner and sees if the fitting is good. One can justify the fitting by looking at the MSE value. MSE value should not exceed 10. If MSE value does not look good, one should repeat the procedure till the fitting is good (MSE less than 10). In general, one should get MSE values of around 2~4 for the best fitting results.

Once the modeling is done, one can get extract n and k of the sample by right clicking the model and clicking “Graph Layer Optical Constant”. One will be able to see the spectra of optical constants in the graph panel. One should right click the graph and click “Copy Data to Clipboard”. Now one can just paste the fitting result to either excel or notepad.

Appendix D Thin Film

Analyzing ellipsometry data for thin film samples is more complex than analyzing single crystal samples. For thin film samples, Ψ and Δ resulted from two reflected rays, one from the interface between air and the surface, and the other from film/substrate interface. Therefore, one has to exclude contribution from film/substrate interface. In order to do so, one has to analyze the ellipsometry data for the substrate first. Most of the ellipsometry data of substrate can be modeled with simple Sellmeier model or Cauchy model. Therefore, one can simply obtain the optical constants of the substrate. Once the optical constants of the substrate are obtained, one should click “add layer”. By doing so, one can add a layer of B-spline. After this process, right click the B-spline layer and click “Parameterize Layer”. By doing so, one can exclude the contribution of Ψ and Δ from film/substrate interface. Rest of the explanation for fitting method is equivalent to that for method to fit ellipsometry data for single crystal samples that was discussed in the **chapter 1.5.1**. However, one needs to know the thickness of the sample before performing ellipsometry analysis on the thin film samples. Thickness measurement can be done by using X-ray techniques.

Appendix E Surface Roughness Characterization

Surface roughness characterization can be done by adding another layer between the sample and the substrate, as shown in **Figure E.1**. In analysis panel, one clicks “Add” and opens “EMA.mat” file. Once one adds the EMA layer between the film and the substrate, one can decide the thickness of the surface roughness. In order to figure out the thickness of the surface roughness, one can utilize Atomic Force microscopy (AFM) or surface profilometer. The characterization of the roughness with these techniques can give you an idea of the thickness of the surface roughness. One can then define the materials that consists of the surface roughness. For surface roughness, one of the material should be air, and the other should be the material. One can also choose volume ratio of each component by clicking the number listed next to “EMA %”. When deciding the volume ratio of each component in the surface roughness, one should consider morphology of the surface. This can also be characterized by AFM or surface profilometer. Lastly, one can choose analysis method for characterizing surface roughness by clicking blue text listed next to “Analysis Mode”. There are several choices, but Bruggeman is the most appropriate method, as already discussed in **Chapter 1.3.7**.

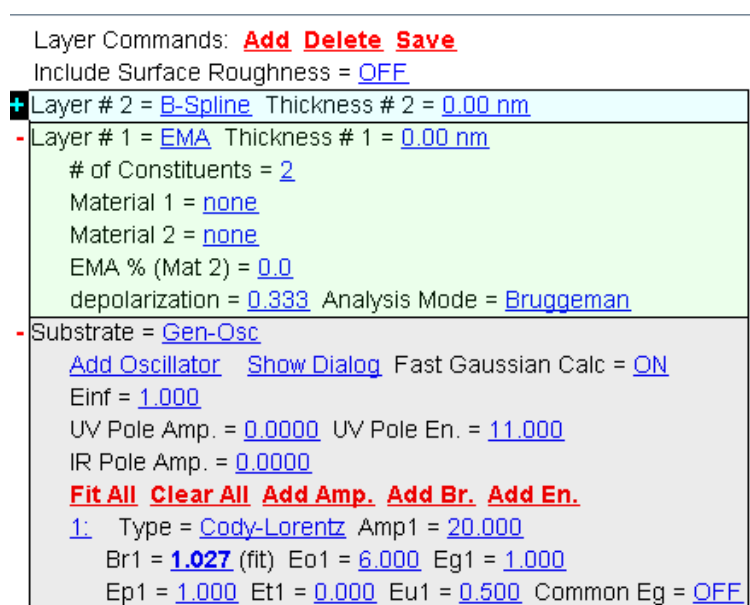


Figure E.1 Analysis panel of CompleteEase containing EMA layer (green box). The layer has several options for surface roughness characterization.

For simplicity, one can also turn on “Include Surface Roughness” in the upper left corner of analysis panel. This method uses Bruggeman EMA with 50 % of volume ratio for each constituent. For this option, one only needs to obtain the thickness of surface roughness.

In chapter 1, the topics regarding spectroscopic ellipsometry have been discussed, from the basic idea of spectroscopic ellipsometry and necessary optics concepts to analysis method using CompleteEase software. In chapter 2, the topics regarding SrNbO₃, which is transparent conducting correlated metal, will be discussed in detail. For more information regarding ellipsometry, one should read “*Spectroscopic Ellipsometry: Principles and Applications*”, written by Fujiwara Hiroyuki¹ and the manual for CompleteEase software⁴, which is available online as pdf files. One could also read “*Handbook of Ellipsometry*”, written by Harland Tompkins and Eugene Irene⁷².